THE UNIVERSITY *of* EDINBURGH

This thesis has been submitted in fulfilment of the requirements for a postgraduate degree (e.g. PhD, MPhil, DClinPsychol) at the University of Edinburgh. Please note the following terms and conditions of use:

This work is protected by copyright and other intellectual property rights, which are retained by the thesis author, unless otherwise stated.
A copy can be downloaded for personal non-commercial research or study, without prior permission or charge.
This thesis cannot be reproduced or quoted extensively from without first obtaining permission in writing from the author.
The content must not be changed in any way or sold commercially in any format or medium without the formal permission of the author.
When referring to this work, full bibliographic details including the author, title, awarding institution and date of the thesis must be given.

INPUT-OUTPUT TRANSFORMATIONS IN THE AWAKE MOUSE BRAIN USING WHOLE-CELL RECORDINGS AND PROBABILISTIC ANALYSIS

PAOLO PUGGIONI

Doctor of Philosophy
School of Informatics
University of Edinburgh

2015

Paolo Puggioni:
Input-output transformations in the awake mouse brain using whole-cell recordings and probabilistic analysis
Doctor of Philosophy, 2015

SUPERVISORS:
Dr. Mark van Rossum
Dr. Ian Duguid

EXAMINERS:
Prof. Matthew Nolan (Centre for Integrative Physiology, University of Edinburgh)
Prof. Peter Latham (Gatsby Unit, University College London)

...in ogni epoca qualcuno, guardando Fedora qual era,
aveva immaginato di farne la cittá ideale,
ma mentre costruiva il suo modello in miniatura,
giá Fedora non era piú la stessa di prima,
e quello che fino a ieri era stato un suo possibile futuro,
ormai era solo un giocattolo in una sfera di vetro...
Italo Calvino, Cittá invisibili (Le cittá e il desiderio, 4)

...in every age someone, looking at Fedora as it was,
imagined a way of making it the ideal city,
but while he constructed his miniature model,
Fedora was already no longer the same as before,
and what had been until yesterday a possible future
became only a toy in a glass globe...
Italo Calvino, Invisible Cities, (Cities and Desire, 4)

ABSTRACT

The activity of cortical neurons in awake brains changes dynamically as a function of the behavioural and attentional state. The primary motor cortex (M1) plays a central role in regulating complex motor behaviors. Despite a growing knowledge on its connectivity and spiking pattern, little is known about intra-cellular mechanism and rhythms underlying motor-command generation. In the last decade, whole-cell recordings in awake animals has become a powerful tool for characterising both sub- and suprathreshold activity during behaviour. Seminal *in vivo* studies have shown that changes in input structure and sub-threshold regime determine spike output during behaviour (input-output transformations).

In this thesis I make use of computational and experimental techniques to better understand (i) how the brain regulates the sub-threshold activity of the neurons during movement and (ii) how this reflects in their input-output transformation properties.

In the first part of this work I present a novel probabilistic technique to infer input statistics from *in-vivo* voltage-clamp traces. This approach, based on Bayesian belief networks, outperforms current methods and allows an estimation of synaptic input (i) kinetic properties, (ii) frequency, and (iii) weight distribution. I first validate the model on simulated data, thus I apply it to voltage-clamp recordings of cerebellar interneurons in awake mice. I found that synaptic weight distributions have long tails, which on average do not change during movement. Interestingly, the increase in synaptic current observed during movement is a consequence of the increase in input frequency only. In the second part, I study how the brain regulates the activity of pyramidal neurons in the M1 of awake mice during movement. I performed whole-cell recordings of pyramidal neurons in layer 5B (L5B), which represent one of the main descending output channels from motor cortex. I found that slow large-amplitude membrane potential fluctuations, typical of quiet periods, were suppressed in all L5B pyramidal neurons during movement, which by itself reduced membrane potential (V_m) variability, input sensitivity and output firing rates. However, a subpopulation of L5B neurons (50%) concurrently experienced an increase in excitatory drive that depolarized mean V_m, enhanced input sensitivity and elevated firing rates. Thus, movement-related bidirectional modulation in L5B neurons is mediated by two opposing mechanisms: 1) a global reduction in network driven V_m variability and 2) a coincident, targeted increase in excitatory drive to a subpopulation of L5B neurons.

ACKNOWLEDGEMENTS

Thanks to Mark van Rossum and Ian Duguid for being terrific supervisors.
Whenever I have needed guidance, Mark has understood my problems in a snap and given great advice. Mark has a clarity of thought that I will always try to emulate.
Like Charon in the Greek mythology, Ian carried me to the intricate world of experimental neuroscience. He has been an enthusiastic guide, spending with me innumerable evenings shoulder to shoulder in the laboratory. He taught me all his tricks to train me as an *in vivo* electrophysiologist. He has always given me the best support by coordinating the activity of his Lab members to contribute to my project. From Ian I learnt that the best results are obtained when researchers work towards a common goal as a team, helping each other. I believe this is a rare quality in experimental labs.

Throughout my PhD, I have received inputs and help from many students and researchers of the Doctoral Training Centre in Neuroninformatics (DTC), Artificial Neural Computation (ANC) and Centre for Integrative Physiology (CIP) of the University of Edinburgh. In particular:

- in *chapter 3*: Marta Jelitai (for collecting the data), Luigi Acerbi and Chris Williams (for insightful discussions and comments);
- in *chapter 4*: Julia Schiemann (for her exceptional help in the experiments), Miha Pelko (for his collaboration on the model), Joshua Dacre, Myles Cowper-Coles and Marta Jelitai (for their help in the experiments),
- in *chapter 5*: Dylan Ross (for being an exceptional student and delivering extraordinary results in the framework of his BSc thesis).

I thank my DTC-09 fellows, in particular Luigi, Lukas, Rui, Vincent and Daga. We have been an excellent crew. These five years together have been a second high school for me.

I really enojoyed having Matt Nolan and Peter Latham as thesis examiners. Their merciless, but fair, comments significantly improved this work.

Finally, thanks to Ugo Amaldi, Ettore Rosso and Giulio Magrin. A long time ago, they helped me in my first steps to scientific research.

DECLARATION

I declare that this thesis was composed by myself, that the work contained herein is my own except where explicitly stated otherwise in the text, and that this work has not been submitted for any other degree or professional qualification except as specified.

Edinburgh, 2015

Paolo Puggioni, July 14, 2015

CONTENTS

1 INTRODUCTION 1

1.1 A primer on the experiments . . . 2
1.1.1 An overview of the cortex . . . 2
1.1.2 Primary motor cortex . . . 3
1.1.3 Whole-cell recordings from awake animals . . . 6
1.1.4 Cortical state and its effects on the membrane potential . . . 7
1.1.5 How do neurons integrate synaptic inputs? . . . 10
1.2 A primer on the inference techniques . . . 12
1.2.1 Bayes theorem . . . 12
1.2.2 Graphical models . . . 13
1.2.3 Sampling the posterior probability . . . 14
1.2.4 Model comparison . . . 15
1.2.5 Useful libraries . . . 16
1.3 Thesis layout . . . 16

2 STATISTICAL PROPERTIES OF THE MEMBRANE POTENTIAL 17

2.1 Single compartment model of a neuron . . . 17
2.1.1 Conductance based synapses . . . 18
2.1.2 Effective input resistance . . . 19
2.2 First order statistics . . . 20
2.3 Power spectrum and second order statistics . . . 21
2.3.1 Power spectrum of the conductances . . . 21
2.3.2 Power spectrum of the membrane potential . . . 22
2.3.3 Validation of the model . . . 23
2.4 Conclusion . . . 24

3 PROBABILISTIC INFERENCE OF *in vivo* SYNAPTIC INPUT STATISTICS FROM VOLTAGE-CLAMP DATA 26

3.1 Introduction . . . 26
3.1.1 Voltage-clamp recordings . . . 26
3.1.2 Which mechanisms underlie the increase in excitatory current in cerebellar interneurons during movement? . . . 28
3.1.3 Measuring synaptic input statistics *in vivo* . . . 30
3.1.4 Comparing *in vivo* to *in vitro* synaptic input frequency and response size distribution . . . 32

3.1.5 Other probabilistic methods used to estimate synaptic inputs *in vivo* . . . 33
3.2 Generative model . . . 35
3.2.1 Mathematical description of the synaptic current . . . 35
3.2.2 Moments of the synaptic current . . . 36
3.2.3 Power spectrum of the synaptic current . . . 38
3.3 Inference . . . 39
3.3.1 Ideal model . . . 39
3.3.2 Description of the nodes . . . 40
3.3.3 Modelling *in vivo* variability and experimental conditions . . . 42
3.3.4 Description of the sampling algorithm . . . 44
3.4 Results - model validation . . . 48
3.4.1 Inferring the parameters with the correct synaptic weight distribution . . . 48
3.4.2 Impact of the recording length on the inference . . . 49
3.4.3 Model selection . . . 49
3.4.4 Adding sources of *in vivo* variability . . . 52
3.5 Results - inference of *in vivo* data . . . 53
3.5.1 Higher frequency of synaptic inputs increases excitatory current 53
3.6 Conclusion . . . 56
3.6.1 Summary of the findings . . . 56
3.6.2 Assumptions of the model and future work . . . 57
4 SUBTHRESHOLD DYNAMICS UNDERLYING BEHAVIORAL STATE-DEPENDENT BIDIRECTIONAL MODULATION OF MOTOR CORTEX OUTPUT 59
4.1 Introduction . . . 59
4.1.1 Modulation of motor cortex activity during behaviour . . . 59
4.1.2 Cellular mechanisms that regulate input sensitivity . . . 61
4.2 Methods . . . 63
4.2.1 Animals and surgery . . . 63
4.2.2 Cortical mapping . . . 63
4.2.3 *In vivo* electrophysiology . . . 64
4.2.4 Motion index and motor pattern discrimination . . . 65
4.2.5 Functional classification of recorded neurons . . . 65
4.2.6 Current injection and spiking probability . . . 66
4.2.7 Intrinsic properties and morphological reconstructions . . . 66
4.2.8 Identification of projection targets . . . 67
4.2.9 Membrane potential dynamics . . . 68
4.2.10 Effective input resistance and membrane time constant . . . 70

4.2.11 Modulation of V_m power in the δ-band during quiet wakefulness 71
4.2.12 Detection of compound synaptic events . . . 71
4.2.13 Statistics . . . 72
4.3 Results . . . 73
4.3.1 Membrane potential dynamics of L5B pyramidal neurons during self-paced, voluntary movement . . . 73
4.3.2 Bidirectional input sensitivity modulation during voluntary movement . . . 77
4.3.3 Behavioral state-dependent changes in network-driven Vm variance . . . 79
4.3.4 Increased excitatory input in $L5B_{enh}$ neurons during movement . 83
4.3.5 Frequency of compound large synaptic inputs increases in $L5B_{enh}$ neurons during movement . . . 87
4.4 Discussion . . . 90
4.4.1 Functional classification of individual neurons . . . 90
4.4.2 Excitatory-inhibitory conductances in L5B pyramidal neurons . . 92
4.4.3 Estimation of synaptic inputs statistics *in vivo* . . . 93
4.4.4 Slow V_m fluctuations in M1 projection neurons . . . 96
4.4.5 Possible sources of increased excitatory inputs to $L5B_{enh}$ neurons during movement . . . 96
4.4.6 Could network activity underlie the movement-related bidirectional changes we measured? . . . 99
4.4.7 What did we learn? . . . 100
5 CONCLUSION 103
5.1 Bidirectional changes in M1: driving or driven by movement? . . . 104
5.2 Origin of the slow fluctuations . . . 105
5.3 Conclusion . . . 109
BIBLIOGRAPHY 110

1

INTRODUCTION

The brain, an orchestra without a conductor. This was the title of the inspiring talk by Prof. Wolf Singer that I attended at CERN (European Center for Nuclear Physics, Geneva) in 2008 (Singer, 2008), which encouraged me to leave Physics and embark on my PhD in Computational Neuroscience. The brain is a self-organised, highly distributed system made of about 100 billion neurons (Azevedo et al., 2009) connected by about 140 trillion synapses (Alonso-Nanclares et al., 2008). Each neuron is a powerful computational unit. In a very simplified picture, a neuron receives thousands of inputs per second, integrates them and, if a threshold is reached, fires a *spike*.

Spikes transmit new inputs to downstream targets (Koch, 1999). Intuitively, the probability that an excitatory input signal generates an output depends on two quantities: firstly on the size of the signal, secondly on the state of the neuron when the input was received (distance to threshold).

This straightforward observation leads to a much deeper concept. The same input can produce two different outcomes depending on the state of the receiving neuron (Arieli et al., 1996). Recent studies are bringing overwhelming evidence that the brain differentially tunes the state of its neurons in particular behavioural circumstances (McCormick et al., 1993; Wilson and Kawaguchi, 1996; Castro-Alamancos, 2002a; Poulet and Petersen, 2008; Lakatos et al., 2009; Harris and Thiele, 2011; Poulet et al., 2012; Saleem et al., 2013; Bennett et al., 2013; Polack et al., 2013; Tan et al., 2014). Computational neuroscientists enjoy borrowing terminology from Physics and Engineering. They say that the brain changes the *gain*, or the *sensitivity* of its computational units (Carandini et al., 1997; Chance et al., 2002; Ayaz and Chance, 2009; Silver, 2010), where each unit performs an operation to transform the inputs into an output. I will discuss in depth the meaning of gain and sensitivity later (1.1.5): for the moment one can consider them as a measure of how much inputs are amplified.

We now face a fundamental question: what are the mechanisms that neurons exploit in order to regulate their input-output transformations? It is an open and controversial issue. This dissertation investigates input-output transformations in the primary motor cortex (M1) of the mouse, an area of the brain that plays a central role in regulating complex motor behaviors (Graziano et al., 2002; Lemon, 2010). I have used a combination of computational and experimental techniques to study how move-

ment influences the way information is propagated by neurons in M1. This thesis is far from giving a complete answer to the fundamental question presented above, however I will present two main contributions:

- I developed an inference method to estimate the statistics of the inputs to a neuron from *in vivo* intracellular recordings, and
- I performed intracellular recordings in M1 of awake mice, finding two subpopulations of neurons that differently regulate their input-output transformations and firing rates with movement.

In the next sections, I will introduce the elements needed to understand the experiments and the computational work of this thesis.

1.1 A PRIMER ON THE EXPERIMENTS

1.1.1 *An overview of the cortex*

The cerebral cortex is the first structure that is found under the skull of mammals. It consists of folded layers of densely connected neurons and is thought to be responsible for the high level functions typical of the mammal brain (Kandel et al., 2000). Here I present a short overview of the structure, function and connectivity from small to large scale. The focus is on the motor cortex of mice.

In a very simplified view, a neuron consists of three parts: (i) the soma, which contains the nucleus of the cell, (ii) the dendritic tree, which receives inputs from other neurons through synapses, (iii) the axon, which carries the output and projects to the dendrites of other neurons. Neurons mainly use spikes to communicate. Spikes are mostly generated in the axon hillock, the portion of the axon close to the soma, and travel along the axon to make synaptic contact with downstream neurons - for a more complete introduction with a computational focus, see Koch (2004).

In the cortex, neurons can be broadly divided into two categories: (i) pyramidal neurons, which are excitatory, and (ii) interneurons, which are inhibitory. Neurons are densely connected in their local region. The probability that two near-by neurons are connected is between 0.1 and 0.3 and depends on neuron types and brain areas (Lefort et al., 2009; Kiritani et al., 2012; Perin et al., 2013).

Neurons appear to be divided into layers. This peculiar layered structure can be observed with a microscope in cortical brain slices (Fig. 1.1 **a**). In the cortex there are 6 layers, which have distinct anatomical features in different cortical regions, and are

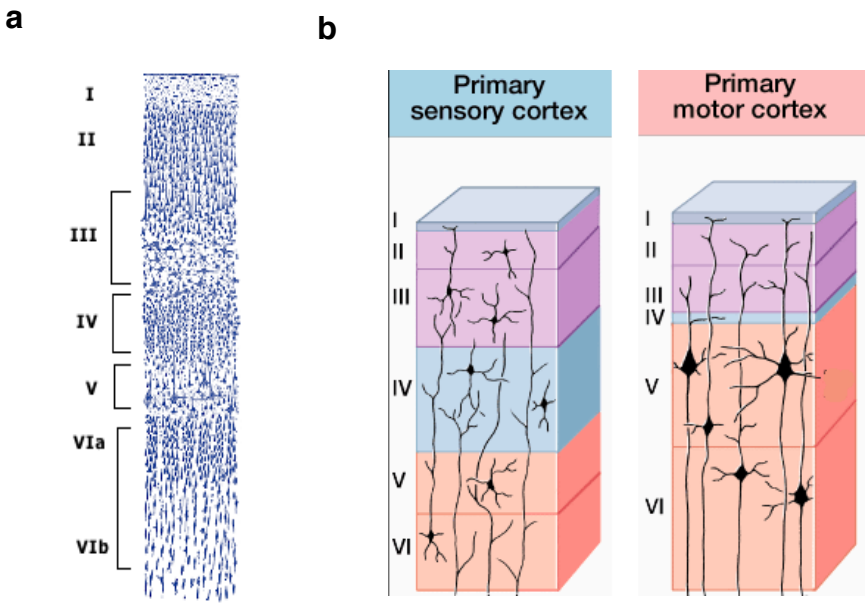

Figure 1.1: Cortical layers. **a)** Vertical section of the visual cortex of man, stained with Nissl method, indicating the division in cortical layers - *figure adapted from* Cajal (1899). **b)** Schematic view of primary sensory cortex and primary motor cortex - *figure adapted from* Joseph (1996).

thought to perform specific functions (Kandel et al., 2000) (Fig. 1.1 **b**). Interestingly, layer 2 (L2) and layer 4 (L4) have a granular, densely packed structure (rich in stellate cells), which contrasts with the agranular nature of the others (mainly containing pyramidal cells).

Anatomically, we also observe connections between layers, where neurons are organised into cortical columns. The canonical but over-simplified view is that L4 is the main input layer, receiving inputs from the thalamus and other sub-cortical regions. From here, the signal is transmitted to the superficial layers (L2/3), then to the deep layers (L5 and L6) which are considered the output of the cortex and project to other brain areas (Douglas and Martin, 2004). This view has been recently challenged in the sensory cortex, where it was shown that sensory processing in deep layers is a consequence of the recruitment of a direct thalamcortical pathway to L5 (Constantinople and Bruno, 2013).

1.1.2 *Primary motor cortex*

The primary motor cortex (M1) is thought to play a central role in regulating complex motor behaviors (Graziano et al., 2002; Lemon, 2010). Although the following

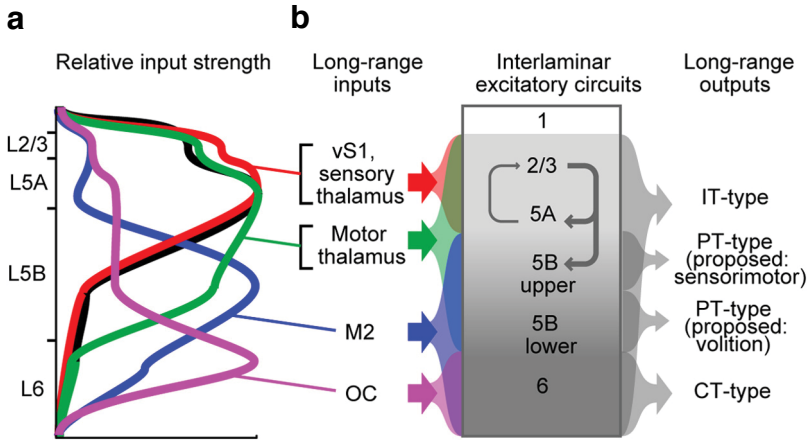

Figure 1.2: Circuit diagram for lamina-specific long-range excitatory inputs to primary motor cortex. **a)** Schematic showing the relative laminar-specific input pathway strength in M1. Profile of S1 input (black) is included for comparison. **b)** A circuit diagram for excitatory inputs to primary motor cortex. (Left) Laminar specificity of long-range excitatory input is shown for all pathways described. Input from S1 to M1 is included with sensory thalamus. (Center) Interlaminar excitatory circuits between M1 pyramidal neurons (gray) are dominated by descending pathways. (Right) Long-range outputs of M1 are shown, with laminar specificity indicated.
Figure adapted from Hooks et al. (2013).

description is specific to the M1 of mice, the general structure still applies to other mammals and primates as well.

Connectivity within M1 layers and between M1 and other brain areas has been recently investigated with anatomical and functional studies in brain slices. It was shown that a column of M1 has a hierarchical top-down structure. It can be broadly divided into upper (L2/3 and L5A) and lower (L5B and L6) layers, with connections going from the former to the latter (Weiler et al., 2008; Anderson et al., 2010) (Fig. 1.2 **b**, center). Notably, rodent M1 does not have a predominant L4, but see Isomura et al. (2009), which on the other hand is prominent in the neighboring primary sensory cortex (S1). The lack of a granular layer is an indication that information flow in M1 differs from other sensory areas.

Upper layers (traditionally considered as *input* layers) receive the majority of their inputs from S1 (Fig. 1.2 **a**) and project to the lower layers (traditionally considered as the *output* of M1, L5B to the pyramidal tract and L6 mainly to thalamus) (Mao et al., 2011) (Fig 1.2 **b** right). The true picture is more complicated than this.

New findings (Hooks et al., 2013) challenge the traditional view of a straight hierarchical top-down pathway in M1, because it was shown that lower layers receive direct input from other brain areas. Thalamus, the main center to transfer information between sub-cortical and cortical areas (Kandel et al., 2000), sends its projections

to both upper and lower M1 in equal amount. The secondary motor cortex (M2) and the orbital cortex (OC) target mostly the lower layers (Hooks et al., 2013) (Fig. 1.2 **a**).

Interestingly, it was also shown that upper and lower layers of M1 projects to other brain structures in a very specific fashion (Fig. 1.2 **b** right). Upper layers contain neurons which have intratelencephalic projections (IT)-type, mainly targeting S1, M1 and striatum. However, lower layers contain both IT-type neurons and pyramidal tract (PT) projecting neurons. PT-type neurons are of great interest because their axons reach the brain stem and carry the information that eventually will reach the spinal cord. In this view, L5B can be considered the principal *output* of M1 because it is the only layer containing neurons that send information directly to the spinal cord.

It is a common misconception that M1 is the sole cortical area projecting to the spinal cord via the cortico-spinal tract (CST) (Lemon, 2008). Afferent axons come from a variety of cortical regions, including pre-motor areas (such as M2), supplementary motor areas (SMA) and sensory cortices (such as S1). The exact role of M1 and its interaction with other cortical areas in the generation and control of movements is still unclear. Lesion of the CST cause a breakdown in fine sensorimotor control, leading to a deterioration in motor function and in the ability to interpret the sensory feedback (Lemon and Griffiths, 2005).

Many studies in different species showed that neurons in M1 activate or inactivate before and during movement onset (Tanji and Evarts, 1976; Sasaki et al., 1981; Hyland, 1998) and that ensemble activity can predict behavioural outcomes (Laubach et al., 2000). The activation of the neurons in M1 could correspond to motor preparation, initiation, execution and termination. Recent evidence suggests that M1 maps the highly dimensional motor space into a smaller number of dimensions by exploiting muscle synergies, which are muscle co-activation patterns (Overduin et al., 2012). In practice, different areas in M1 are tuned to activate particular muscle synergies.

However, little is known about intracortical mechanism underlying motor-command generation. Some studies showed that the upper layers of M1 are involved in a sensory-motor loop (Dombeck et al., 2009; Komiyama et al., 2010; Huber et al., 2012). Another study found that excitatory neurons in M1 have firing patterns across layers which are related to particular phases of the movement (Isomura et al., 2009).

The work presented in this thesis is a step forward towards understanding of the mechanisms that regulate the information flow in the lower layers of M1.

1.1.3 *Whole-cell recordings from awake animals*

The first attempts to measure the electric activity of the brain go back to the early 19^{th} century (Brazier, 1963). Picking the right tool depends on the best trade-off between the experimental hurdles and the data we need to address the questions we want to answer. The technique of *in vivo* blind patch clamp electrophysiology is a relatively new tool to measure the electric activity *inside* a neuron in a living brain (Margrie et al., 2002).

In brief, to perform a whole-cell recording from an individual neuron, one inserts in the brain a glass pipette with a small diameter tip ($< 1\,\mu$m) containing a solution that mimics the intracellular fluid in the intact brain. While searching for a cell, a small positive pressure is applied to the pipette to avoid obstructions of the tip and brief current pulses are produced to measure the resistance between the pipette and the extracellular fluid. A sudden increase in resistance often means that the electrode is in close proximity to a cell membrane which is then sealed to the tip (cell attached configuration) by applying a light negative pressure to the electrode. The membrane is broken by applying a ramp of negative pressure and the cell intracellular fluid directly communicates with the solution in the pipette (dialysis of the cell).

This fairly complicated technique has a unique combination of features which make it an invaluable tool to shed light on physiological and computational mechanisms (Chorev et al., 2009; Long and Lee, 2012). Firstly, it allows the experimenter to simultaneously monitor both the sub-threshold (summation of synaptic inputs) and supra-threshold (output spikes) features, offering the possibility to relate inputs to outputs. Secondly, one can control the voltage of the cell by injecting current in the soma, for example to characterise the electrical properties (Lefort et al., 2009). Moreover, it is possible to introduce marker substances in the pipette solution, which will flow in the intracellular fluid and can be used after the recording to reconstruct the morphology and identify the neuronal type.

All these benefits come at a cost. Despite tremendous technical advances, whole cell recordings in awake animals are still very difficult to perform and only a few groups have published data using this technique (Long and Lee, 2012). Experiments still have limitations:

- due to the low success rate of each experiment, it is normally possible to record only one neuron per time, although some pioneers in the field managed to obtain simultaneous recordings (Poulet and Petersen, 2008; Gentet et al., 2010), see also Okun and Lampl (2008) in anaesthetised rats,

- to keep good electrode stability, normally animals are awake, but head restrained, although some heroic researchers were able to obtain recordings from freely moving rats (Lee et al., 2006, 2012),
- recordings are normally short (rarely above one hour) and the quality degrades over time (Chorev et al., 2009).

The most frequently used recording configuration in *in vivo* patch clamp recordings is called current-clamp. In the current-clamp mode, the glass pipette measures the voltage difference between the intracellular solution in the soma and the extracellular fluid. This value is called the membrane potential (V_m), which in a cortical neuron is usually around -65mV *in vitro* (Lefort et al., 2009). Synaptic inputs evoke small deflections of V_m in close proximity of the post-synaptic terminal. The inputs can be positive (excitatory post synaptic potentials, EPSPs) or negative (inhibitory post synaptic potentials, IPSPs) and are actively or passively propagated through the dendritic tree to reach the soma. The electrode records the effect of the inputs on the V_m of the soma.

A different configuration is called voltage-clamp. In this case, the electrode clamps the voltage of the soma at a defined value by injecting a current which is equal in amplitude (but opposite in sign) to the synaptic current propagated to the soma. The mathematical details and the limitations of the voltage-clamp configuration will be explained in chapter 3. For now, it is enough to know that with this technique we can separate the contribution of excitatory and inhibitory currents at the level of the soma.

In the framework of this thesis, I performed intracellular recordings of pyramidal neurons in superficial and deep layers of M1 in awake, head restrained mice.

1.1.4 *Cortical state and its effects on the membrane potential*

The state of the cortex is not fixed, but highly variable. The traditional view predicts that cortical state changes with sleep cycles (Steriade and McCarley, 2005). During deep sleep, cortical activity is *synchronised*, and shows slow oscillations in the δ frequency ($2-4$ Hz), where neurons tend to fire periodically together. On the other hand, rapid eye movement (REM) sleep and waking periods are characterised by a *desynchronised* state, in which neurons spike almost independently and δ oscillations are suppressed.

In the last decade, many have challenged this view by showing that during the awake state the cortex toggles between these two extremes, displaying a continuum

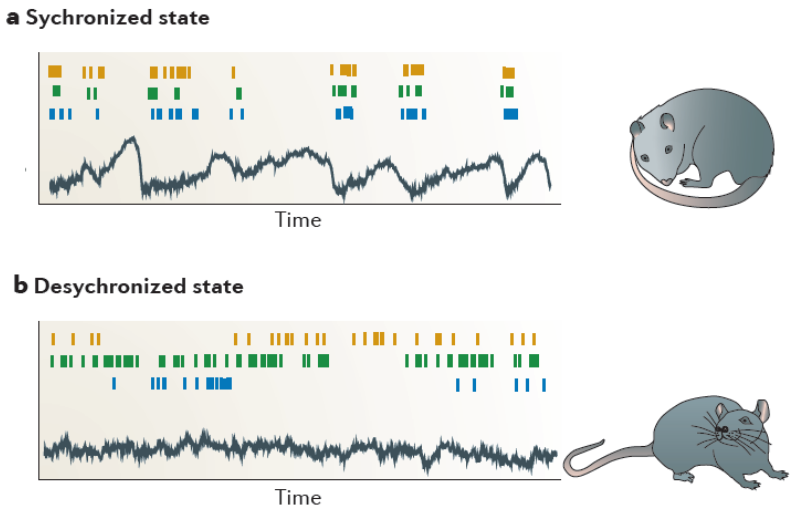

Figure 1.3: Population activity patterns vary with cortical state. Illustrations of two extremes of a continuum of states seen in awake rodents. **a)** In synchronized states, cortical populations show spontaneous common fluctuations in firing rate. During the up phase, all neuronal classes show a propensity to fire (shown by the coloured raster plots), whereas during the down phase spiking is reduced or absent. The deep-layer cortical local field potential (LFP) (shown by the black trace) shows slow negative waves accompanied by high-frequency activity in the up phase and smooth dome-shaped positive waves in the down phase. This type of activity is seen in drowsy or quiescent animals. **b)** In the desynchronized state, coordinated slow fluctuations in population activity are not seen, and low-frequency fluctuations in the LFP are suppressed. This type of activity is seen in actively behaving, alert animals. Note that this figure does not show actual recordings, but is a drawing integrating the results of multiple studies.
Figure adapted from Harris and Thiele (2011).

of states from *synchronised* to *desynchronised* (Harris and Thiele, 2011) (Fig. 1.3). Interestingly, the synchronised low-frequency fluctuation state is also present during quiet wakefulness (Buzsáki et al., 1988). Thus, the desynchronised state, once thought to characterise the whole waking period, has been associated with the execution of particular behaviours or behavioural tasks, such as: movement preparation (Churchland et al., 2006b), locomotion (Polack et al., 2013), active whisking in rodents (Crochet and Petersen, 2006; Poulet and Petersen, 2008), and attention (Fries et al., 2001; Mitchell et al., 2009; Chalk et al., 2010).

The reason why the cortex dynamically switches between synchronised and desynchronised state during wakefulness is not entirely clear.

One possibility is that slow fluctuations are a default stand-by condition of the cortex because the desynchronised state is energy-expensive (Harris and Thiele, 2011).

The desynchronisation is needed when the brain decides to reduce its internal variability to enhance signal-to-noise ratio (Arieli et al., 1996; Churchland et al., 2006b, 2010).

A different, intriguing alternative is that actually the synchronised state has a functional purpose. A series of experiments in primates has shown that cortical state can be controlled in a top-down fashion (Lakatos et al., 2008, 2009; Schroeder and Lakatos, 2009). Critically, attention can synchronise the slow oscillations with an external stimulus to improve signal-to-noise ratio of sensory perception. The idea is that the brain functions in two modes: (i) a continuous mode, when the task performed does not have a dominant periodicity and (ii) a rhythmic mode, when the cortex is entrained to an external signal. The authors argue that natural stimuli are rich in periodic patterns. However, the reason why the cortex of an awake, quiet mouse (quiet wakefulness state) displays slow rhythmical activity is still unknown. In chapter 5 I will formulate a hypothesis, based on preliminary data, to explain this feature.

Despite our poor understanding of the functional reasons, the mechanisms responsible for cortical state changes are well known (Steriade et al., 1993a). A variety of studies have identified diverse conditions that can trigger a desynchronised state. It is now clear that cortical state depends on a combination of neuromodulatory (acetylcholine and noradrenaline) and direct glutamatergic inputs (Harris and Thiele, 2011). Here I summarise the main mechanisms.

- *Thalamus* is a key player (McCormick and Bal, 1997). Thalamic excitation causes desynchronised cortical activity via glutamaergic inputs to pyramidal neurons, while thalamic inactivation increases the slow fluctuations of cortical activity during quiet wakefulness (Poulet et al., 2012). However, changes in behaviour can still trigger a desynchronised cortical state even during thalamic inactivation. In summary thalamus is sufficient but not necessary for cortical state changes.

- *Cortico-cortical interactions* are sufficient to trigger a state transition. Recently it was shown that activation of M1 induces a desyncronisation in S1 (Zagha et al., 2013).

- *Acetylcholine* (Ach) can induce thalamo-cortical desynchronisation (Steriade et al., 1991), however it is not necessary for desynchronisation in quiet wakefulness (Constantinople and Bruno, 2011), and the lack of it does not prevent desychronisation during locomotion (Polack et al., 2013).

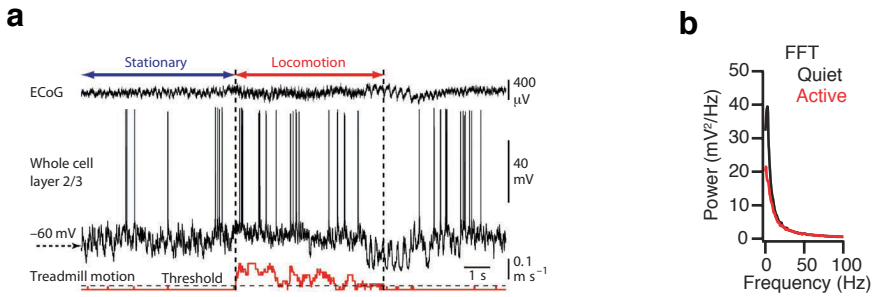

Figure 1.4: Effect of cortical state on membrane potential. **a)** Current-clamp recording of a L2/3 neuron (middle trace) simultaneously with primary visual cortex electrocorticography (ECoG, top trace) and treadmill motion (bottom trace) - *figure adapted from* Polack et al. (2013). **b)** Average power spectum of V_m from L2/3 neurons in S1 during quiet wakefulness and whisking - *figure adapted from* Poulet and Petersen (2008).

- *Noradrenaline* is necessary for the depolarisation of cortical neurons (McCormick, 1989; Constantinople and Bruno, 2011). In the absence of noradrenaline, the cortex remains in a quiescent state and responses to behavioural changes are largely suppressed (Polack et al., 2013).

Importantly, cortical state has dramatic effects on the V_m of cortical excitatory neurons. In the synchronised state, the V_m displays slow fluctuations (Fig. 1.4 **a**) and its probability distribution is characterised by a large variance and a large power in the low frequencies of its power-spectrum. On the other hand, a desynchronised state induces smaller deviations of V_m, a suppression of the variance and of the low frequency peak in the power-spectrum (Poulet and Petersen, 2008; Polack et al., 2013) (Fig. 1.4 **a-b**).

1.1.5 *How do neurons integrate synaptic inputs?*

In the previous section we described the effects of cortical state on the V_m of cortical neurons. Here discuss how changes of the V_m distribution alter the magnitude of the neuronal response as a function of the input amplitude (input-output curve). There are a variety of input-output curves (usually with a sigmoidal shape) depending on the specific context and the experimental paradigm used (Fig. 1.5).

When a neuron undergoes a sustained excitation, the output is generally measured as the firing rate of the neuron. However, the input can take multiple forms: (i) the frequency of the input drive (Rothman et al., 2009) or (ii) the total current received by the neuron (Chance et al., 2002) or even (iii) the strength of an applied sensory stimulus (Ayaz and Chance, 2009) (Fig. 1.5 **a**).

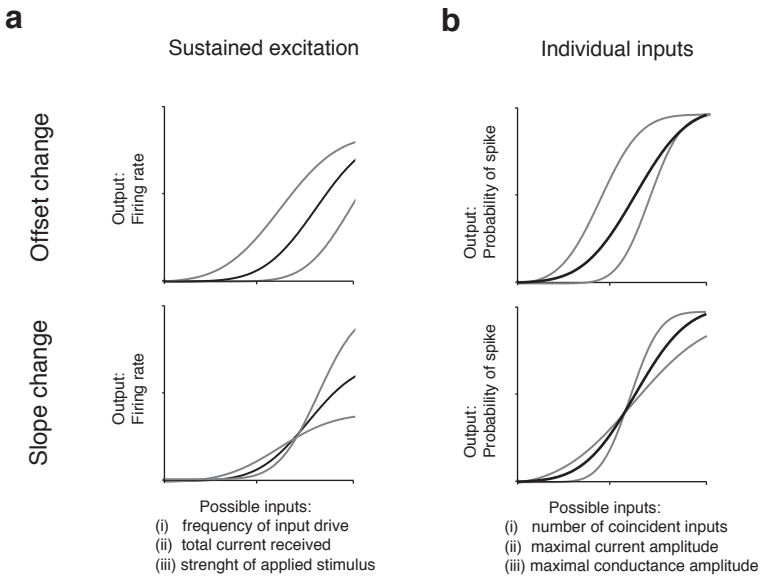

Figure 1.5: Input-output curves, measured by using sustained excitation **(a)** or individual inputs **(b)**. The top row shows offset changes (e.g. translations along the input axis), while the bottom row displays changes in the slope.

When the neuron receives individual inputs, the output is measured as the probability that a spike is evoked in response to an input. In this case, the input axis can represent: (i) the number of coincident inputs (Silver, 2010), or (ii) the maximum amplitude of the inputs measured as a current (Rossant et al., 2011) or (iii) as a conductance (Hô and Destexhe, 2000) (Fig. 1.5 **b**).

Input-output curves might display offset changes (Fig. 1.5 **a-b**, top) or changes in the slope (Fig. 1.5 **a-b**, bottom), which alter the response of the neurons in a non-linear fashion dependent on the input size. An important feature of any input-output transformation is the slope of the relationship, defined as *gain* (Silver, 2010). Unfortunately, this definition is a little confusing as it depends on which input and output we measure and also on which point of the sigmoidal curve we measure the slope. As a result, some researchers prefer talking about *sensitivity* to inputs (Rossant et al., 2011) or *responsiveness* (Destexhe et al., 2003), if excitation is driven by single inputs.

In this thesis I studied the effect of movement on input-output transformation of neurons in M1 of awake mice. Since I measured the input-output curves by exciting neurons with single inputs, I decided to use the terms *sensitivity* and *responsiveness* rather than *gain*.

1.2 A PRIMER ON THE INFERENCE TECHNIQUES

This section is a primer on Bayesian inference techniques, which will be used in Chapter 3. For a comprehensive overview of Bayesian theory, refer to (Barber, 2012; Bishop, 2007).

1.2.1 *Bayes theorem*

Bayes theorem is an algorithm for combining prior experience with current evidence. This is an example of the theorem in action:

> I am on holiday and I want to know whether the girl sitting on the other side of the table studied Physics at University. Without any other knowledge (a *priori*), the probability of the event A = *the girl studied Physics* is $P(A) = 0.01$. During the dinner, I hear that she is talking about input-output transformations in pyramidal neurons and Bayesian inference techniques. Clearly, she is a computational neuroscientist. I define B = *the girl is a computational neuroscientist*. I know that among physicists, computational neuroscience is getting popular and about 1 in every 20 physicists is a computational neuroscientist: the likelihood of my observation is $P(B|A) = 0.05$. To answer my original question, I now have a new piece of evidence and I update my belief to find $P(A|B)$. Bayes theorem simply states that
>
> $$P(A|B) = \frac{P(B|A)P(A)}{P(B)}. \tag{1.1}$$
>
> Considering that computational neuroscientists are in general rare, $P(B) = 0.001$, thanks to Bayes theorem I know that the probability that the girl studied Physics is $P(A|B) = 0.5$.

The key to this example is that I had a prior, $P(A)$, and then I collected new evidence B. By using the likelihood of the observed event $P(B|A)$ and exploiting Bayes theorem I updated my prior and calculated the posterior probability $P(A|B)$.

In general, given a model with parameters $\boldsymbol{\theta}$, a set of data $\boldsymbol{D}$ and an understanding of the process generating $\boldsymbol{D}$, we can calculate:

$$P(\boldsymbol{\theta}|\boldsymbol{D}) = \frac{P(\boldsymbol{D}|\boldsymbol{\theta})P(\boldsymbol{\theta})}{P(\boldsymbol{D})}. \tag{1.2}$$

If we have:

- a generative model that allows us to compute the likelihood $P(\boldsymbol{D}|\boldsymbol{\theta})$ of the data given the model parameters,
- a prior expectation on the values of the parameters $P(\boldsymbol{\theta})$,

it is possible to calculate the posterior probability of the parameters, given the evidence $P(\boldsymbol{\theta}|\boldsymbol{D})$. The most probable value of the parameters is $\boldsymbol{\theta}^* = \text{argmax}_{\boldsymbol{\theta}} P(\boldsymbol{\theta}|\boldsymbol{D})$, which is called maximum a posteriori solution (MAP). For a flat prior, it is equivalent to the maximum likelihood solution (ML), which is $\boldsymbol{\theta}^* = \text{argmax}_{\boldsymbol{\theta}} P(\boldsymbol{D}|\boldsymbol{\theta})$.

Notably, the denominator of 1.2 does not depend on $\boldsymbol{\theta}$, thus the posterior is proportional to the joint distribution:

$$\begin{aligned} P(\boldsymbol{\theta}|\boldsymbol{D}) &\propto P(\boldsymbol{D}|\boldsymbol{\theta})P(\boldsymbol{\theta}) \\ &\propto P(\boldsymbol{D}, \boldsymbol{\theta}). \end{aligned} \tag{1.3}$$

In practice, the goal of the inference is to estimate the joint distribution. To construct $P(\boldsymbol{D}, \boldsymbol{\theta})$, we need an understanding of the underlying process and reproduce it for example in a graphical model.

1.2.2 *Graphical models*

A concise way to represent our knowledge of the process is a directed acyclical graph (a graph with no loops), also called probabilistic graphical model or Bayesian network. Here is a short guide on how to build graphical models:

1. variables are represented by nodes in the graph, while dependencies between variables are represented by arrows,
2. variables are both data, $\boldsymbol{D} = \{d_1, d_2, \ldots\}$, and parameters of the model $\boldsymbol{\theta} = \{\theta_1, \theta_2, \ldots\}$,
3. when a variable A has an influence on variable B (e.g. in the graph there is an arrow going from A to B), the node A is said to be *parent* of node B,
4. if two nodes are not directly connected, they are conditionally independent given their parents,
5. the graph should not have recursive connections, it has to be acyclical.

Making the dependencies between variable explicit simplifies the calculation of the joint probability. Let's call all the variables $\boldsymbol{n} = \{n_1, n_2, \ldots\}$ (pulling together $\boldsymbol{D}$ and

$\boldsymbol{\theta}$). The chain rule allows writing the joint probability as the product of the conditional probabilities:

$$P(n_1, \ldots, n_k) = \prod_{i=1}^{k} P(n_i | n_{i+1}, \ldots, n_k). \tag{1.4}$$

However, since unconnected nodes are conditionally independent given their parents, we can simplify Eq. 1.4:

$$P(n_1, \ldots, n_k) = \prod_{i=1}^{k} P(n_i | \text{Parents}(n_i)). \tag{1.5}$$

To estimate the posterior, a brute force method is to create a grid with all the possible combination of parameter values (an m dimensional grid if we have m parameters), and for each combination calculate $P(\boldsymbol{\theta}, \boldsymbol{D})$. This method becomes computationally unfeasible even with a modest number of parameters. Luckily, the posterior distribution can be explored with sampling methods like the Markov Chain Monte Carlo (MCMC).

1.2.3 *Sampling the posterior probability*

In brief, MCMC algorithms generate a random walk in the parameter space in such a way that points are visited with a frequency that is proportional to a given probability distribution. In this way, we avoid wasting time in low-probability region of space. A formal description of the available MCMC algorithms is beyond the scope of this section and I advise the interested reader to refer to Barber (2012); Bishop (2007); Dumoulin and Thouin (2014).

One of the main features of the Bayesian approach is that it does not give a mere point-like estimation of the parameters (e.g. ML). By sampling, we obtain the full posterior probability of the parameter space that allows us (i) to express our confidence in the parameter values and (ii) to examine correlations between the probability distribution of the parameters. This is key to evaluate which parameters are really important in the model (their probability distribution will have a sharp peak) and which ones are only marginal (their probability distribution will be broad, meaning that a large range of values can explain equally well the data).

1.2.4 *Model comparison*

The second advantage is that the Bayesian framework allows us to compare competing models and select which one better describes the data.

Assume that you have two models and you want to assess which one better fits the data. Formally, you want to calculate:

$$\frac{P(M_1|\boldsymbol{D})}{P(M_2|\boldsymbol{D})} = \frac{P(\boldsymbol{D}|M_1)}{P(\boldsymbol{D}|M_2)}\frac{P(M_1)}{P(M_2)}. \tag{1.6}$$

The term on the left represent the posterior odds (the ratio of the posterior probabilities of the two models), the first term on the right is called the Bayes factor and the second term on the right is the prior odds. If we assume that *a priori* the two models are equally probable, we just need to calculate the Bayes factor. Each term is:

$$P(\boldsymbol{D}|M_i) = \int P(\boldsymbol{D}|\boldsymbol{\theta}, M_i)P(\boldsymbol{\theta}|M_i)d\boldsymbol{\theta}. \tag{1.7}$$

This integral is usually impossible to compute and we need to adopt approximation methods.

A popular method is called Bayesian Information Criteria (BIC). In practice, we approximate the log of the model likelihood as:

$$\log P(\boldsymbol{D}|M_i) \simeq \log P(\boldsymbol{D}|\boldsymbol{\theta}^*, M_i) - \frac{K}{2}\log(N), \tag{1.8}$$

where $\boldsymbol{\theta}^*$ are the ML values of the parameters, K is the number of parameters and N the number of data points. This crude approximation is equal to the probability of the ML solution minus a penalty term proportional to the number of parameters, which punishes complex models. The BIC is then calculated as:

$$\begin{aligned} \text{BIC} &= -2\log P(\boldsymbol{D}|M_i), &(1.9)\\ &= -2\log P(\boldsymbol{D}|\boldsymbol{\theta}^*, M_i) + K\log(N) &(1.10)\end{aligned}$$

and a high BIC implies a poor fitting of the data.

To compare two models M_1 and M_2, we calculate $\Delta\text{BIC} = \text{BIC}_1 - \text{BIC}_2$. Usually, we consider M_1 significantly better than M_2 if $\Delta\text{BIC} < -10$ (Bishop, 2007).

The Deviance Information Criteria (DIC) is a popular approximation when the inference is performed with MCMC sampling (Spiegelhalter et al., 2002). While the BIC just takes into account the ML solution, the DIC makes use of all the samples

from the posterior. We define the deviance as $D(\boldsymbol{\theta}) = -2 \log P(\boldsymbol{D}|\boldsymbol{\theta})$. The DIC is computed as

$$\text{DIC} = 2\overline{D(\boldsymbol{\theta})} - D(\bar{\boldsymbol{\theta}}), \tag{1.11}$$

where $\overline{D(\boldsymbol{\theta})}$ is the average of the deviance of the samples and $D(\bar{\boldsymbol{\theta}})$ is the deviance calculated for a good estimator of $\boldsymbol{\theta}$, for example the ML value $\boldsymbol{\theta}^*$. The idea is that models which have peaked probabilities are favoured over those which have broad probabilities (as $\overline{D(\boldsymbol{\theta})}$ is lower). However, to penalise overfitting complex models, it is introduced the term $-D(\bar{\boldsymbol{\theta}})$, which is strongly positive if the ML solution is too accurate.

Similarly to the BIC case, to compare two models we calculate ΔDIC and the significance threshold is $\Delta\text{DIC} < -10$.

1.2.5 *Useful libraries*

There are several software libraries and tutorials which allow the user to easily implement Bayesian models and perform inference with a variety of MCMC algorithms.

I strongly recommend to the interested reader an open source book that can be found on-line (Davidson-Pilon, 2014). This book, which is actually a collaborative GitHub project, is an excellent introduction to Bayesian inference using PyMC, a python module that implements Bayesian statistical models and fitting algorithms (Patil et al., 2010).

1.3 THESIS LAYOUT

The work is organised as follows. In Chapter 2, I introduce the mathematical description of the most simple neural model, deriving the equations that link the statistics of its inputs to those of the membrane potential. I will exploit these calculations in Chapter 3, when I describe a probabilistic method that I implemented to infer the statistics of the inputs to a neuron from *in vivo* voltage-clamp traces. The experimental work is in Chapter 4: I performed whole-cell recordings in the motor cortex of awake mice and applied analytical and computational models to describe the findings. In Chapter 5 I discuss the findings of this thesis and suggest new experiments.

2

STATISTICAL PROPERTIES OF THE MEMBRANE POTENTIAL

In this chapter I present the calculations that relate input statistics to the statistics of the membrane potential (V_m) in one of the most simple neural models: the single compartment passive neuron. In this approximation, the whole geometry of the neuron collapses to one point in space and the membrane behaves as a low pass filter on the synaptic current. Despite its simplicity, this model is useful for ball-park estimations of the net effect of the currents in the soma of a neuron (Gerstner and Naud, 2009). I first introduce the mathematical description of the single compartment model, see e.g. (Koch, 1999; Bialek et al., 1999; Gerstner and Kistler, 2002), then I present an extension with my own calculations that will be applied in chapter 3 and 4.

2.1 SINGLE COMPARTMENT MODEL OF A NEURON

In first approximation, a neuron is a leaky integrator with a resting membrane potential E_L:

$$C\frac{dV_m(t)}{dt} = G_L\Big(E_L - V_m(t)\Big) + I_{ext}(t), \tag{2.1}$$

where C is the capacitance of the neuron, $V_m(t)$ the membrane potential, G_L is the leak conductance and $I_{ext}(t)$ is any external current which is applied to the neuron. Eq. 2.1 can be rewritten as

$$\tau_m\frac{dV_m(t)}{dt} = \Big(E_L - V_m(t)\Big) + \frac{I_{ext}(t)}{R_{in}}, \tag{2.2}$$

with $R_{in} = 1/G_L$ being the input resistance and $\tau_m = R_{in}C$ the membrane time constant. In practice, in absence of external currents, whenever the $V_m(t)$ is different from E_L, a current flows through the membrane until the resting state E_L is reached.

I now describe the synaptic inputs, which represent excitatory and inhibitory signals coming from other neurons.

2.1.1 *Conductance based synapses*

In a conductance based model (COBA), synapses are modelled as transient changes of conductance at a particular reversal potential, which differs according to the synapse type. The current flowing through a synapse is defined as

$$I_x(t) = g_x(t)\Big(E_x - V_m(t)\Big), \tag{2.3}$$

where $g_x(t)$ is the transient change of conductance and E_x is the reversal potential of a synapse of type x, which can be either excitatory (E or inhibitory I) and the last term on the right hand side is generally called the driving force of the synapse. The shape of a transient conductance change due to a synaptic input coming at time t_k is commonly described by a bi-exponential function (Schutter, 2009):

$$g_x(t - t_k) = (1 - e^{-(t-t_k)/\tau_{1_x}})e^{-(t-t_k)/\tau_{2_x}}\mathcal{H}(t), \tag{2.4}$$

where τ_{1_x} and τ_{2_x} are the rise and decay time constants and $\mathcal{H}(t)$ is the Heaviside function.

Now I add the synaptic currents to the passive equation 2.1 to obtain

$$C\frac{dV_m(t)}{dt} = G_L\Big(E_L - V_m(t)\Big) + G_E(t)\Big(E_E - V_m(t)\Big) + G_I(t)\Big(E_I - V_m(t)\Big). \tag{2.5}$$

$G_E(t)$ and $G_I(t)$ are the total excitatory and inhibitory conductances, sum of the individual events:

$$G_x(t) = \sum_{p_x}\sum_{k_p} a_{k_p} g_x(t - t_{k_p}), \tag{2.6}$$

where the sum is over all the P input neurons of the type x and a_{k_p} is the amplitude of the event k of the neuron p taking place at time t_{k_p}.

We define the spike train of the input neuron p as

$$S_p(t) = \sum_{k_p} \delta(t - t_{k_p}), \tag{2.7}$$

and the amplitude weighted spike train of the neuron p as

$$W_p(t) = \sum_{k_p} a_{k_p}\delta(t - t_{k_p}). \tag{2.8}$$

Now we rewrite Eq. 2.6 as the convolution between the shape of the synaptic input (Eq. 2.4) and the amplitude weighted spike train (Eq. 2.8):

$$G_x(t) = \sum_{p_x} \int_{-\infty}^{+\infty} g_x(s) W_p(t-s) ds. \tag{2.9}$$

This last equation will be important to calculate the power spectrum of the membrane potential in section 2.3.

2.1.2 *Effective input resistance*

A very useful quantity is the effective input resistance R_{eff}, which is widely used in both experimental and computational literature.

$$\begin{aligned} R_{eff} &= \frac{1}{\langle G_{tot} \rangle}, \\ &= \frac{1}{G_L + \langle G_{syn} \rangle}, \\ &= \frac{1}{G_L + \langle G_E \rangle + \langle G_I \rangle}, \end{aligned} \tag{2.10}$$

where $\langle \cdot \rangle$ indicates a temporal average

$$\langle x \rangle = \lim_{T \to \infty} \frac{1}{T} \int_0^T x(t) dt, \tag{2.11}$$

and we made use of $\langle G_{syn} \rangle = \langle G_E \rangle + \langle G_I \rangle$ (the average total synaptic conductance) and $\langle G_{tot} \rangle = \langle G_{syn} \rangle + G_L$ (average total conductance).

R_{eff} can be defined as the effective resistance seen by a current injected in the neuron[1]. By analogy, we define the effective membrane time constant as

$$\tau_{eff} = R_{eff} C. \tag{2.12}$$

In vivo, $\langle G_{syn} \rangle$ can be large respect to G_L (Haider et al., 2012; Destexhe et al., 2003). As a result, the effective input resistance is significantly lower, meaning synaptic in-

1 Please note that we are modelling a point-like neuron, where all the synapses are in the same location. In a real neuron, the axial resistance of the dendritic tree makes R_{eff} more difficult to interpret. Each synapse will experience a *local* R_{eff} which depends on its position in the neuron and on the filtering effect of the axial resistance. When we talk about R_{eff}, we need to keep in mind that it refers to the effective resistance seen by a current injected in the soma. Potentially, this has little to do with the resistance seen by the individual synapses located far from the soma.

puts *in vivo* produce smaller voltage deflections with faster membrane time constant when compared to the equivalent inputs *in vitro*.

2.2 FIRST ORDER STATISTICS

The first order statistics of the membrane potential can be derived by calculating the stationary case, $dV(t)/dt = 0$, of Eq. 2.5:

$$0 = G_L\Big(E_L - \langle V_m\rangle\Big) + \langle G_E\rangle\Big(E_E - \langle V_m\rangle\Big) + \langle G_I\rangle\Big(E_I - \langle V_m\rangle\Big). \tag{2.13}$$

The average membrane potential $\langle V_m\rangle$is:

$$\begin{aligned}\langle V_m\rangle &= \frac{G_L E_L + \langle G_E\rangle E_E + \langle G_I\rangle E_I}{\langle G_{tot}\rangle} \\ &= R_{eff}\Big(G_L E_L + \langle G_E\rangle E_E + \langle G_I\rangle E_I\Big).\end{aligned} \tag{2.14}$$

We can also express the average synaptic conductances $G_x(t)$ in terms of the frequency, shape and amplitude of the synaptic inputs. The temporal average of Eq. 2.9 is

$$\langle G_x(t)\rangle = \lambda_x \mu_{a_x} \frac{\tau_{2_x}^2}{\tau_{1_x} + \tau_{2_x}}, \tag{2.15}$$

where μ_{a_x} is the mean of the distribution of the synaptic input amplitudes.

By combining Eq. 2.10 and 2.14, we can write the expression for the excitatory and inhibitory input conductances:

$$\langle G_E\rangle = \frac{\Big(\langle V_m\rangle - E_L\Big)\langle G_{tot}\rangle - \langle G_{syn}\rangle\Big(E_I - E_L\Big)}{E_E - E_I}, \tag{2.16}$$

$$\langle G_I\rangle = \frac{\Big(\langle V_m\rangle - E_L\Big)\langle G_{tot}\rangle - \langle G_{syn}\rangle\Big(E_E - E_L\Big)}{E_I - E_E}. \tag{2.17}$$

Eq. 2.16 and 2.17 are very important for chapter 4. By measuring $\langle V_m\rangle$ and $\langle G_{tot}\rangle$ *in vivo* and estimating G_L and E_L from literature, I could infer the average excitatory and inhibitory conductances - see Anderson et al. (2000) for a similar method.

2.3 POWER SPECTRUM AND SECOND ORDER STATISTICS

The power spectrum of a signal $y(t)$ is

$$P_y(\omega) = 2\widehat{y}(\omega)^*\widehat{y}(\omega) = 2|\widehat{y}(\omega)|^2, \tag{2.18}$$

where * denotes the complex conjugation and $\widehat{y}(\omega)$ is the Fourier tramsform of $y(t)$

$$\widehat{y}(\omega) = \mathcal{F}\{y(t)\} = \int_{-\infty}^{+\infty} y(t)e^{-2\pi i t\omega}dt. \tag{2.19}$$

2.3.1 *Power spectrum of the conductances*

We first calculate the power spectrum of the conductance $G_x(t)$. The Fourier transform of Eq. 2.9 is

$$\mathcal{F}\{G_x(t)\} = \sum_{p_x} \widehat{g_x}(\omega)\widehat{W_p}(\omega), \tag{2.20}$$

and the power spectrum is

$$P_{G_x}(\omega) = 2\left(\sum_{p_x} \widehat{g_x}(\omega)\widehat{W_p}(\omega)\right)^* \left(\sum_{p_x} \widehat{g_x}(\omega)\widehat{W_p}(\omega)\right) \tag{2.21}$$

$$= 2|\widehat{g_x}(\omega)|^2 \sum_{p_x} |\widehat{W_{p_x}}(\omega)|^2, \tag{2.22}$$

$$= 2N_x|\widehat{g_x}(\omega)|^2|\widehat{W_x}(\omega)|^2, \tag{2.23}$$

where in the last line we assumed that the N_x input spike trains are uncorrelated and statistically indistinguishable input spike trains p.

We can now expand the last term $|\widehat{W_x}(\omega)|^2$ by making use of Eq. 2.8. If the amplitude of the events a_k is independent from the underlying stochastic process, we have

$$P_{G_x}(\omega) = 2N_x\overline{a_x^2}|\widehat{g_x}(\omega)|^2|\widehat{S_x}(\omega)|^2. \tag{2.24}$$

In practice, the term $|\widehat{S_x}(\omega)|^2$ is the power spectrum of the stochastic process underlying the time series of the spike trains. A common choice to describe neural firing in the cortex is the uniform Poisson train, see (Koch, 1999; Gerstner and Kistler, 2002), but also (Lindner, 2006). Hence, we have $|\widehat{S_x}(\omega)|^2 = \lambda_x + 2\pi\lambda_x^2\delta(\omega)$, where λ_x is the

average firing rate of the neurons in population x. For non-zero frequencies Eq. 2.24 becomes:

$$P_{G_x}(\omega) = 2N_x\lambda_x(\mu_{a_x}^2 + \sigma_{a_x}^2)|\widehat{g_x}(\omega)|^2, \tag{2.25}$$

where σ_{a_x} is the standard deviation of the distribution of the synaptic input amplitudes.

For the bi-exponential kernel in Eq. 2.4, we have

$$|\widehat{g_x}(\omega)|^2 = \frac{\tau_{2_x}^4}{(\tau_{1_x} + \tau_{2_x})^2 + (\omega\tau_{2_x})^2(2\tau_{1_x}^2 + 2\tau_{1_x}\tau_{2_x} + \tau_{2_x}^2) + (\omega\tau_{2_x})^4\tau_{1_x}^2}. \tag{2.26}$$

2.3.2 *Power spectrum of the membrane potential*

We can compute the power spectrum of the current coming from population x by assuming that the changes of V_m are small compared to the distance between V_m and reversal potential of the synapses[2], so that Eq. 2.3 becomes:

$$I_x(t) = G_x(t)\Big(E_x - \langle V_m\rangle\Big). \tag{2.27}$$

Thus, the power spectrum of the current is:

$$P_{I_x}(\omega) = P_{G_x}\Big(E_x - \langle V_m\rangle\Big)^2. \tag{2.28}$$

We now write down the equation describing the power spectrum of the total current:

$$P_I(\omega) = P_{I_E}(\omega) + P_{I_I}(\omega) + 2P_{I_{IE}}(\omega), \tag{2.29}$$

where

$$P_{I_{IE}} = P_{G_{IE}}\Big(E_E - \langle V_m\rangle\Big)\Big(E_I - \langle V_m\rangle\Big) \tag{2.30}$$

2 This approximation is in principle dangerous, because *in vivo* the fluctuations of the membrane potential have usually a large standard deviation. However, in Sec. 2.3.3 I will show that this approximation works well in practice.

is the cross-spectrum between excitatory and inhibitory current and interestingly has a negative value (the condition $E_I < \langle V_m \rangle < E_E$ is always satisfied). The cross-spectrum of the conductances $P_{G_{IE}}$ is

$$\begin{aligned} P_{G_{IE}} &= \widehat{G_E}(\omega)^* \widehat{G_I}(\omega), \\ &= N_E N_I \left(\widehat{g_E}(\omega)^* \widehat{g_I}(\omega) \right) \left(\widehat{W_E}(\omega)^* \widehat{W_I}(\omega) \right). \end{aligned} \tag{2.31}$$

V_m deflections are caused by the synaptic current flowing through the membrane, which is a low pass filter. From Eq. 2.2, taking into account the effect of the synaptic inputs on membrane time constant and input resistance, the filter has the form

$$\widehat{M}(\omega) = \frac{R_{eff}}{1 + i\omega\tau_{eff}}. \tag{2.32}$$

Thus, the power spectrum of V_m is:

$$\begin{aligned} P_{V_m} &= |\widehat{M}(\omega)|^2 P_I(\omega), \\ &= \frac{R_{eff}^2}{1 + (\omega\tau_{eff})^2} P_I(\omega). \end{aligned} \tag{2.33}$$

Eq. 2.33 is very general and, in principle, allows the calculation of the power spectrum of V_m for any input statistics. For example, we could choose spike trains which do not have uniform Poisson statistics, or that are correlated. What is important is to be able to compute the power spectra and cross-spectra of the trains and plug them in Eq. 2.24 and 2.31.

From the power spectrum, we can calculate the variance $\sigma^2_{V_m}$ of V_m as:

$$\sigma^2_{V_m} = \int_0^\infty P_{V_m}(\omega) d\omega, \tag{2.34}$$

which has an analytical, but rather intimidating, solution.

2.3.3 *Validation of the model*

By using computational simulations, I show that this model correctly describes the power spectral density of a conductance based single compartment leaky neuron.

The simulated neuron had the following parameters: $C = 100$ pC, $G_L = 5$ nS, $E_L = -62$ mV, $E_E = 0$ mV, $E_I = -75$ mV. The excitatory and inhibitory synapses had respectively 3 ms and 10 ms time constant, with lognormally distributed amplitudes with parameters $\mu_a = 60$ nS and $\sigma_a = 60$ nS. We stimulated the neuron with

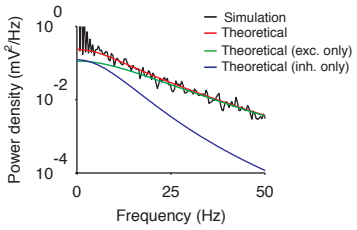

Figure 2.1: Simulated power density (black), superimposed on the theoretical prediction of the model (red). In green and blue the contribution of the excitatory and inhibitory synapses respectively.

8000 Hz excitatory inputs and 1500 Hz inhibitory inputs. In Fig. 2.1 we show the power spectral density of the simulated neuron (black) superimposed on the theoretical prediction of the model (red). The inhibition, as expected, contributes to the power spectrum predominantly in the low frequencies, due to the longer time constant of inhibitory synapses. Higher frequencies of the power spectrum are almost exclusively due to the excitatory synapses.

2.4 CONCLUSION

In summary, in this chapter we have derived the equations that link frequency, shape and amplitude of the synaptic inputs to the first and second order statistics of the membrane potential. We have used a simple neural model, where the neuron does not have any spatial extension (point model) and does not have active conductances, because $g_x(t)$ does not depend on the voltage. This means that synaptic inputs sum up linearly and are neither enhanced, nor suppressed while travelling along the dendritic tree.

Clearly, this is not a realistic approximation, as we know that dendritic processing is an important element for computation (London and Hausser, 2005). Synaptic inputs can sum up both sub-linearly and supra-linearly, depending on their amplitude, location and relative timing (Poirazi et al., 2003; Polsky et al., 2004) by triggering active conductances and dendritic spikes also *in vivo* (Helmchen et al., 1999; Häusser et al., 2000).

Hence, we need to be careful when interpreting results obtained from the single compartment passive neural model. When we talk about frequency, shape and amplitude of the inputs, we should refer to the net effect that they have on the soma, after the dendritic processing. Including dendritic non-linearities in the model would make analytical approximations intractable and would require computationally expensive simulations (Hines and Carnevale, 1997). The simple approximation used in

this chapter is still very useful to quickly obtain rough estimations of the net effect of inputs to the soma of a neuron. Caution should also be used when interpreting the effective input resistance measured *in vivo*. In fact, it refers to the resistance measured at the soma, which might have little to do with the effective resistance seen by the synapses located in the distal part of the dendritic tree.

More advanced theoretical approaches, such as the *ball and stick* neuron (Rall, 1959), address the fundamental limitation of the point-neuron model. Here, the soma is provided with a single resistive cable (the stick) which receives the synaptic inputs. Assuming that the spatial distribution of the synapses is known, it is possible to solve analytically the equations describing the voltage in the soma. This approach relies on safer assumptions, but it would bring two problems: (i) the analytical treatment, although possible, becomes much more difficult (see for example this recent work Pettersen et al. (2014)), and it is an avenue of research by itself; (ii) the goodness of the model relies on the knowledge of the spatial distribution and activity of the synaptic contacts, which are not always available. For these reasons, in the framework of this thesis, I decided to use the simple point-neuron model. Unfortunately, the interpretation of the results is more difficult, because it relies on assumptions that are in practice violated.

The results obtained in this chapter are crucial for the inference techniques developed in chapter 3 and for the calculations of chapter 4.

3

PROBABILISTIC INFERENCE OF *IN VIVO* SYNAPTIC INPUT STATISTICS FROM VOLTAGE-CLAMP DATA

3.1 INTRODUCTION

Whole-cell recordings in awake animals are rapidly becoming a powerful tool to characterise how neurons integrate synaptic inputs to generate behaviourally relevant spike output patterns (Chorev et al., 2009; Long and Lee, 2012). To extract the most information from this precious data, developing new analysis tools is key. First I describe a method we developed to infer the statistics of synaptic inputs to a neuron from *in vivo* voltage-clamp recordings. Then, as a proof of concept, I applied it to real data. In theory, with this technique one could analyse any good quality voltage-clamp recording (also in motor cortex, which is the main object of this thesis). In practice, as I will explain in the following, it is technically difficult to obtain good quality data from large pyramidal neurons due to their considerable size. Thus, I decided to analyse voltage-clamp traces of cerebellar molecular layer interneurons, which have a compact morphology.

3.1.1 *Voltage-clamp recordings*

Voltage-clamp recordings were developed more than sixty years ago by Marmont (1949), who recorded in squid giant axons. With the introduction of the whole-cell patch-clamp technique in the late seventies (Neher and Sakmann, 1976), in the voltage-clamp configuration one could measure the sum of all synaptic and intrinsic currents as seen at the soma. While under normal conditions V_m changes according to the currents the cell receives, in voltage-clamp current is injected to fix the voltage at a set point. In practice, V_m is measured, compared to the desired value V_{clamp} and an external current I_{clamp} is injected to minimize the difference $(V_m - V_{clamp})$. The current injected is

$$I_{clamp} = g(V_{clamp} - V_m), \tag{3.1}$$

where ideally g is an infinite gain, so to instantaneously bring $V_m = V_{clamp}$.

In the Ohmic approximation, synaptic currents are proportional to the transient conductance change ($g(t)$, due to the opening of the ion channels) multiplied by the driving force $(E - V_m(t))$, which is the difference between the reversal potential of the synapse E and the voltage in proximity of the synapse

$$I(t) = g(t)\Big(E - V_m(t)\Big). \tag{3.2}$$

If we clamp the voltage of the entire neuron at exactly the reversal potential of a given synapse, the driving force goes to zero and the synaptic current is suppressed. This method is, in principle, very powerful because makes it possible to record the contribution of excitatory or inhibitory currents in isolation. If, for example, we clamp the voltage at the reversal potential of inhibition $E_{clamp} = E_I = -70\text{mV}$[1], the synaptic current is:

$$\begin{aligned} I_{syn}(t) &= G_I(t)\Big(E_I - E_{clamp}\Big) + G_E(t)\Big(E_E - E_{clamp}\Big), \\ &= 0 + G_E(t)\Big(E_E - E_{clamp}\Big). \end{aligned} \tag{3.3}$$

In order to clamp the voltage of the soma, we need to inject a current I_{clamp} which is equal in amplitude, but opposite in sign to I_{syn}, so that the total current flow is zero and the V_m is kept constant. Therefore, by measuring I_{clamp}, we can estimate $I_{syn} \simeq -I_{clamp}$, which in first approximation is proportional to the synaptic conductance.

This technique has a number of known issues.

- To measure V_m and inject at the same time and with the same electrode an external current, capacitance and resistance of the electrode and membrane have to be adequately compensated. A full compensation might result in instability of the circuit and usually only a partial compensation is performed (Brette and Destexhe, 2012).
- Due to residual capacitive currents in the system, the gain of Eq. 3.1 cannot be infinitely large and fast, therefore the voltage-clamp is not perfect (Brette and Destexhe, 2012).
- The V_m can be clamped in only one point in space, in proximity of the electrode tip. The periphery of the neuron might not be clamped at the desired voltage (space-clamp errors) due to the resistive nature of dendritic cables which at-

1 $E_I = -70$ mV is a standard value as reverse potential of GABA_A receptors, the most common source of inhibition in pyramidal neurons. However, the exact value of the reverse potential depends on the intracellular solution.

tenuate the propagation of the electric current. Imperfect space-clamp leads to systematic errors in the estimation of the synaptic currents, because it results in a mixture of excitatory, inhibitory and active dendritic currents (Williams and Mitchell, 2008). The space-clamp problem is particularly severe in neurons with large dentritic branches, such as pyramidal cells in the cortex, even when the internal solution contains ion channel blockers to reduce leak currents and suppress active conductances (Williams and Mitchell, 2008).

In the last decade, many studies have been using voltage-clamp data from anaesthetised animals to investigate the contribution of excitation and inhibition to the V_m dynamics. Among others, recordings were performed in auditory cortex (Wehr and Zador, 2003; Poo and Isaacson, 2009; hua Liu et al., 2010a), visual cortex (hua Liu et al., 2010b) and pre-frontal cortex (Haider et al., 2006). However, experiments in awake preparations are more problematic, because movements of the animal often introduce vibrations to the electrode which undermine the stability of the recording, which is pivotal in voltage-clamp configuration. At the present time, to the best of my knowledge, only one study investigated excitatory and inhibitory contributions performing voltage-clamp recordings in the primary visual cortex of awake mice (Haider et al., 2012).

In this chapter, I use voltage-clamp traces of molecular layer interneurons recorded in the cerebellum of awake mice[2]. Cerebellar interneurons, unlike pyramidal neurons, have a more compact morphology which makes the cell electrotonically compact reducing space-clamp errors. In principle, the method outlined here could be also applied to good quality voltage-clamp recordings from pyramidal neurons in the cortex, provided that the internal solutions of the electrodes contains Na and K channels blockers to reduce (but unfortunately never completely remove) space-clamp errors (Haider et al., 2006). However, as described above, special caution would be required in interpreting voltage-clamp data from large pyramidal neurons.

3.1.2 *Which mechanisms underlie the increase in excitatory current in cerebellar interneurons during movement?*

Voltage-clamp traces of molecular layer interneurons recorded in the cerebellum of awake head fixed mice during quiet wakefulness and self paced movement[3] display a steady increase of average excitatory current when mice are moving (Fig. 3.1 **a-b**). This effect might be explained by a combination of different mechanisms:

2 These data were collected and generously shared by M. Jelitai from the Duguid Lab. (Edinburgh)

3 In brief, the mice were head-restrained mounted on a single axis, cylindrical treadmill. Movements were detected with a high speed camera. The cells were clamped at -70 mV.

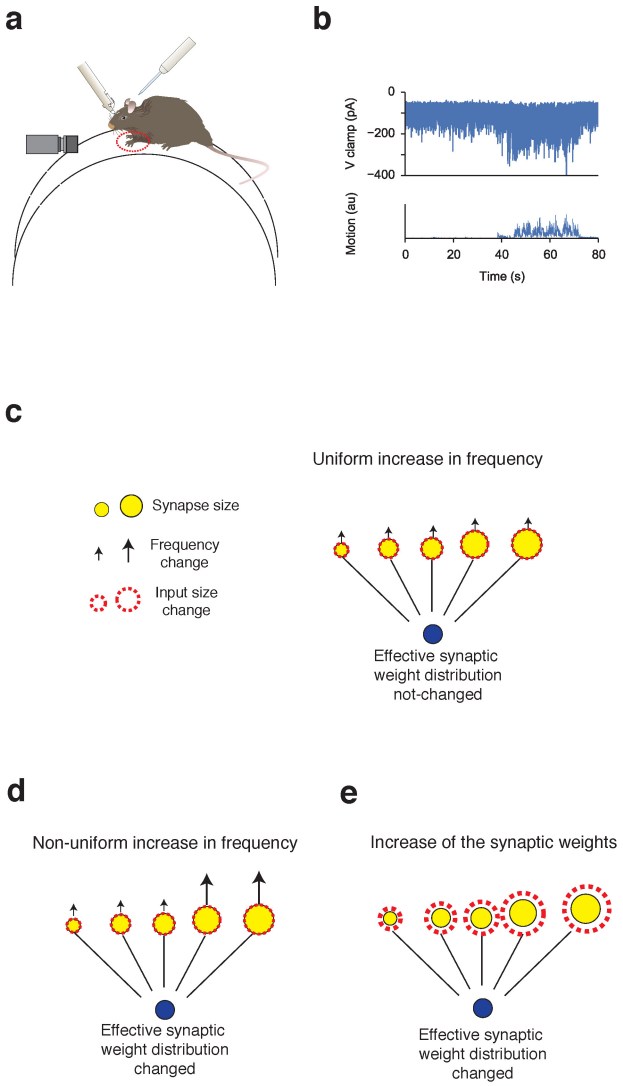

Figure 3.1: Possible mechanisms underlying the increase in excitatory current in cerebellar molecular layer interneurons during locomotion. **a)** Patch-clamp recording configuration in head-fixed mice mounted on a single axis, cylindrical treadmill. Digital imaging (60 fps) was used to confirm changes in behavioral state – quiet wakefulness to movement – and to calculate motion index. **b)** representative voltage clamp trace recorded in a cerebellar interneuron in an awake mouse. We use the motion index (bottom panel) to distinguish between quiet wakefulness or movement periods. **c-e)** Schematics displaying possible mechanisms underlying the increase in excitatory current observed in **(a)**. **c)** uniform increase of synaptic input frequency, **d)** increase of the input frequency of the large synapses only, **e)** increase of synaptic weights but no increase of input frequency.

1. A uniform increase in the frequency of all synaptic inputs, with no change in synaptic weight amplitude (Fig. 3.1 **c**). In this case, interneurons would receive a global and uniform increase in synaptic inputs during movement.

2. A preferential increase in input frequency of larger synapses, leading to an increase in both frequency and amplitude of synaptic inputs (Fig. 3.1 **d**). This could suggest a preferential routing of information, where certain synapses become even more active.

3. Increase of the amplitude of the synaptic inputs but no change of the frequency (Fig. 3.1 **e**), as could be the result of pre-synaptic modulation of neurotransmitter release (Gordon and Bains, 2005).

Our goal is to identify the most likely mechanism responsible for the increased excitatory current in interneurons, by measuring how the synaptic weight distribution and the frequency of the inputs change during movement.

3.1.3 *Measuring synaptic input statistics in vivo*

In the Ohmic approximation, voltage-clamp recordings measure the sum of all excitatory (or inhibitory) post-synaptic currents (PSCs) as seen at the soma. In *in vitro* recordings (brain slice or primary cell cultures), PSC rates are low enough to allow direct identification of each synaptic event and to determine their rate, amplitude and kinetics semi-automatically. An example of an analysis tool used to select individual PSCs *in vivo* is TaroTools a custom-written macro in IgorPro[4]. TaroTools runs an event detection algorithm that automatically labels putative PSCs. However, due to the high input frequency *in vivo*, the algorithm is not perfect and the traces have to be manually processed to correct any mistakes. This manual processing is quite time consuming, and even experienced researchers spend more than 1 hour to analyse a 10 second trace - private communication by Jelitai (2014). In the following we will refer to this method as TaroTools assisted (*TTa*).

We argue that analysing the traces with *TTa* is not only time consuming, but it also produces incorrect results. To test this hypothesis, we generated artificial voltage-clamp traces by summing PSCs with identical shape and Poisson time arrival (Fig.

4 Url address: sites.google.com/site/tarotoolsregister/

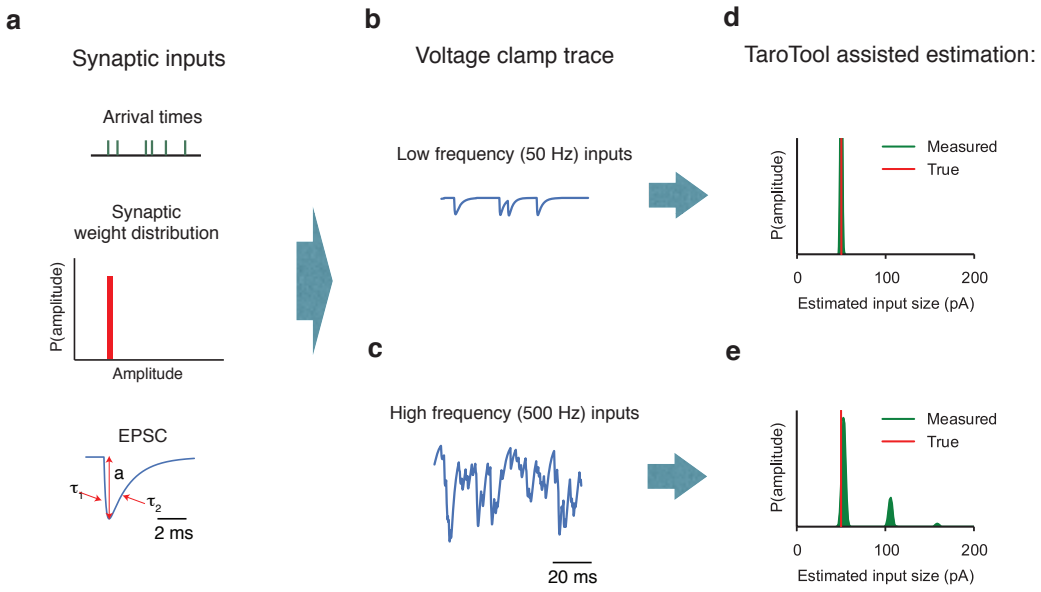

Figure 3.2: Problems in estimating statistics of high frequency synaptic inputs with TaroTools assisted (*TTa*) method. **a**) Generation of a voltage-clamp trace by summing PSCs with identical shape (same amplitude and time constants) and Poissonian time arrival. **b**,**d**) At low input frequencies individual events are well separated and the *TTa* method estimates well the amplitude of the inputs. **c**,**e**) At high input frequency individual PSCs substantially overlap. The *TTa* method classifies near-simulataneous PSCs as a single large event and the probability distribution of the amplitudes incorrectly show multiple peaks.

3.2 **a**). Each event k with amplitude $a_k = 50$ pA is described by a bi-exponential function

$$f(t - t_k) = (1 - e^{-(t-t_k)/\tau_1})e^{-(t-t_k)/\tau_2}\mathcal{H}(t - t_k), \tag{3.4}$$

where $\tau_1 = 0.3$ ms is the rise-time, $\tau_2 = 2$ ms the decay-time and $\mathcal{H}(t)$ the Heaviside function. The rise and decay time chosen are those typical of PSCs in a cereballar interneuron (Szapiro and Barbour, 2007).

When the input frequency is low (50 Hz), each PSC can be correctly detected (Fig. 3.2 **b**) and the resulting estimation of the synaptic input amplitude distribution is correct, with a single sharp peak centered on the true value (Fig. 3.2 **d**).

On the contrary, when the input frequency is higher (500 Hz) individual EPSCs overlap and become indistinguishable (Fig 3.2 **c**). The probability distribution of the amplitude of the PSCs shows smaller peaks at multiples of the original amplitude (Fig 3.2 **e**). This is an indication that multiple near-simultaneous PSCs are classified as a single large PSC. The origin of this problem is that the most probable inter-time interval of a Poisson process, a common model for the inputs received by a neuron,

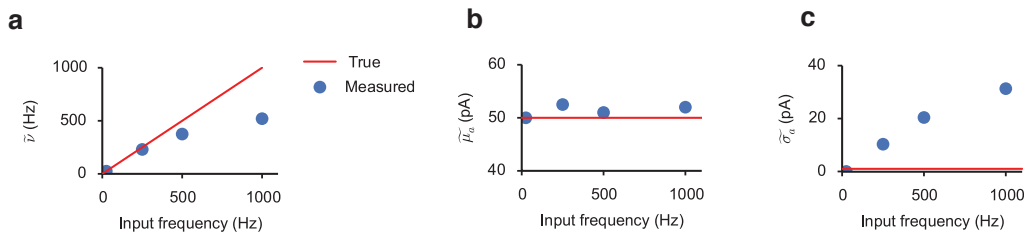

Figure 3.3: The *TTa* method substantially underestimates the frequency of the inputs during sustained synaptic activity. **a**) *TTa* estimated frequency of the inputs $\widetilde{\nu}$ as a function of the real input frequency. **b**) *TTa* estimated mean ($\widetilde{\mu_a}$) and **c**) standard deviation ($\widetilde{\sigma_a}$) of the synaptic input amplitude as a function of the real input frequency.

but see Lindner (2006), is zero.

Thus, we measured how well the *TTa* analysis performs as a function of the input frequency. In particular, we evaluated the estimation of input frequency $\widetilde{\nu}$ (Fig. 3.3 **a**), average input amplitude $\widetilde{\mu_a}$ (Fig. 3.3 **b**) and standard deviation of the input amplitude $\widetilde{\sigma_a}$ (Fig. 3.3 **c**).

At low input frequencies, most of the PSCs are correctly identified and the estimation of the frequency is correct. However, for higher frequencies, the result is grossly underestimated and basically $\widetilde{\nu}$ reaches a plateaux at $\sim$ 500 Hz. In practice, the average human eye cannot resolve two events which are closer than $\sim \tau_2$.

On the other hand, the estimation of the average input amplitude is reasonably correct. The multiple peaks of the distribution (see Fig. 3.2 **e**) do not affect significantly the mean. However, they largely influence the variance, which in reality is zero, because all the PSCs have the same amplitude.

To summarise, our data show that using the *TTa* method gives good results when the input frequency ν is low ($\nu \ll 1/\tau_2$). However, with higher input frequencies, *TTa* substantially underestimates the input frequency and incorrectly predicts the shape of the distribution of the synaptic amplitudes.

In this chapter, we propose a novel probabilistic method which allows a precise inference of the frequency and the distribution of the amplitudes of PSCs *in vivo*.

3.1.4 *Comparing in vivo to in vitro synaptic input frequency and response size distribution*

To avoid confusion with experimental literature, it is important to note that measuring synaptic input frequency and response size distribution *in vivo* is not equivalent to

in vitro. In the latter, connections between a pair of neurons are usually characterised by physical properties, such as the number of contacts (n), maximal conductance for each contact (g) and release probability (p). The weight can be seen as the product ($w = npg$) of those three factors. It thus refers to physical properties that can be individually measured.

By using the voltage clamp approach *In vivo*, it is not possible to isolate inputs coming from a specific pair of neurons and we cannot measure the physical properties of the synaptic contacts. Instead, we measure the amplitude distribution of the response sizes coming from all synaptic contacts.

For example, let's take a neuron that receives inputs from only two upstream neurons with frequency $f_1 = 1$ Hz and $f_2 = 2$ Hz and synaptic weights $w_1 = 5$ pA and $w_2 = 10$ pA. If measured through paired recordings, the synaptic weights distribution $P(w)$ will be:

$$P(w) = \begin{cases} 0.5, & \text{if } w = 5 \text{ pA} \\ 0.5, & \text{if } w = 10 \text{ pA} \\ 0, & \text{otherwise.} \end{cases} \tag{3.5}$$

If we perform the measurement *in vivo*, the synapse of the neuron 2 will be twice as active as the one of the neuron 1. Therefore, our perceived distribution would be:

$$P(w) = \begin{cases} 0.33, & \text{if } w = 5 \text{ pA} \\ 0.67, & \text{if } w = 10 \text{ pA} \\ 0, & \text{otherwise.} \end{cases} \tag{3.6}$$

Therefore, what we really measure *in vivo* is not the actual weight distribution, but the distribution of response sizes, which takes into account the relative frequency of the inputs coming to a specific synaptic site.

3.1.5 *Other probabilistic methods used to estimate synaptic inputs in vivo*

As discussed in chapter 1, *in vivo* whole-cell recordings have become popular during the last decade. The availability of these important data recently prompted computational studies to infer the time-varying course of excitatory and inhibitory synaptic conductances from current-clamp or voltage-clamp recordings.

The early techniques allowed an estimation of the excitatory and inhibitory conductances, $G_E(t)$ and $G_I(t)$, based on the across trial average of variable amplitude

current injections (Borg-Graham et al., 1996; Anderson et al., 2000; Wehr and Zador, 2003). More recently, $G_E(t)$ and $G_I(t)$ can be estimated even from a single trial by applying a diverse range of probabilistic inference methods (Kobayashi et al., 2011; Paninski et al., 2012; Lankarany et al., 2013).

Kobayashi et al. (2011) assumed the size of the excitatory and inhibitory inputs to be identical ($a_e = a_i$), fixed and known *a priori*. Moreover, synaptic inputs are seen as δ functions, with instantaneous rise and decay time and Poissonian time arrival.

Some of the assumptions are relaxed by Paninski et al. (2012), where the number of inputs in a time window dt follows either an exponential or truncated Gaussian distribution. Synaptic inputs have now a decay time constant (τ_{2_E} and τ_{2_I}) which has to be known *a priori*.

Finally, Lankarany et al. (2013) further generalise the distribution of the number of inputs in a time window dt by making use of a mixture of Gaussians. This method allows a good estimation of $G_E(t)$ and $G_I(t)$ even when the distribution of synaptic weights $P(a_k)$ has a long tail.

We highlight that these methods do not estimate directly the frequency and amplitude distribution of the inputs, but they recover the global excitatory and inhibitory conductances. Thus, despite the wealth of information they provide on excitatory and inhibitory conductances, this techniques would not be able to investigate the mechanisms underlying the increase in excitatory current during movement (section 3.1.2).

In this chapter, we propose a probabilistic method to estimate the time constants, frequency and response size distribution of the synaptic inputs. However, unlike the methods described above, we do not obtain a time-varying estimation, but we average the result over a short (few second long) portion of the voltage-clamp recording. We propose that the results obtained with our approach could be used to better constrain the parameters of the time-resolved models described above.

3.2 GENERATIVE MODEL

3.2.1 *Mathematical description of the synaptic current*

The time arrivals of the synaptic inputs t_k are assumed to follow a Poisson process with frequency ν and the shape of each PSC is a double exponential function (Eq. 3.4). We consider all the PSCs having the same time constants, but in section 3.4.4 we examine the effect of heterogeneneous time-constants.

The total current is the sum of the individual PSCs:

$$I(t) = \sum_{k=1}^{K} a_k f(t - t_k), \tag{3.7}$$

where a_k is the amplitude of the PSC.

Although our method is general and could work with any synaptic weight distribution $P(a_k)$, we consider for simplicity the a_k to be distributed as either a log-normal ($L\mathcal{N}$)

$$P(a_k) = L\mathcal{N}(a_k|p_1, p_2) = \frac{1}{p_2\sqrt{2\pi}a_k} e^{-\frac{(\ln a_k - p_1)^2}{2p_2^2}}, \tag{3.8}$$

where (p_1, p_2) are the parameters of the distributions, or a stretched exponential (Exp)

$$P(a_k) = Exp(a_k|p_1, p_2) = \frac{p_1^{-1}}{\Gamma(1 + 1/p_2)} e^{-(a_k/p_1)^{p_2}}, \tag{3.9}$$

(where $\Gamma(\cdot)$ is the Gamma function), or a zero-truncated-normal ($T\mathcal{N}$)

$$P(a_k) = T\mathcal{N}(a_k|p_1, p_2) = p_2^{-1} \frac{\phi(a_k/p_2 + h)}{1 - \Phi(h)}, \tag{3.10}$$

$h = -p_1/p_2$, and $\phi(\cdot)$ and $\Phi(\cdot)$ are respectively the density and cumulative functions of a standardised normal distribution.

These three probability distributions are the most popular choices in experimental and theoretical literature for synaptic strengths: they can represent short tailed ($T\mathcal{N}$ and Exp with $p_2 \gtrsim 1.5$), heavy tailed ($L\mathcal{N}$ and Exp with $p_2 \lesssim 1$) and monotonically decreasing (Exp) distributions (Song et al., 2005a; Buzsáki and Mizuseki, 2014; Barbour et al., 2007).

The mean and standard deviation of the synaptic amplitude, μ_a and σ_a are completely defined by the two parameters p_1 and p_2 of each distribution:

$$\begin{aligned} &L\mathcal{N}: \quad \mu_a = e^{(p_1+\frac{1}{2}p_2^2)}, \quad \sigma_a = \sqrt{(e^{p_2^2}-1)\mu_a^2}; \\ &Exp: \quad \mu_a = \frac{p_1\Gamma(2/p_2)}{p_2\Gamma(1+1/p_2)}, \quad \sigma_a = \sqrt{\frac{p_1^2\Gamma(3/p_2)}{p_2\Gamma(1+1/p_2)} - \mu_a^2}; \\ &T\mathcal{N}: \quad \mu_a = p_1 + p_2\rho, \quad \sigma_a = \sqrt{p_2^2 - p_2^2(\rho^2-\rho h) - (p_1-\rho p_2)^2}, \end{aligned} \tag{3.11}$$

where $\rho = \phi(h)(1-\Phi(h))^{-1}$.

3.2.2 *Moments of the synaptic current*

We now calculate the moments of the synaptic current (Eq. 3.7), which will be used in the next sections. Rice (1954) and Bendat and Piersol (1966) provide an expression to calculate the cumulants k_n of the current probability distribution $P(I)$

$$k_n = \nu\overline{m_a^n}\int_0^{+\infty}[f(t)]^n dt, \tag{3.12}$$

where $\overline{m_a^n}$ are the non-central moments of the distribution $P(a_k)$. The cumulants k_n are related to the standardised central moments of the current M_I:

$$\begin{aligned} \bar{I} &= k_1 \\ \sigma_I &= \sqrt{k_2} \\ \text{skew}(I) &= k_3/k_2^{3/2} \\ \text{kurtosis}(I) &= (k_4+3k_2)/k_2^2 - 3. \end{aligned} \tag{3.13}$$

For $f(t)$ according to Eq. 3.4, the last term of Eq. 3.12 corresponds to the integrals $H_n = \int_0^{+\infty}[f(t)]^n dt$, $(n = 1\ldots 4)$:

$$\begin{aligned} H_1 &= \frac{\tau_2^2}{\tau_1+\tau_2} \\ H_2 &= \frac{\tau_2^3}{2\,(\tau_1+\tau_2)\,(\tau_2+2\tau_1)} \\ H_3 &= \frac{2\tau_2^4}{3(\tau_2+\tau_1)(2\tau_2+3\tau_1)(\tau_2+3\tau_1)} \\ H_4 &= \frac{3\tau_2^5}{4(\tau_2+\tau_1)(3\tau_2+4\tau_1)(\tau_2+4\tau_1)(\tau_2+2\tau_1)}. \end{aligned} \tag{3.14}$$

We now calculate analytically the first four non-central moments $\overline{m_a^n}$, $n = 1 \dots 4$ of every synaptic weight distribution ($L\mathcal{N}$, Exp and $T\mathcal{N}$).

- In the $L\mathcal{N}$ case we have

$$\overline{m_a^n} = e^{np_1 + n^2 p_2^2/2}. \tag{3.15}$$

- For a stretched exponential Exp we have

$$\overline{m_a^n} = \frac{p_1^n \Gamma\Big((1+n)/p_2\Big)}{p_2 \Gamma(1+1/p_2)} \tag{3.16}$$

- In the $T\mathcal{N}$ case, we first compute the central moments $\overline{m_a'^n}$, indicated with the $'$ symbol (Horrace, 2013):

$$\begin{aligned}
\overline{m_a'^1} &= a + \rho b, \\
\overline{m_a'^2} &= b^2 - \rho b^2(\rho - h), \\
\overline{m_a'^3} &= b^3 \rho((\rho - h) + \rho(\rho - h) - 1), \\
\overline{m_a'^4} &= 3b^4(1 - \rho^2(\rho - h)^2 - \rho(\rho - h) - 1/3(h^2\rho(\rho - h) - \rho^2)),
\end{aligned} \tag{3.17}$$

  from which, the non-central moments $\overline{m_a^n}$ of the $T\mathcal{N}$ distribution are calculated as:

$$\begin{aligned}
\overline{m_a^1} &= \overline{m_a'^1}, \\
\overline{m_a^2} &= \overline{m_a'^2} + \overline{m_a'^1}^2, \\
\overline{m_a^3} &= \overline{m_a^3} + 3\overline{m_a'^2}\,\overline{m_a'^1} + \overline{m_a'^1}^3, \\
\overline{m_a^4} &= \overline{m_a'^4} + 4\overline{m_a^3 m_a'^1} + 6\overline{m_a'^2 m_a'^1}^2 + \overline{m_a'^1}^4.
\end{aligned} \tag{3.18}$$

In summary, by combining Eq. 3.12, 3.13 and 3.14 with Eq. 3.15 (for the $L\mathcal{N}$ case) or Eq. 3.16 (for the Exp case) or Eq. 3.17 and 3.18 (for the $T\mathcal{N}$ case), we compute analytically the first four moments of $P(I)$.

3.2.3 *Power spectrum of the synaptic current*

As we have derived in chapter 2 (Eq. 2.28) the power spectral density (PSD) of the current $I(t)$ is for non-zero frequencies

$$\mathrm{PSD}(f) = 2\nu(\mu_a^2 + \sigma_a^2)\frac{\tau_2^4}{(\tau_1+\tau_2)^2 + (2\pi f\tau_2)^2(2\tau_1^2 + 2\tau_1\tau_2 + \tau_2^2) + (2\pi f\tau_2)^4\tau_1^2}. \quad (3.19)$$

As expected, the PSD does depend only on the second cumulant of $P(a_k)$.

3.3 INFERENCE

Given the observed data, the inference problem is to estimate the parameters of the model: ν, μ_a, σ_a, τ_1 and τ_2.

We first present an idealised version of the model, which does not take into account variability and experimental conditions typical of *in vivo* recordings. In Sec. 3.3.3, we will describe the full version of the model.

3.3.1 *Ideal model*

In Fig. 3.4 we show the Bayesian network (see sec. 1.2.2) representing the dependencies among the variables (nodes) of interest: white nodes represent variables that have to be inferred from the data, while gray nodes stand for variables that are measured directly from the data.

The joint probability of the bayesian network in Fig. 3.4 has a complicated expression:

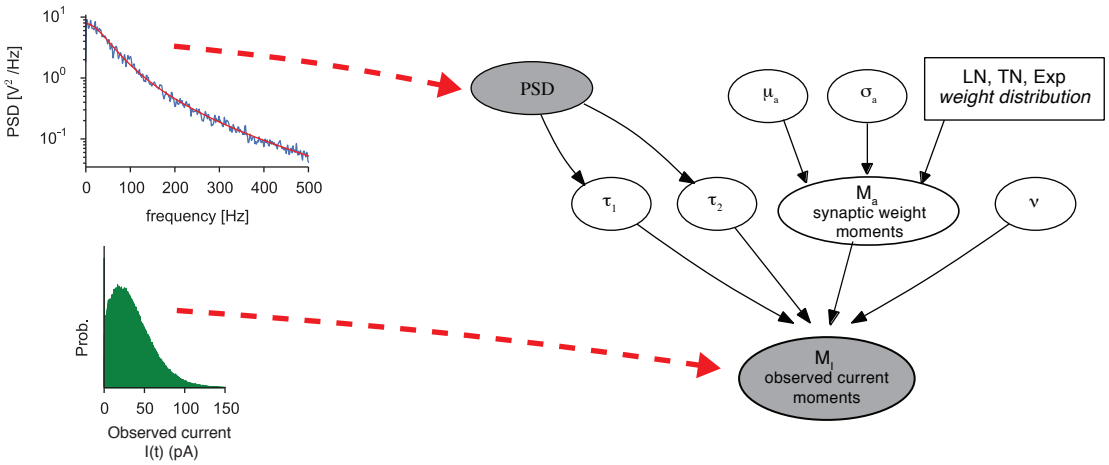

Figure 3.4: Bayesian network representing the dependencies between the variables. White nodes represent variables that have to be inferred from the data, gray nodes stand for variables that are measured directly from the data. The top left panel shows the PSD fit (red line is the fit with Eq. 3.19) and the bottom left panel is the probability distribution of $I(t)$, used to calculate the observed moments M_I. All variables are described in Table 3.1

Parameter name	Description
	Measured data D
M_I	Observed standardised central moments of the current $I(t)$
PSD	Power spectral density of $I(t)$
	Ideal model parameters θ_{th}
τ_1, τ_2	Rise and decay time of the EPSCs
DW	Distribution of the synaptic weights
$L\mathcal{N}$	Log-normal distribution (Eq. 3.8)
$T\mathcal{N}$	Truncated-normal distribution (Eq. 3.10)
Exp	Stretched exponential distribution (Eq. 3.9)
μ_a, σ_a	Mean and standard deviation of the weight distribution
M_a	Moments of the synaptic weight distribution
ν	Frequency of the synaptic inputs
	Additional full model parameters θ_{ex}
i_0	Voltage clamp baseline current
σ_H	Standard deviation contribution of voltage clamp high frequency noise
σ_L	Standard deviation contribution of the low frequency fluctuations of the synaptic input

Table 3.1: Description of the parameters and variables of the model.

$$\begin{aligned} P_{joint} =& P(\tau_1|\text{PSD}) \cdot P(\tau_2|\text{PSD}) \cdot P(M_a|\mu_a, \sigma_a, \text{DW}) \cdot \\ & P(\mu_a) \cdot P(\sigma_a) \cdot P(\nu) \cdot P(M_I|\tau_1, \tau_2, M_a, \nu) \end{aligned} \tag{3.20}$$

and the parameters, summarised in Table 3.1, will be discussed in the following sections. We first describe the data and the probabilistic dependencies among the nodes, and then how to perform the inference.

3.3.2 *Description of the nodes*

Unlike Kobayashi et al. (2011), Paninski et al. (2012), and Lankarany et al. (2013), which make the inference using the time course of the current (or voltage) trace,

we extract summary quantities from it. We measure its first four central standard moments $M_I = [\mu_I, \quad \sigma_I, \quad \text{skewness}_I, \quad \text{kurtosis}_I]$ and the PSD (see left hand side panels in Fig. 3.4).

Calculating the likelihood of a continuous function as the PSD is impractical, therefore we use empirical Bayes to set the prior on the time constants of the PSC (Casella, 1985). With a least square (LS) method we fit Eq. 3.19 to the PSD to find τ_1 and τ_2 (see top left panel in Fig. 3.4). Since we found the cross terms of the Hessian matrix between τ_1 and τ_2 to be very low (<0.005), we decided to model the time constants with independent Gaussian distributions with mean and variance given by the LS and the Hessian of the PSD fit. Although we are using the PSD data to set the prior on the time constants, we highlight that we are not double counting the data, because the PSD is not used as evidence in the inference process.

μ_a, σ_a and ν are given uninformative Uniform priors spanning a reasonable and positive range of values.

$P(M_a|\mu_a, \sigma_a, \text{DW})$ is a deterministic function, because the moments of the synaptic weight distribution M_a are fully determined given μ_a, σ_a and the weight distribution type (DW), see Eq. 3.15 (for the $L\mathcal{N}$ case), Eq. 3.16 (for the Exp case), Eq. 3.17 and 3.18 (for the $T\mathcal{N}$ case).

The likelihood of the moments of the current $P(M_I|\tau_1, \tau_2, M_a, \nu)$ cannot be calculated analytically, because Eq. 3.13 gives only the expected value of M_I, but not the uncertainties.

Thus, the likelihood can be estimated only by simulating multiple times the generative model with parameters τ_1, τ_2, M_a, ν. Due to the stochastic nature of the Poisson process, each run produces a different set of values of M_I and we estimate the likelihood with a 4-D kernel (see Fig. 3.5), because we consider the first four moments of the current distribution.

Notably, the likelihood does depend on the length of the simulation: longer runs give a narrower distribution but shorter intervals are preferable to allow the analysis of shorter periods in *in vivo* traces. As a compromise, we normally used 10 second long simulations, but in section 3.4.2 we compare the results for different trace lengths.

In the next section we generalise the model to take into account the effects of *in vivo* variability and experimental conditions.

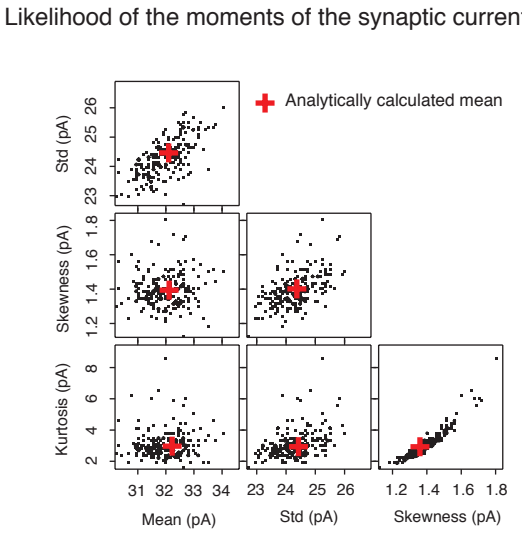

Figure 3.5: Likelihood of the moments of the synaptic current $P(M_I|\tau_1, \tau_2, M_a, \nu)$ estimated by simulating the generative model multiple times with fixed parameters τ_1, τ_2, M_a, ν. Red crosses represent the analytical predictions of the expected values of M_I, Eq. 3.13. (simulated data)

3.3.3 *Modelling in vivo variability and experimental conditions*

In vivo voltage clamp recordings show features that do not satisfy all the assumptions of the theoretical model described above, so we need to include additional parameters. Fig. 3.6 displays the bayesian network of the extended version of the model, adding three features to the simple version of Eq. 3.20. Now the joint probability is:

$$\begin{aligned} P_{joint} =& P(\tau_1|\text{PSD}) \cdot P(\tau_2|\text{PSD}) \cdot P(M_a|\mu_a, \sigma_a, \text{DW}) \cdot P(\mu_a) \cdot P(\sigma_a) \cdot P(\nu) \\ & \cdot P(i_0) \cdot P(\sigma_H) \cdot P(\sigma_L|\text{PSD}) \cdot P(M_I|\tau_1, \tau_2, M_a, \nu, i_0, \sigma_H, \sigma_L) \end{aligned} \tag{3.21}$$

where all the variables are summarised in Table 3.1.

The first additional feature is the baseline current (i_0) of the voltage clamp that has to be subtracted from $I(t)$. Experimenters usually estimate its contribution by finding an appropriate baseline to the voltage trace (green line in the left panel of Fig. 3.6).

Here, we set $P(i_0)$, the prior probability of i_0, to be normally distributed with mean and variance estimated with an informed guess, reflecting the uncertainty of the experimenter on the value of i_0. This is a step forward from the standard methods of measuring the total current, where the baseline is subtracted, although the uncertainty is not taken into account.

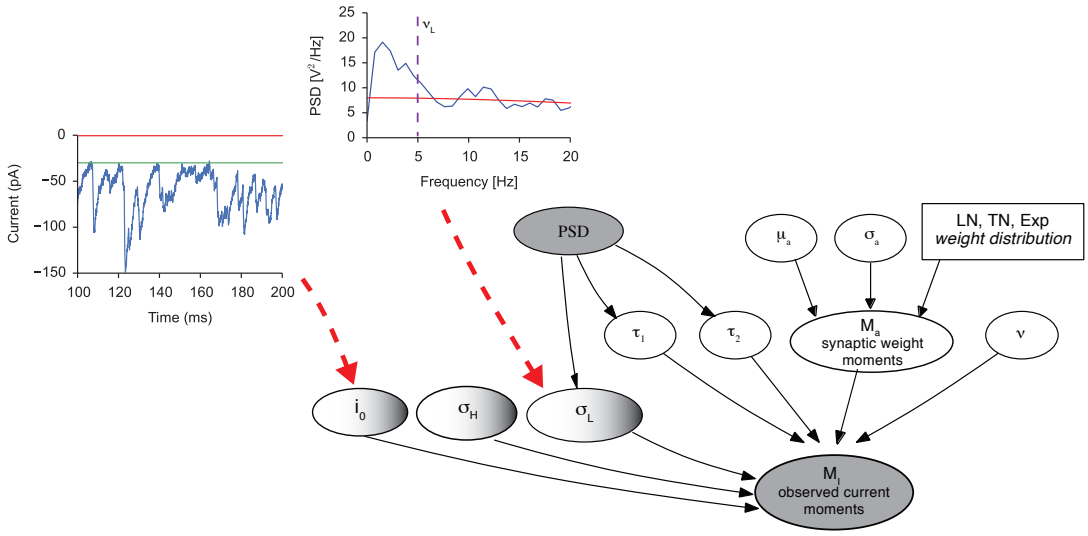

Figure 3.6: Bayesian network representing the dependencies between the variables of the full model. White nodes represent variables that have to be inferred from the data, gray nodes stand for variables that are measured directly from the data, and nodes with a gray transparency are variables taking into account variability and expreimental conditions of *in vivo* recordings. The left panel shows the estimated baseline (green line) of the current trace. The top panel displays the effect of low frequency fluctuation (below f_L) of the synaptic inputs on the PSD (red line is the fit of Eq. 3.19 excluding frequencies below f_L).

The second feature is the high frequency noise characteristic of the recording set-up and of the stochastic opening/closing of ion channels. Its standard deviation σ_H is measured experimentally and we model it as a zero mean Orstein-Uhlenbeck (OU) process

$$dU_{H_t} = -\tau_H U_{H_t} dt + \sigma_H \sqrt{2/\tau_H} dB_t, \tag{3.22}$$

where B_t is a Wiener process and the cut-off frequency is $1/(2\pi\tau_H) = 600$ Hz.

The third and last feature we take into account comes from the low frequency fluctuations which characterise *in vivo* synaptic activity. We relax the constant rate assumption by adding a modulation term modelled as an OU process with a cut-off frequency ($f_L = 1/(2\pi\tau_L)$) of 5 Hz

$$dU_{L_t} = -\tau_L U_{L_t} dt + \sigma_L \sqrt{2/\tau_L} dB_t. \tag{3.23}$$

We include this term in the PSD of $I(t)$:

$$PSD(f) = 2\Big(\nu + PSD_{OU}(f)\Big)(\mu_a^2 + \sigma_a^2) \times \frac{\tau_2^4}{(\tau_1+\tau_2)^2 + (2\pi f\tau_2)^2(2\tau_1^2 + 2\tau_1\tau_2 + \tau_2^2) + (2\pi f\tau_2)^4\tau_1^2}, \tag{3.24}$$

where the power spectrum of the OU process $PSD_{OU} = \sigma^2\tau_L/(1+(2\pi\tau_L)^2)$ does not affect the PSD above its cut-off frequency. To find its parameters, we fit the PSD with Eq. 3.19 in a range above f_L (red line in the top panel of Fig. 3.6) and calculate its integral σ_{th} (the theoretical standard deviation of a fluctuation free trace). Thus, we compute σ_{obs} (the integral of the observed PSD) and we calculate the variance (σ_L^2) of the OU process $\sigma_L^2 = \sigma_{obs}^2 - \sigma_{th}^2$ that explains the difference between the observed and theoretical standard deviation.

Due to the contribution of i_0, σ_H and σ_L, the likelihood of the observed moments of the current (M_I) is different from the one of the simple model.

To get the likelihood, we run multiple times the generative model adding the contribution of the *in vivo* features (i_0 and the two OU processes described above). As in the simple model case (section 3.3.2), we fit the data with a 4D kernel. We will validate the full model in section 3.4.4.

3.3.4 *Description of the sampling algorithm*

In principle, it is now possible to perform inference on the Bayesian network by sampling P_{joint}. This approach is very slow, because the likelihood does not have an analytical form and has to be estimated with multiple simulations after each MCMC sample[5].

Here we introduce a speed up trick that can be used when the likelihood is obtained by sampling from the generative model, but its means can be calculated analytically. The idea is to fit the likelihood with a kernel density estimation (KDE). If we assume that the shape of the likelihood does not depend much on the values of the parameters, the same KDE can be exploited to approximate the likelihood also for different parameter values. In practice, we keep the shape fixed, but we translate it to a new location determined by the analytically calculated average moments of the likelihood.

5 The estimation of the likelihood function takes about 1 minute on a standard desktop PC. In a typical MCMC run of $\sim$ 100000 samples, the calculation of the likelihood would take approximately 2 months.

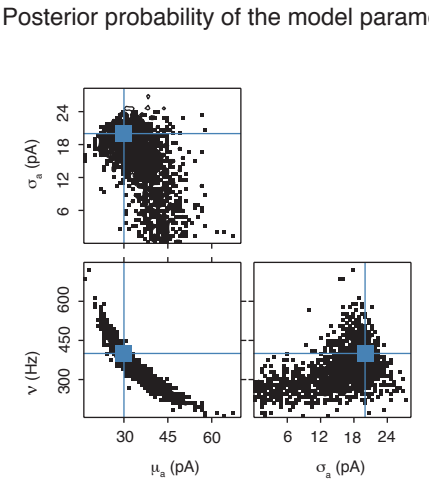

Figure 3.7: Posterior distribution of the main parameters of the model (μ_a, σ_a ν), obtained with MH MCMC sampling. $P(M_I|\tau_1, \tau_2, M_a, \nu)$. The blue lines represent the true values of the parameters (the values used to generate the data). The posterior distribution show us the dependencies among the parameters. The true values are in the regions of maximal probability, confirming that the algorithm gives correct results.

In our case, we initialise the parameters τ_1, τ_2, M_a, ν by LS fitting Eq. 3.13 to M_{obs} and Eq. 3.19 to the PSD. Thus, we run the generative model multiple times to calculate the shape of $P(M_I|\tau_1, \tau_2, M_a, \nu)$ with an exponential 4 dimensional KDE. Finally, we keep the shape fixed during the sampling of P_{joint}, but at each step we translate it to the location of the analytically calculated average moments (Eq. 3.12, red crosses in Fig 3.5). This trick makes the inference of the parameters computationally tractable.

We implemented the model in PyMC, a python package to perform Bayesian computation (Patil et al., 2010). We decided to use a simple Metropolis Hastings sampler, with normal proposal distribution and standard deviation equal to 1 over the absolute value of the parameter. Usually, the auto-correlation of the chains is about $300 - 500$ samples and the burn-in phase is about 10 effective samples. To construct the posterior, we generate ~ 400 effective samples and we assess the mixing by using the Geweke method provided by the PyMC package.

In Fig. 3.7 we simulated data and show the posterior distribution of the parameters contains the true values in the region of maximal density. We are also able to evaluate the dependencies between the parameters, because we do not have only a single point estimation (e.g. maximum *a posteriori*, MAP), but we recover the full posterior.

We checked whether our assumption on the fixed shape of the likelihood is correct. In Fig. 3.8 **a**, we plot the likelihood (with mean zero) at four different stages

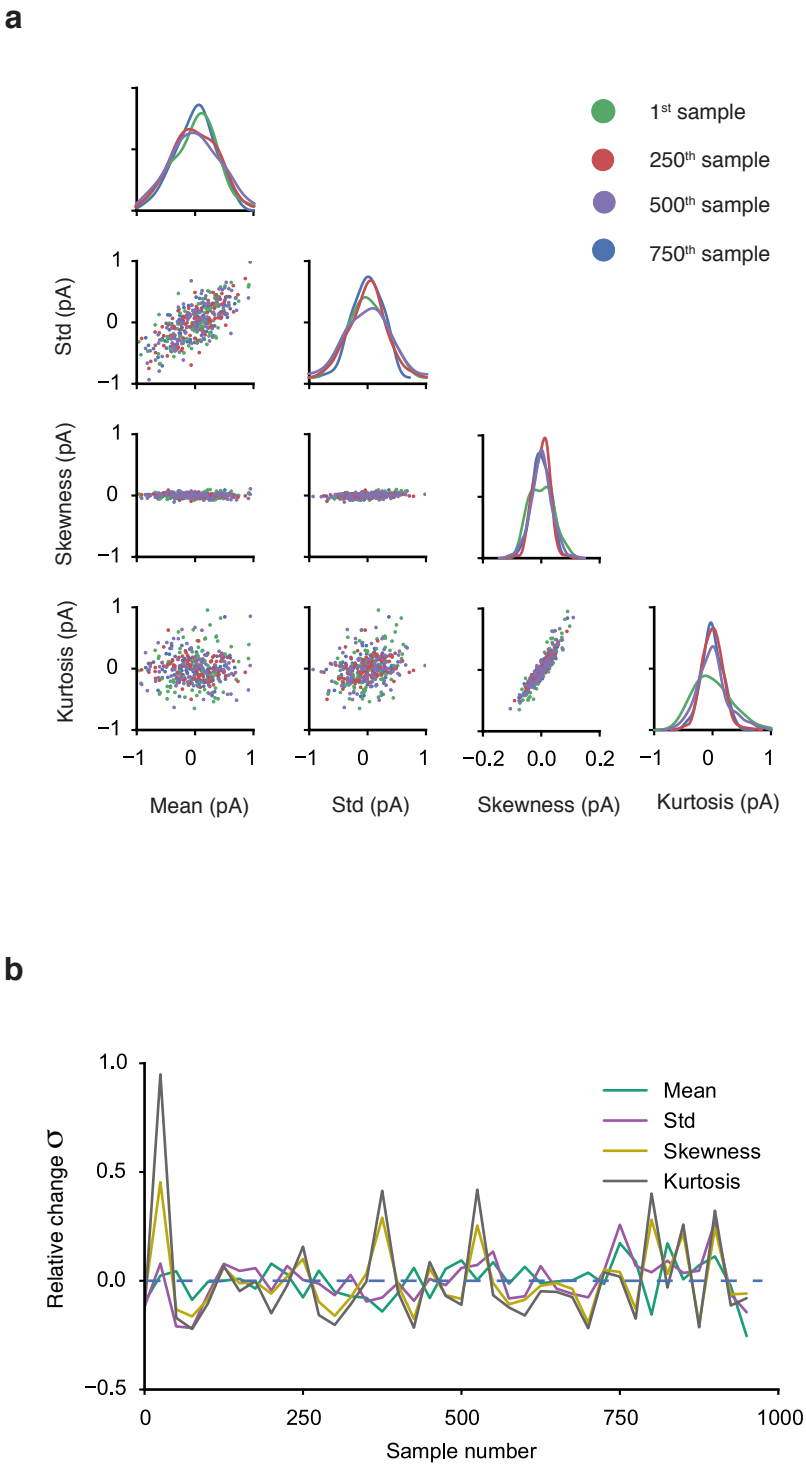

Figure 3.8: Testing the assumption of the speed up trick: shape of the likelihood during the MCMC run. **a)** Mean subtracted likelihood function $P(M_I|\tau_1, \tau_2, M_a, \nu)$ at four different stages of the MCMC run: after the 1^{st} (green), 250^{th} (red), 500^{th} (purple) and 750^{th} (blue) effective sample. **b)** Relative change $((x - \mu_x)/\mu_x)$ of the standard deviation of the likelihood functions during the MCMC run.

of the MCMC: 1^{st}, 250^{th}, 500^{th} and 750^{th} sample. All the probability functions of the likelihood are quite similar, although for skewness and kurtosis we notice some differences. In Fig. 3.8 **b**, we show the relative change $((x - \mu_x)/\mu_x)$ of the standard deviation of the likelihood functions (basically the width of the KDEs of panel **a**) during the MCMC run. The shapes of the likelihoods of the mean and of the standard deviation of the current are quite constant during the sampling (at most $\sim 20\%$ change). However, the shapes of the likelihood of skewness and kurtosis seem to vary more, with changes up to $\sim 50\%$.

This analysis shows that the assumptions we made are not completely satisfied, which means that the shape of the posterior distributions might not reflect the true uncertainty of the parameters. However, in sec. 3.4 we show that this approximation gives correct results for a wide range of biologically plausible parameters.

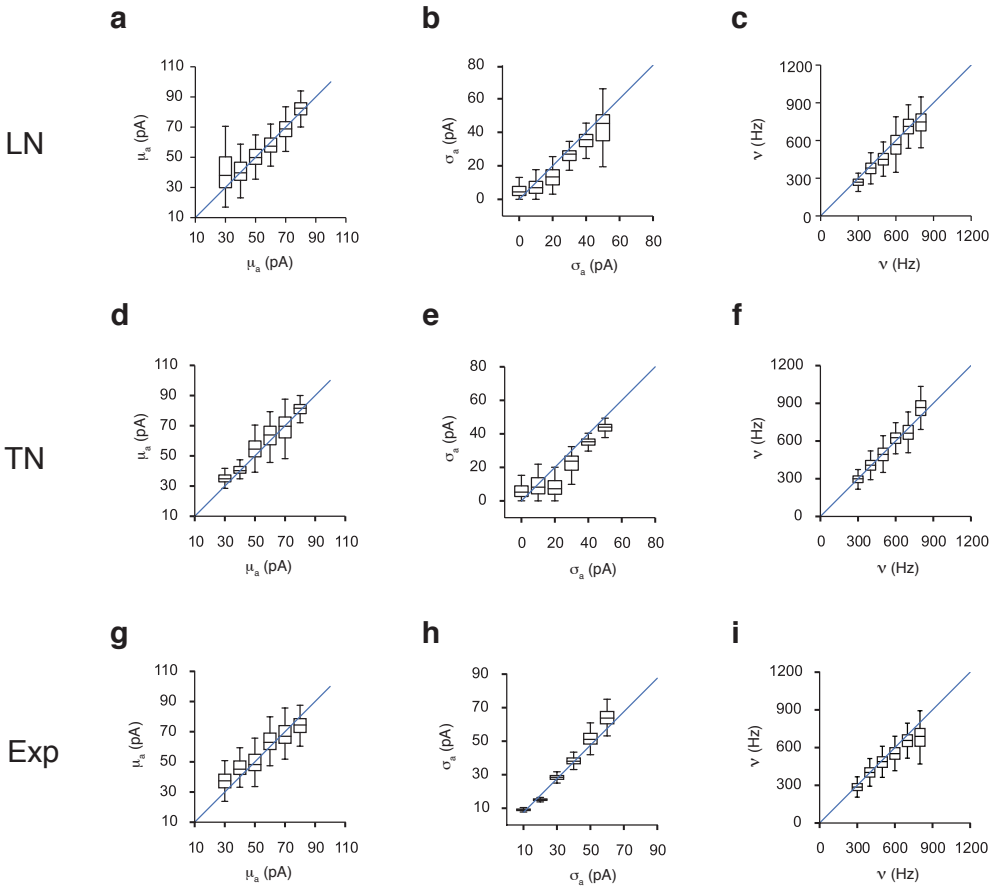

Figure 3.9: The inference generate good approximations of synaptic parameters when examined over a physiological range, when the true distribution of synaptic weights is known *a priori*. In **a)**, **b)** and **c)** we use a $\mathcal{LN}$ synaptic weight distribution and vary μ_a, σ_a and ν respectively. The posterior distributions of the parameters are plotted against the true value (blue line). **d-f)** and **g-i)** are the same as in **a-c)**, but using $\mathcal{TN}$ and Exp weight distributions respectively. The boxes represent the 33^{rd} and 66^{th} percentile of the distributions, while the whiskers represent the full range.

3.4 RESULTS - MODEL VALIDATION

3.4.1 *Inferring the parameters with the correct synaptic weight distribution*

We generate 10s traces using the model of section 3.2 with known parameters and we apply our inference method to recover the value of the parameters. For now, we assume that we know *a priori* the correct distribution of the synaptic weight ($\mathcal{LN}$, $\mathcal{TN}$ or Exp). In section 3.4.3 we will relax this assumption.

The standard parameters are: $\mu_a = 50$ pA, $\sigma_a = 30$ pA, $\nu = 700$ Hz, and one parameter per time is varied while keeping the others fixed. In Fig 3.9 we show the

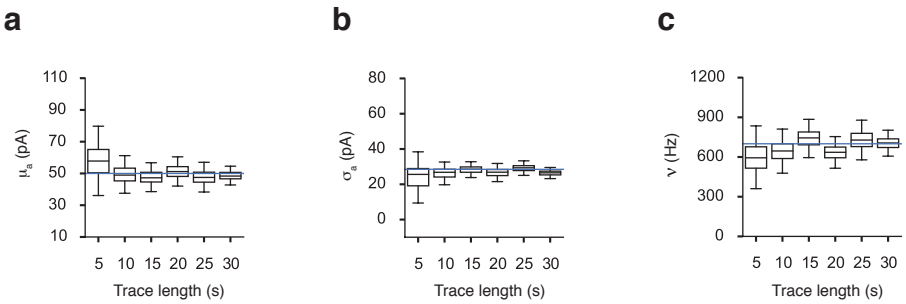

Figure 3.10: Parameter inference for a range of simulation lengths, using $L\mathcal{N}$ weight distribution. **a-c**, represent respectively μ_a, σ_a and ν.

posterior distribution of the parameters vs. their true value. Our inference works well in a physiologically plausible range and the true value is almost always within the confidence interval.

3.4.2 *Impact of the recording length on the inference*

As mentioned in Sec. 3.3.2, the likelihood function depends on the length of the trace. Intuitively, longer traces lead to less uncertainty, because more statistics are collected. However, short intervals would be preferable, because they allow the analysis of shorter periods in *in vivo* traces. This is important because it would make possible to track rapid changes in input structure that would be otherwise lost while averaging over a longer period.

In Fig 3.10, we test the performance of our algorithm with varying trace lengths. As expected, longer traces lead to less uncertainty on the parameters. The analysis shows that 10 second long recordings are in general enough to obtain a reasonable estimation of the parameters.

3.4.3 *Model selection*

Next, we tested whether we are able to determine the correct weight distribution when we do not know it *a priori*. As discussed in section 1.2.4, the Bayesian framework offers straightforward tools to assess the likelihood of a model, such as the Deviance Information Criterion (DIC). The higher is the DIC, the less likely the model suitably describes the data.

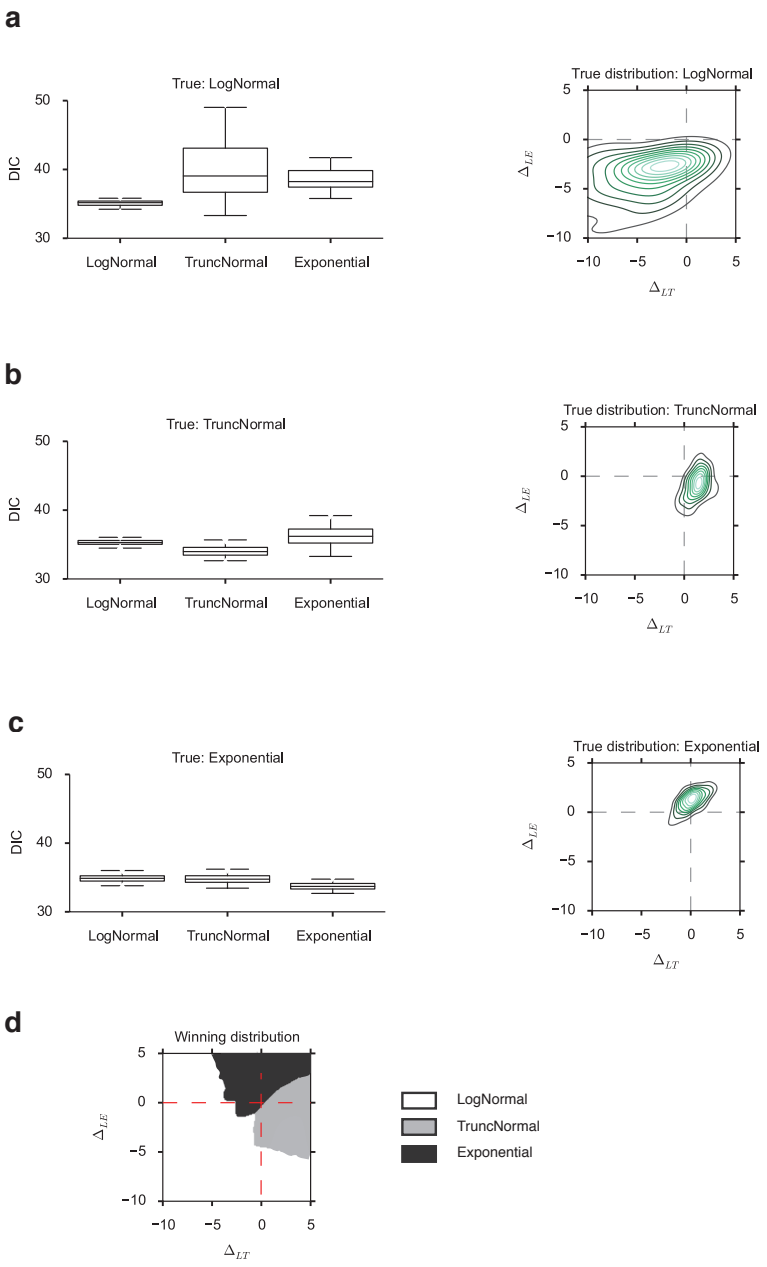

Figure 3.11: **a-c)** Distribution of the DIC value of a model assuming $L\mathcal{N}$, $T\mathcal{N}$ and Exp weight distributions when the true distribution is $L\mathcal{N}$ (**a**), $T\mathcal{N}$ (**b**) and Exp (**c**). On the right side, joint probability distributions of Δ_{LE} and Δ_{LT}. **d)** Most probable weight distribution in the region of space $(\Delta_{LE}, \Delta_{LT})$: white is $L\mathcal{N}$, gray is $T\mathcal{N}$ and black is Exp.

		True		
		$L\mathcal{N}$	$T\mathcal{N}$	Exp
Chosen	$L\mathcal{N}$	0.85	0.02	0.00
	$T\mathcal{N}$	0.13	0.91	0.04
	Exp	0.02	0.07	0.96

Table 3.2: Probability of selecting a certain weight distribution, given the true weight distribution. Values on the diagonal represent correct classifications.

Here, we generated 100 traces using the same weight distribution (true distribution: either $L\mathcal{N}$, or $T\mathcal{N}$, or Exp). For each of the three true weight distributions, we run the inference algorithm assuming either $L\mathcal{N}$, or $T\mathcal{N}$ or Exp weight distribution and we calculate the DIC for each model. In Fig. 3.11 **a-c** (left hand side) we display the distribution of the DIC values under the different conditions. Notably, the models with the correct weight distribution tend to have smaller DIC values than the other two.

In model comparison tasks, what matters is the difference between the DIC values. Thus, from the three DIC values of the three models (DIC_L, DIC_T and DIC_E, corresponding to the $L\mathcal{N}$, $T\mathcal{N}$ and Exp model respectively) we calculate two quantities: $\Delta_{LT} = \mathrm{DIC}_L - \mathrm{DIC}_T$, and $\Delta_{LE} = \mathrm{DIC}_L - \mathrm{DIC}_E$. In the right hand side of Fig. 3.11 **a-c**, we display $P(\Delta_{LE}, \Delta_{LT}|X)$, the joint probability distributions of Δ_{LE} and Δ_{LT} for the three different true distributions $X = [L\mathcal{N}, T\mathcal{N}, Exp]$.

To find the most likely weight distribution, we apply Bayes theorem and calculate

$$\begin{aligned} P(X|\Delta_{LE}, \Delta_{LT}) &= \frac{P(\Delta_{LE}, \Delta_{LT}|X)P(X)}{\Sigma_{Y\in[L\mathcal{N}, T\mathcal{N}, Exp]}P(\Delta_{LE}, \Delta_{LT}|Y)P(Y)}, \\ &= \frac{P(\Delta_{LE}, \Delta_{LT}|X)}{\Sigma_{Y\in[L\mathcal{N}, T\mathcal{N}, Exp]}P(\Delta_{LE}, \Delta_{LT}|Y)}, \end{aligned} \tag{3.25}$$

where in the second line we assumed that the three weight distribution are equiprobable *a priori*. Thus, for each point in the space $(\Delta_{LE}, \Delta_{LT})$, the winning distribution is the one which has the highest probability according to Eq. 3.25 (see Fig. 3.11 **d**). By applying this method, we are able to correctly choose the weight distribution $\sim 90\%$ of the time, as summarised in Table 3.2

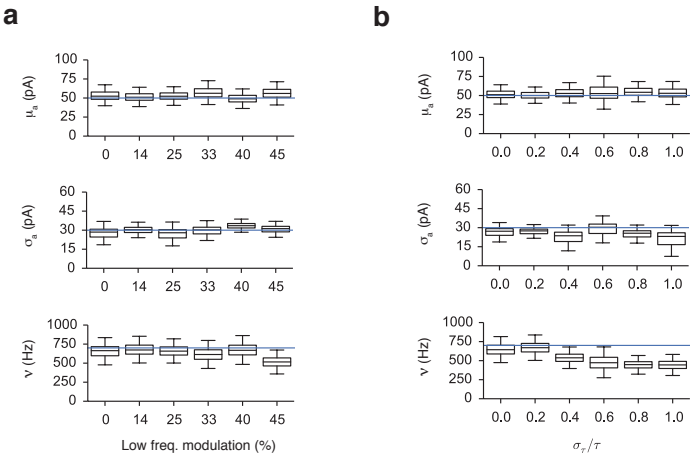

Figure 3.12: Inference is robust to *in vivo* variability. **a)** We add an inhomogeneous low frequency (< 5 Hz) component to the Poisson rate. The parameters' estimation is plotted against the contribution (in percentage) of the low frequency modulation to the total standard deviation. **b)** Same as in **a)**, but progressively increasing the standard deviation of the rise- and decay-time constants.

3.4.4 *Adding sources of in vivo variability*

In the previous sections we have demonstrated that our model performs well in the simple case, when the ideal model (sec. 3.3.2) correctly describes the generative process. However, we need to test what happens when we introduce variability typical of *in vivo* recordings and we make use of the full model described in Sec. 3.3.3.

Firstly, *in vivo* activity breaks the stationary assumption of the homogeneous Poisson model and inputs typically show fluctuations on a slow time scale. To test the model robustness, we generate *in vivo*-like traces by adding an inhomogeneous component to the Poisson rate, modelled as a OU process with 5 Hz cut-off frequency (Fig. 3.12 **a**). Again using simulated data, we demonstrate that the full model performs well even in presence of considerable fluctuations in the synaptic input rate.

Secondly, *in vivo* PSCs rise- and decay-times vary as different synapses may have different kinetic proprieties and dendritic filtering severely affects the shape of the PSCs measured at the soma (Williams and Mitchell, 2008). To test whether our model performs well when the shape of the PSCs varies, we generate voltage clamp traces where for each PSC the two time constants are drawn from truncated normal distribution $T\mathcal{N}(\tau_1, \sigma_1)$ and $T\mathcal{N}(\tau_2, \sigma_2)$. Our model correctly predicts μ_a and σ_a even for large variances of τ (Fig. 3.12 **b**). However, when the standard deviation is larger than half the average τ (in practice $\sim$ 1ms) the model underestimates the frequency of the inputs.

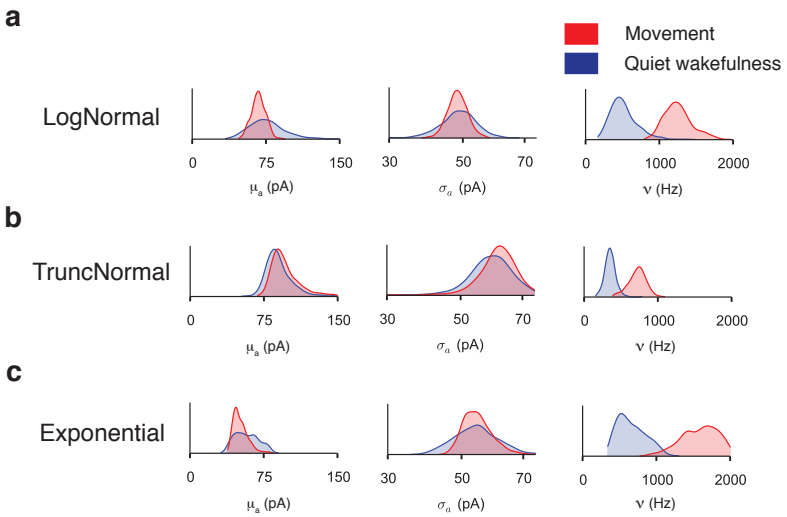

Figure 3.13: Posterior distribution of the mean amplitude (left), standard deviation (center) and frequency (right) of the synaptic inputs during quiet wakefulness and movement of a representative recording. In **a)**, **b)** and **c)** we assumed a $L\mathcal{N}$, $T\mathcal{N}$ and Exp synaptic weight distribution respectively.

3.5 RESULTS - INFERENCE OF *in vivo* DATA

In the previous sections we validated our model, showing that it is able to correctly infer the parameters of the generative model even in presence of sources of variability typical of *in vivo* recordings. Here we apply our inference method to recordings from molecular layer cerebellar interneurons of mice during quiet wakefulness and self-paced voluntary movement. Animals were head restrained and mounted on a single-axis cylindrical treadmill (Fig. 3.1 **a**). Once the patch-clamp whole-cell configuration was obtained, the cell membrane potential was clamped at -70 mV.

3.5.1 *Higher frequency of synaptic inputs increases excitatory current*

All the traces we analysed ($n = 8$) were 90 second long and contained at least 20 seconds of movement. We applied to each trace our inference method three times, using $L\mathcal{N}$, $T\mathcal{N}$ and Exp distribution.

The synaptic time constant we found by fitting the power spectrum of the current with Eq. 3.19 were consistent with those found in literature (Szapiro and Barbour, 2007): $\tau_1 = 0.25 \pm 0.04$ ms and $\tau_1 = 1.56 \pm 0.21$ ms (mean $\pm$ standard error).

In Fig. 3.13 we show the posterior distribution of μ_a, σ_a and ν during quiet wakefulness and movement for a representative trace. Qualitatively, the results do not

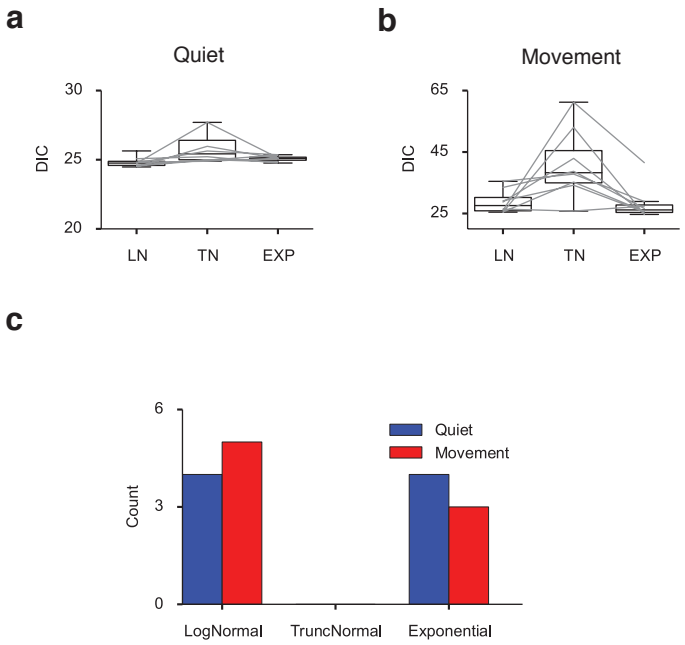

Figure 3.14: Determining the most likely synaptic weight distribution *in vivo*. **a,b)** Distribution of the DIC values for the three models ($L\mathcal{N}$, $T\mathcal{N}$ and Exp) during quiet wakefulness and movement respectively. **c)** Model-inferred synaptic weight distribution during quiet wakefulness (Blue) and movement (red).

depend on the chosen weight distribution: during movement the frequency of the inputs increases, while the parameters of the synaptic weight distribution do not change significantly. However, when using the $T\mathcal{N}$ distribution, the frequency of inputs is lower and the standard deviation of the weights higher than when using the $L\mathcal{N}$ or Exp.

By using the method described in section 3.4.3, we determined which synaptic weight distribution is the most likely *in vivo*. Interestingly, the $T\mathcal{N}$ distribution was the least favoured distribution both during quiet wakefulness and movement (Fig. 3.14 **a** and **b**). Our model selection always indicated either the $L\mathcal{N}$ or the Exp as the most likely distribution (Fig. 3.14 **c**).

We also measured the exponent of the Exp distribution (Eq. 3.9) and found that on average it was 0.8 (range $0.7 - 1.2$). Thus, our findings suggest that molecular layer interneurons in the cerebellum have a long-tailed synaptic weight distribution. This means that in general synapses are small, but a few of them are very large (Song et al., 2005a).

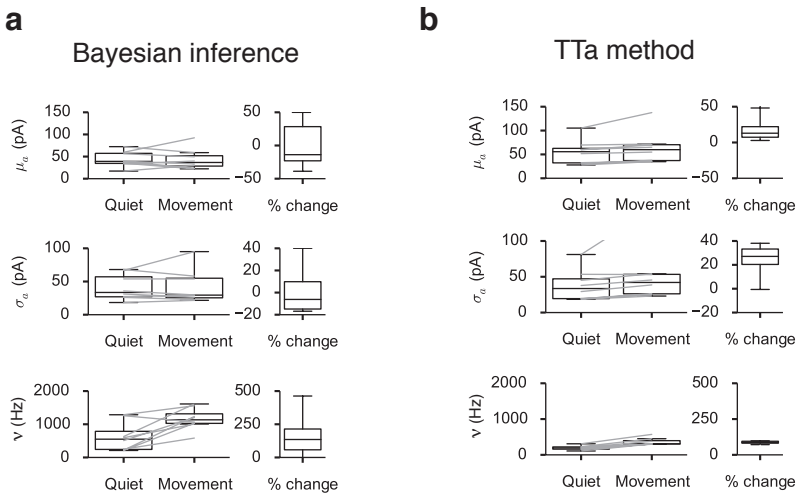

Figure 3.15: Comparison of the parameters obtained analysing n=8 *in vivo* voltage clamp recordings with our inference **(a)** and with the *TTa* method **(b)**.

Finally, in Fig. 3.15 we compare the estimation of μ_a, σ_a and ν performed with our model and with the *TTa* method. Our inference method suggests that on average, the increase in excitatory synaptic current is produced by higher frequency inputs without changing the amplitude or standard deviation of the synaptic weights (Fig. 3.15 **a**). In particular, during movement the input frequency roughly doubles, from $\sim$ 600 to $\sim$ 1200 Hz. On the other hand, as explained already in section 3.1.3, with the *TTa* method it is difficult to count more than 500 input per second. As expected, the frequency of the synaptic inputs is underestimated by a factor of two. Moreover, unlike our method, μ_a and σ_a are predicted to show small increases during movement. This is because overlapping events are more likely to happen and thus misclassified as a single PSC.

3.6 CONCLUSION

3.6.1 *Summary of the findings*

In this chapter, we proposed a novel probabilistic model to infer synaptic input statistics using *in vivo* voltage-clamp data.

We first showed that inference is correct (i) when the distribution of synaptic weights is known, (ii) when the trace shows slow fluctuations of synaptic inputs and (iii) when the time constants of the PSCs are heterogeneous. Thus, we demonstrated that we are able to estimate, with about 90% success, the correct distribution of synaptic inputs. Finally, we applied this method to voltage-clamp recordings from molecular layer cerebellar interneurons of awake mice. There are two main findings: (i) the response size distribution has a long tail and on average does not change during movement, (ii) the increase in excitatory current during movement is due to an increase in the frequency of all synaptic inputs.

The distribution of synaptic weights is a hot topic in current research because it has important effects on memory storage (Teramae and Fukai, 2014; Barbour et al., 2007), on cortical firing rates (Koulakov et al., 2009; Roxin et al., 2011) and information transmission (Teramae et al., 2012; Buzsáki and Mizuseki, 2014). Evidence from *in vitro* studies shows that EPSPs have a skewed long-tailed distribution in various regions of the brain (Sayer et al., 1990; Manabe et al., 1992; Song et al., 2005a; Ikegaya et al., 2013). In practice, most of the synapses have small EPSPs and contribute to the background activity of the membrane potential. However, a few strong synapses evoke large EPSPs which have a high probability of generating a spike and thus propagating information to downstream neurons.

Unfortunately, directly measuring the distribution of synaptic weights in behaving animals is practically impossible due to the high input frequency (Buzsáki and Mizuseki, 2014). Our method represents a step forward, because we demonstrate that we can capture the effective distribution of synaptic inputs from *in vivo* voltage-clamp recordings.

We highlight that typically the techniques used to determine synaptic weight distributions *in vitro* and *in vivo* are different (see section 3.1.4). In our *in vivo* inference, the contribution of each synapse is weighted by its own input rate: synapses receiving more inputs contribute more to the weight distribution. In practice, we measure an *effective* weight distribution. This is why our inference would detect an increase in the input rate of stronger synapses also as a shift in the mean and standard deviation of the amplitude.

Interestingly, we showed that the increase in excitatory current during movement is due to higher frequency of inputs, while on average the synaptic weight distribution does not change. This scenario is consistent with the hypothesis summarised in Fig. 3.1 **c**: interneurons receive a global and uniform increase in their excitatory inputs during movement. Molecular layer interneurons in cerebellum receive their inputs from granule cells (GCs), which represent the input layer of the cerebellar circuit (Dean et al., 2010). GCs have naturally a very low firing rate ($\sim$ 1Hz) but show a characteristic bursting behaviour during sensory stimulation (Beugen et al., 2013). Our findings have an impact on how information flows to interneurons: we argue that both the signal coming from the large synapses and the background activity increase during movement and that short term plasticity does not have a detectable effect on the synaptic amplitudes.

3.6.2 *Assumptions of the model and future work*

One of the main assumptions is that synaptic inputs are uncorrelated and follow a Poisson distribution. Experimental measurements of correlations in the brain are contradictory and largely depend on what time-scale is considered (Cohen and Kohn, 2011). Notably, correlations on a longer time scale would be visible in the PSD, adding a component with a different time-constant (Moreno-Bote et al., 2008). When fitting the PSD of *in vivo* data, indeed we observed a bump in activity at low frequencies ($f < 10$ Hz), that could correspond to spike correlations on time-scales $\geq$ 15ms[6], but we take into account this effect as explained in Sec. 3.3.3. Unfortunately, we would not be able to identify spike-correlations on the order of τ_1 and τ_2, because they would contribute to the PSD in the same frequency range. However, it is generally accepted that spike count correlations on a short time scale ($\sim 1-5$ms) are small, normally < 0.03 (Smith and Kohn, 2008; Helias et al., 2014; Grytskyy et al., 2013; Renart et al., 2010; Ecker et al., 2010), and thus our inference would likely still give reasonable results, as shown by the following simple calculation.

Let's take a neuron that receives identical inputs with equal amplitude a and a global frequency ν. If the inputs have a correlation c, it means that the probability of two inputs to be coincident is c. If we take a reasonable value of $c = 0.05$, it means that every 100 inputs, we actually will observe on average only 95 inputs (5 are coincident), 90 of which of size a and 5 of size $2a$. Generalising from the above example, for a given correlation c, the observed frequency is $\nu_{\text{obs}} = \nu_{\text{true}}(1-c)$ and the observed average amplitude $a_{\text{obs}} = a_{\text{true}}(1-c)$, where the subscript $_{\text{obs}}$ refers

6 the cut-off frequency is $f \sim 1/(2\pi 15\text{ms})$

to the observed values. Thus, even assuming $c = 0.05$, the error of our estimation wouldn't be worse than 5%, which we consider a reasonable result.

However, it would be an important avenue of future work to run simulations with input trains with a different level of correlation and assess the impact on the inference model.

Secondly, we need *in vivo* traces to be stationary over a period long enough to accumulate sufficient statistics. This is possible when the inputs are stable and the cerebellar interneurons used in this study are an excellent example, whilst in other areas or cell types this might not be the case.

As discussed in section 3.1.5, recent techniques based on Kalman filtering (Kobayashi et al., 2011; Paninski et al., 2012; Lankarany et al., 2013) give a good estimation of the time-varying synaptic conductance, but do not allow an independent estimation of the rate and amplitude distribution of the individual synaptic inputs. The solution is to use the method we proposed here to shape an informed prior on the probability distribution of the synaptic weights to feed the Kalman-filtering based models.

In this study we restricted the analysis of *in vivo* voltage clamp recordings at the reversal potential of inhibition to measure only excitatory inputs. It would be interesting to analyse traces recorded in the same cells at the reversal potential of excitation to infer the statistics of the inhibitory inputs. In the current clamp configuration, we record the membrane potential of the neuron, which, in the ohmic approximation, is the result of the combined effect of excitatory and inhibitory currents. If we infer the statistics of excitation and inhibition individually via voltage-clamp as described above, it will be interesting to extend the model to include the effect of correlations between excitation and inhibition in a current clamp trace.

In summary, we showed that present methods used to analyse *in vivo* voltage clamp data fail to infer quantitatively and qualitatively the statistics of the inputs. Our model represents an important step forward in our ability to extract all possible information from high-resolution *in vivo* intracellular recordings.

4

SUBTHRESHOLD DYNAMICS UNDERLYING BEHAVIORAL STATE-DEPENDENT BIDIRECTIONAL MODULATION OF MOTOR CORTEX OUTPUT

Part of this chapter is a product of the collaboration with other members of Duguid Lab (University of Edinburgh) that resulted in a publication which I co-first authored: ***Cellular Mechanisms Underlying Behavioral State-Dependent Bidirectional Modulation of Motor Cortex Output****, Julia Schiemann, Paolo Puggioni et al., Cell Reports 11, (2015).*

All the data collection and analysis presented here are a result of my work, with some exceptions listed below. L5B recordings: performed by Paolo Puggioni (PP), with a substantial contribution from Julia Schiemann (JS) and some additional help from Joshua Dacre (JD). Projection target identification: JS, with the help from PP and JD. Morphological reconstructions of pyramidal neurons: Ian Duguid, with the contribution of PP, JS and JD. Implementation of the simulated power-spectrum fit PP with the help of Miha Pelko. In the data figure captions, I highlight the contribution of other lab members.

4.1 INTRODUCTION

4.1.1 *Modulation of motor cortex activity during behaviour*

Primary motor cortex (M1) plays a central role in regulating complex motor behaviors (Graziano and Aflalo, 2007b,a; Lemon, 2008, 2010). For decades scientists have focused on investigating how patterns of motor cortex output relate to different aspects of volitional, goal-directed movement and ongoing locomotor rhythm.

Neuronal activity in M1 correlates with rhythmic voluntary motor movements (Phillips and Porter, 1977; Armstrong and Drew, 1984; Drew et al., 2002, 2004; Isomura et al., 2009). During walking or running output neurons in M1 display changes in firing rates that reflect periods of coordinated muscle activity (Armstrong and Drew, 1984; Beloozerova et al., 2003; Phillips and Porter, 1977). Although spontaneous locomotor activity is generated by central pattern generators (CPGs) in the spinal cord (Forssberg and Grillner, 1973; Goulding, 2009), descending motor commands from M1 are integrated with ongoing rhythmic spinal cord signals and sensory afferent input from the periphery to initiate, adjust and maintain locomotor

function (Armstrong and Drew, 1984; Beloozerova et al., 2003; Ueno and Yamashita, 2011). In particular, a subset of layer 5B (L5B) pyramidal neurons project to the pyramidal tract (PT) which directly targets spinal circuits (Shepherd, 2013). In rodents, L5B neurons display enhanced or suppressed (e.g. bidirectional) firing rate changes during locomotion that are abrupt, sustained changes – so called "on-off" responses – or gradual frequency changes linked to the velocity of running (Costa et al., 2004). Although we are now beginning to understand how patterns of motor cortex activity relate to changes in behavioral state (quiet wakefulness vs. movement), the cellular mechanisms underpinning bidirectional modulation of M1 output during self-paced voluntary movement in rodents remain largely unresolved. Likely candidates are: (i) changes in conductance state, (ii) changes in cortical state-dependent network-driven input structure, and (iii) altered excitatory inputs coming from other cortical or subcortical areas.

Previous reports have shown that neurons in the awake brain display a much lower input resistance with respect to *in vitro*, due to the elevated synaptic activity - see section 2.1.2 and (Destexhe et al., 2003). Possibly, during behaviour, rapid changes in conductance modulated by synaptic activity might alter M1 neuron responsiveness (Shu et al., 2003; Haider and McCormick, 2009; Destexhe and Contreras, 2006).

During inactivity or slow-wave sleep cortical networks remain in a synchronised state that consists of slow, large amplitude oscillations that characterise the activity of neuronal populations (Steriade et al., 1993b; Cowan and Wilson, 1994; Steriade et al., 2001; Petersen et al., 2003; Poulet and Petersen, 2008). During changes in behavioral state, cortical networks become desynchronised displaying a reduction in slow oscillations and in some cases an increase in higher frequency activity (Steriade et al., 1993b). This change in network-driven input structure profoundly alters the subthreshold V_m dynamics and spike output patterns of cortical pyramidal neurons during behavior - see section 1.1.4 and (Castro-Alamancos, 2004a; Constantinople and Bruno, 2011; Crochet and Petersen, 2006; Haider et al., 2012; Okun and Lampl, 2008).

It also likely that neural activity in the output layer of M1 is modulated by inputs coming from a variety of brain areas (e.g. L2/3 neurons in M1, secondary motor cortex and motor thalamus - see section 1.1.2 and Fig. 1.2). Possibly, these inputs could modulate the dynamics of L5B neurons during behaviour.

In this study we investigated which combination of the three mechanisms (conductance changes, network state and excitatory inputs) is responsible for the bidirectional modulation of M1 output neurons during self-paced voluntary movement.

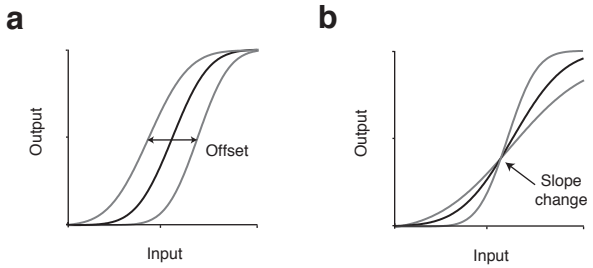

Figure 4.1: Changes in the input-output curve: **a)** offset and **b)** slope.

4.1.2 *Cellular mechanisms that regulate input sensitivity*

The cellular mechanisms that regulate the flow of information and input-output transformations in M1 during self-paced voluntary movement remain largely unresolved.

The input-output curve is a simple measure of the magnitude of the response of a neuron as a function of the input amplitude (see Fig 4.1). In principle, changes in membrane potential (V_m) mean (μ_{V_m}) or standard deviation (σ_{V_m}) and effective input resistance (R_{eff}) can have profound effects on the response magnitude (or sensitivity) of a neuron to its synaptic inputs (Hô and Destexhe, 2000; Chance et al., 2002; Tiesinga et al., 2004; Cardin et al., 2008) - see section 1.1.5 for a discussion on the terminology used in this chapter.

Neurons in the neocortex receive continuous barrages of synaptic input *in vivo*, which strongly influence their integrative properties and output firing patterns (Haider and McCormick, 2009; Shu et al., 2003). Given that brain-state profoundly alters the spatiotemporal structure of synaptic input to cortical neurons *in vivo*, can rapid changes in subthreshold V_m dynamics account for neuronal response modulation during behavior? This question has been explored in a variety of computational and experimental studies that have identified several mechanisms by which neuronal responsiveness can be dynamically modulated.

In the absence of significant membrane potential variability, steady-state changes in V_m result in altered neuronal responsiveness by shifting the input-output curve along the input axis (Fig. 4.1 **a**) (Hô and Destexhe, 2000; Chance et al., 2002; Silver, 2010). However, if the input range is restricted to the initial portion of the input-output curve, shifts along the driving axis can produce non-linear changes that profoundly alter the sensitivity to small amplitude inputs (Brozović et al., 2008; Silver, 2010). In contrast, changes in synaptically-driven membrane potential variance or 'noise' provides a variable level of depolarization that reduces the slope of neuronal input-output transformations increasing the probability that small inputs reach threshold,

while reducing responses to larger amplitude inputs (Fig. 4.1 **b**) (Chance et al., 2002; Hô and Destexhe, 2000; Silver, 2010). Changes in membrane conductance directly lead to amplitude changes of the EPSPs (the voltage deflection is proportional to the synaptic current divided by the membrane conductance). Thus, increasing the membrane conductance results in leftward shifts of the input-output curve and vice-versa (same schematic as in Fig. 4.1 **a**).

By combining changes in membrane potential mean, variance and membrane conductance, cortical neurons can dynamically alter the shape of input-output transformations depending on the nature and context of a specific behavior.

Recent evidence has shown that behavioral state-dependent changes in V_m dynamics can profoundly affect the integrative mode and response gain of neocortical pyramidal neurons. In rodents, locomotion increases the gain and signal-to-noise of visually evoked responses in V1 L2/3 principal cells (Niell and Stryker, 2010; Keller et al., 2012; Bennett et al., 2013; Polack et al., 2013) via two independent mechanisms: (i) a decrease in V_m variability which reduces spontaneous firing and (ii) an increase in average V_m which enhances subthrehold responses. This state-dependent modulation of visually-evoked responses appears to require the interplay between cholinergic disinhibition (Fu et al., 2014), enhanced glutamatergic input and noradrenergic neuromodulation (Polack et al., 2013). Although there is now emerging evidence of the subthreshold dynamics underlying brain state-dependent gain modulation in superficial cortical layers, how behavior-related changes in Vm dynamics affect input-output transformations in L5B projection neurons of M1 has never been explored.

4.2 METHODS

To investigate the cellular mechanisms underpinning behavioral state-dependent modulation of motor cortex output, we combined *in vivo* patch-clamp recordings, neuroanatomical tracing and computational modeling.

4.2.1 *Animals and surgery*

All experiments and procedures involving animals were approved by the University of Edinburgh local ethical review committee and performed under license from the UK Home Office in accordance with the Animal (Scientific Procedures) Act 1986. Male 5-8 weeks old, C57BL/6 mice (20-25 g), 2-6 animals per cage, maintained on a reversed 12:12 hour light:dark cycle and *ad libitum* access to food and water were implanted with a small lightweight headplate (0.75 g) under 1.5 % isoflurane anaesthesia using cyano-acrylate glue and dental acrylic. After at least 2 days recovery, a craniotomy (300 $\times$ 300 μm) was performed above the right forelimb region of M1 (identified by intracortical microstimula- tion) and the dura removed. The craniotomy was sealed with (1.5 %) agar and Kwik-Cast sealant (WPI, Europe) and mice were returned to the home cage to recover for $\sim$2 hrs before recording commenced.

4.2.2 *Cortical mapping*

To find the coordinates of the forelimb region of primary motor cortex ($M1_{FL}$), we mapped the area using intracortical microstimulation (ICMS) (Dombeck et al., 2009; Tennant et al., 2011) in 7 male mice under 0.5% isoflurane anesthesia. Glass micropipettes (1-2 MΩ) filled with extracellular solution were targeted to layer 5 ($600 - 800\,\mu$m) and cathodal pulse trains (50 ms train duration, $30 - 350\,\mu$A, 300 μs pulse duration, 33 Hz) (A.M.P.I. Iso-flex) were applied through the stimulating electrode and slowly increased until contralateral forelimb muscle twitches could be observed. Stimulation sites were spaced approximately 250 μm apart and 24 ICMS sites were used to map $M1_{FL}$ (Fig. 4.2 **a**).

Movements were visually scored and movement probability maps were generated for forelimb, hindlimb, wrist/digits and trunk (Fig. 4.2 **b**). The centre of $M1_{FL}$ was located 0.3 mm rostral and 1.5 mm lateral to bregma. Consistent with previous studies, it was found that the motor areas are significantly overlapped (Wang et al., 2011; Tennant et al., 2011): in many occasions, brief low current stimulation of a single spot

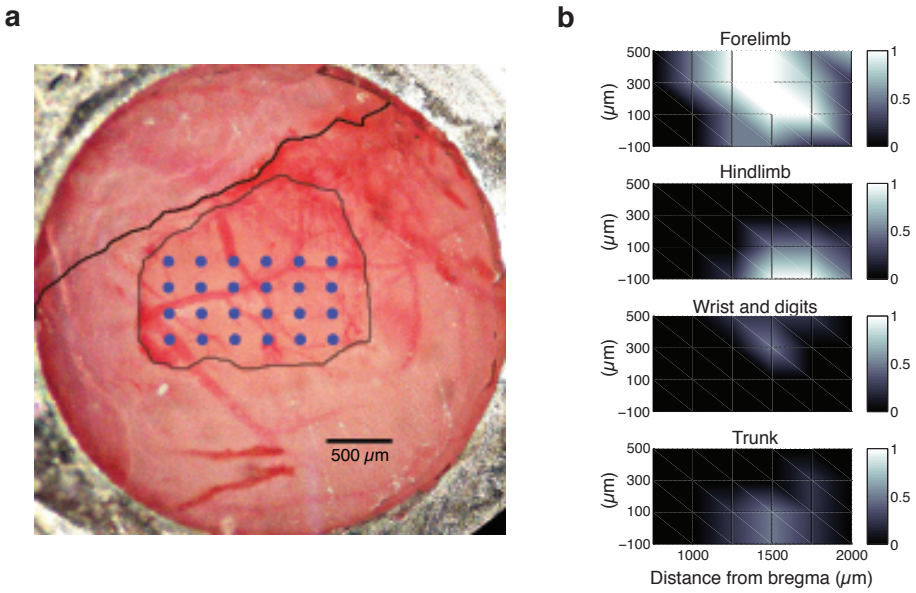

Figure 4.2: Intracortical microstimulation (ICMS) mapping of forelimb motor cortex. **a)** Brightfield image of the forelimb region of primary motor cortex. Black line represents the coronal suture with bregma located on the left. The grey encircled area represents the craniotomy and blue dots represent 24 ICMS sites. **b)** Movement probability map for forelimb, hindlimb, wrist/digits and trunk.

was able to evoke twitches in more than one muscle. Often forelimb and trunk or forelimb and hindlimb were activated at the same time. Sporadically, also ipsilateral forelimb muscle twitches were observed. Although this feature was not further investigated, it was observed before (Tennant et al., 2011).

4.2.3 *In vivo electrophysiology*

To measure subthreshold, spiking and network activity of pyramidal neurons in the primary motor cortex of awake mice, we performed patch-clamp and LFP recordings. Mice were habituated to the head-restraint and experimental setup for 45 - 60 mins before each recording session.

To confirm changes in behavioral state - quiet wakefulness to movement - local field potentials (LFPs) were recorded in $M1_{FL}$ L5B of head-restrained mice. Low-resistance ($1-2M\Omega$) glass micropipettes were filled with external solution and LFP signals were high-pass filtered at 1 Hz.

Whole-cell patch clamp recordings were obtained from awake head-restrained mice as described previously (Crochet and Petersen, 2006; Poulet and Petersen, 2008). Recordings were made at a depth of 180 – 420 μm (layer 2/3) or 620 – 880 μm (layer

5B) from the pial surface, using a Multiclamp 700B amplifier (Molecular Devices, USA). Signals were filtered at 10 kHz and acquired at 20 kHz using PClamp 10 software in conjunction with a DigiData 1440 DAC interface (Molecular Devices). Unless mentioned, no bias current was injected during recording, and the junction potential was not corrected. Resting membrane potentials were recorded immediately after attaining whole-cell configuration ("break-in"). Series resistances (R_s) ranged from 15-40 MΩ and experiments were terminated if R_s exceeded 60 MΩ. Current injection was performed only if Rs was < 35 MΩ. Patch pipettes (5-7 MΩ) were filled with internal solution (285-295 mOsm) containing (in mM) 135 K-gluconate, 4 KCl, 10 HEPES, 10 sodium phosphocreatine, 2 MgATP, 2 Na_2ATP, 0.5 Na_2GTP and 2 mg/ml biocytin (pH adjusted to 7.2 with KOH). External solution contained (in mM): 150 NaCl, 2.5 KCl, 10 HEPES, 1 $CaCl_2$, 1 $MgCl_2$ (adjusted to pH 7.3 with NaOH).

4.2.4 *Motion index and motor pattern discrimination*

To select periods of self-paced voluntary movement and locomotion of the mouse on the treadmill, we used an an optical encoder and a moderate speed (60 fps) camera synchronised with each electrophysiological recording. The optical encoder was used to capture movement of the treadmill. Locomotion was defined as periods where speed > 0.01 m/s for more than 2 s (Dombeck et al., 2009). The videos were used to define a region-of-interest (ROI) covering the contralateral forelimb of the mouse. We calculated the motion index (MI) for each successive frame as $\mathrm{MI}_f = \Sigma_{i=1}^{N}(c_{f+1,i} - c_{f,i})^2$, where $c_{f,i}$ is the greyscale level of the pixel i of the ROI in the frame f. We defined *grooming* as periods with no *locomotion* and MI$> \theta_m$, where threshold θ_m was determined by visual inspection. Periods shorter than 2 s were not included in the analysis. Further, we defined *movement* as periods of *locomotion* or *grooming*.

4.2.5 *Functional classification of recorded neurons*

We grouped the neurons into functional sub-classes, according to their movement-related firing rate change. L5B neurons display enhanced or suppressed (e.g. bidirectional) firing rate changes during movement.

For each L5B cell, (i) we divided quiet periods into 1 second epochs, (ii) randomly assigned each epoch into two groups – quiet 1 (q1), quiet 2 (q2) – and (iii) calculated the firing rate difference between q1 and q2. We repeated steps (i) to (iii) 10000 times for each cell to obtain the distribution probability of the difference of firing rate in q1 and q2 (see Fig. 4.7). If during movement, the firing rate change was higher than the 99^{th} percentile or lower than the 1^{st} percentile we classify the neuron as enhanced or

suppressed, respectively. If the firing rate change fell within the 1^{st} and 99^{th} percentile the cell was classified as non-responding.

4.2.6 *Current injection and spiking probability*

To investigate how behavioural state affected input-output transformations in different subpopulations of L5B pyramidal neurons, we measured changes in firing probability in response to somatic current injection during quiet wakefulness and movement. We injected exponentially decaying EPSCs $I(t) = ae^{-t/\tau}$ of variable size a and fixed decay $\tau_s = 5$ ms (Rossant et al., 2011). EPSCs of different amplitude (in total 80 for each amplitude, range 40-1200 pA) were injected in random order with 100 ± 10 ms intervals. To calculate the relationship between EPSP and EPSC size, we injected a series of 30 EPSCs and measured the average peak EPSP.

To estimate the probability p_i of producing an extra spike, we counted the number of spikes in the 10 ms following and in the 10 ms preceding the EPSC injection. We calculated p_i as the fraction of EPSCs injections of size a_i that produce an extra spike.

In a simple neural model (Rossant et al., 2011), the probability function $P(w)$ that an EPSP of size w causes a spike is $P(w) = \int_{\theta_r - w}^{\theta_r} p(V)dV$, defining the membrane potential distribution $p(V)$ and the spike threshold θ_r relative to the mean V_m. If we assume a Gaussian distribution for $p(V)$, with zero mean and standard deviation σ, one has

$$P(w) = \frac{1}{2}\Big[\mathrm{erf}\Big(\frac{\theta_r}{\sigma\sqrt{2}}\Big) - \mathrm{erf}\Big(\frac{\theta_r - w}{\sigma\sqrt{2}}\Big)\Big], \tag{4.1}$$

where erf is the error function.

For each neuron i, we fitted $P_{quiet}(w)$ and $P_{mov}(w)$, thus we calculated the *sensitivity ratio* $S(w) = P_{mov}(w)/P_{quiet}(w)$ and its average $(0 - 8$ mV).

4.2.7 *Intrinsic properties and morphological reconstructions*

We measured the intrinsic properties of L5B pyramidal neurons and determined their morphology to investigate whether they correlate with their functional classification defined above.

Spike threshold was defined as the maximum of the second derivative of the voltage trace $V_m(t)$ (Henze and Buzsáki, 2001; Rossant et al., 2011). Spike FWHM is the width of the spike measured at half of the distance between the threshold and the peak. dV/dt peak:trough is the ratio of the peak to the trough of the voltage derivative, previously used to characterise different neuron types (Gentet et al., 2010). Spike

accommodation was measured by injecting 60 depolarizing current steps (0.5 s long, 100-500 pA depending on the input resistance). Accommodation index was defined as $(ISI_2 - ISI_1)/ISI_1$, where ISI_1 and ISI_2 are the first and second inter-spike intervals at the beginning of each current step (Buchanan et al., 2012). Membrane potential sag was measured using hyperpolarising current steps (250 ms, −100-500 pA depending on the input resistance) and calculated as the percentage difference between the peak amplitude of the initial response (0-0.1 s) relative to the peak amplitude of the steady state response (0.15-0.25 s) (Suter et al., 2013).

After each recording deeply anesthetised mice were transcardially perfused with 4% para- formaldehyde. Brains were post-fixed overnight and coronal sections (60 or 100 μm) of M1 and tracer injection sites were cut using a vibrating microtome. For morphological reconstructions, sections were incubated in streptavidin AlexaFluor-488 (1:1000, catalog no. S11223, Molecular Probes) in 0.1 M phosphate buffered saline (PBS) containing 0.5% Triton X-100 then mounted (Vectashield, VectorLabs) and images were taken using a Zeiss LSM 510 Meta confocal microscope (20x objective). Morphological reconstructions were generated from 60μm z-stacks using NeuronJ (ImageJ plugin).

4.2.8 *Identification of projection targets*

We identified the projection targets of L5B neurons, pyramidal tract (PT) or intratelencephalic (IT), to investigate whether they correlate with the functional classification. We adopted two strategies: (i) retrograde tracing using fluorescent microspheres and (ii) multi-labelling of transcription factors.

4.2.8.1 *Retrograde tracing of projection targets*

Projection targets of individual neurons were identified by injecting fluorescent retrograde microspheres (RetroBeads, Lumafluor, USA) into the ipsilateral pons and contralateral hemisphere (dorsal striatum, corpus callosum and overlying cortex) under isoflurane anesthesia (1 − 1.5%) (Reiner et al., 2003; Hooks et al., 2013). Stereotaxic coordinates (Paxinos and Franklin, 2004) and volumes for pons injections were: 0.4 mm lateral, 3.9 and 4.1 mm posterior to bregma, 0.2 (75 nl), 0.4 (75 nl) and 0.6 mm (50 nl) from the ventral surface of the brain, green beads. For the dorsal striatum: 2.0 mm lateral, 0.2 and 0.6 mm anterior to bregma and 2.7, 2.5 and 2.2 mm ventral to the pial surface, 6 × 50 nl, red beads. 2-3 days after injection mice were transcardially perfused with 4% paraformaldehyde and brains processed to identify injection sites and retrograde staining in cortex (Fig. 4.3 **a-d**).

4.2.8.2 *Multi-labelling immunohistochemistry*

To identify projection targets of individually recorded neurons, sections were further processed by heat-mediated antigen retrieval in 10 mM sodium citrate buffer (pH 6.0) for 3 hrs at 80 °C. Sections were incubated in blocking solution (0.01 M PBS, 10 % normal goat serum (vol/vol), 0.5 % Triton X-100 (vol/vol) at 22 °C for 2 hrs and incubated overnight at 22 °C in a primary antibody mixture containing mouse monoclonal anti-Satb2 (1:200, Cat. No. ab51502, Abcam) and rat monoclonal anti-Ctip2 (1:1000, Cat. No. ab18465, Abcam) (Lickiss et al., 2012; Yasvoina et al., 2013) dissolved in carrier solution (0.01 M PBS, 1 % goat serum, 0.5 % Triton X-100). Slices were incubated overnight at 22 °C in a secondary antibody mixture containing AlexaFluor-568 goat anti-mouse (1:750, Molecular Probes) and AlexaFluor-647 goat anti-rat (1:750, Molecular Probes) dissolved in carrier solution (0.01 M PBS, 1 % goat serum, 0.5 % Triton X-100). Slices were mounted and imaged using a Nikon A1R FLIM confocal microscope (Nikon, Europe). A sequential imaging protocol was used to minimise cross talk between fluorophores. Images were analyzed offline using ImageJ.

Previous reports have described the selective molecular expression profiles of cortical projection neurons during development with the transcription factor Ctip2 being a selective marker for PT-type neurons and Satb2 a marker for IT-type neurons (Arlotta et al., 2005; Molyneaux et al., 2007; Yasvoina et al., 2013). We independently validated the selective expression of Ctip2 and Satb2 in PT and IT neurons respectively, by combining retrograde tracing with post hoc Ctip2/Satb2 immunohisto- chemistry (Fig. 4.3 **e-f**). Quantification of Ctip2 or Satb2 expression in individual, retrogradely identified L5B pyramidal neurons confirmed that all retrogradely labeled PT neurons were Ctip2 immunopositive, with only a small proportion of neurons co-expressing Ctip2 and Satb2 (9.7 %, Fig. 4.3 **g** left). Similarly, all retrogradely identified IT neurons expressed Satb2, with a minority expressing both molecular markers (2.7 %, Fig. 4.3 **g** right). For a subset of neurons we employed a dual strategy combining post hoc immunohistochemistry and morphological analysis to confirm the mixed PT- and IT-type projection-class identity of $L5B_{enh}$ and $L5B_{supp}$ subpopulations.

4.2.9 *Membrane potential dynamics*

To better understand the mechanisms underpinning firing rate and input-sensitivity changes of L5B neurons during movement, we analysed in depth the statistical properties of their membrane potential. Analysis of the subthreshold V_m dynamics was performed after clipping spikes from threshold to 3 ms after the peak (changing the

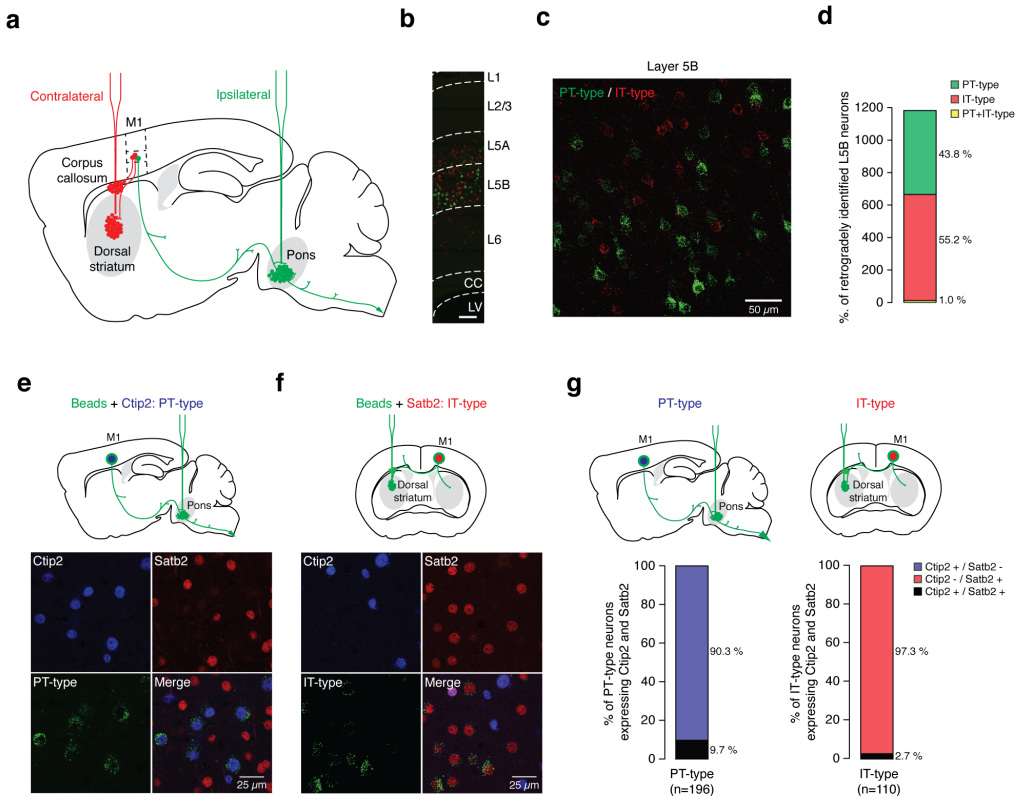

Figure 4.3: Classification of L5B projection neurons based on retrograde tracing and molecular marker expression. **a)** Schematic parasagittal brain section illustrating retrograde fluorescent bead injection sites. Red fluorescent beads were injected into the contralateral dorsal striatum and corpus callosum to identify intratelencephalic (IT-type) projection neurons. Green fluorescent beads were injected into the ipsilateral pons to identify pyramidal tract (PT-type) projection neurons. **b-c)** Distribution of PT-type (green) and IT-type (red) projection neurons across different cortical layers (**b**) and within L5B (**c**) of the forelimb region of M1. LV: lateral ventricle; CC: corpus callosum. (**d**) Relative distributions of PT-type (green) and IT-type (red) projection neurons in L5B of forelimb motor cortex (n = 1183 neurons, 50 slices, 6 mice). **e-f)** Single retrograde tracing and immunohistochemical staining confirming transcription factors Ctip2 and Satb2 are molecular markers for retrogradely identified PT-type (ipsilateral pons injection, (**e**)) and IT-type (contralateral dorsal striatum injection, (**f**)) neurons, respectively. **g)** Relative distribution of retrogradely identified L5B neurons expressing Ctip2 or Satb2 (n = 306 neurons, 24 slices, 4 mice).
Figure prepared by Julia Schiemann, data collected by Julia Schiemann with the help of Paolo Puggioni and Joshua Dacre.

clipping window to 10 ms before and 20 ms after each spike did not alter the results). The average standard deviation of the voltage σ_{V_m} was calculated as the average over non-overlapping periods of 1 s.

We measured the power-spectra of V_m with 75% overlapping Bartlett 1 s windows. The mean population spectrum was the average of the single cell spectra. The δ-band power δ_P was calculated as the integral of the power-spectrum between 1.5 and 4 Hz. The β-band was calculated between 12 and 30 Hz.

The time-frequency spectrograms of the subthreshold voltage were computed with a continuous Morlet wavelet transform

$$\psi(t) = e^{i2\pi f_0 t} e^{-t^2/2}, \tag{4.2}$$

where $2\pi f_0 = 6$ rad s^{-1}. The coefficients are

$$CWT_V^{\psi}(\tau, s) = 1/\sqrt{s} \int V(t)\psi^*((t-\tau)/s)dt, \tag{4.3}$$

where τ is the time shift and s the scaling factor. We calculate the Fourier frequency ν that corresponds to the scaling factor s by using the approximated conversion formula $\nu = (2\pi f_0 + \sqrt{2 + 2\pi f_0^2})/4\pi s$ (Torrence and Compo, 1998). The power at time τ and frequency ν is the square of the coefficient $CWT_V^{\psi}(\tau, s)$.

4.2.10 *Effective input resistance and membrane time constant*

In vivo, synaptic conductances dramatically alter the input resistance of neurons (Destexhe et al., 2003). To test whether this effect was responsible of the firing rate and input-sensitivity changes of L5B neurons in M1, we measured the effective input resistance of a subset of recorded neurons. We defined the effective input resistance as $R_{\text{eff}} = 1/G_{\text{tot}}$, the inverse of the total conductance $G_{\text{tot}} = G_L + \langle G_e \rangle + \langle G_i \rangle$, sum of the leak conductance G_L and the average synaptic excitatory and inhibitory conductances $\langle G_e \rangle$ and $\langle G_i \rangle$. The effective time constant is $\tau_{\text{eff}} = R_{\text{eff}}C$, where C is the capacitance. R_{eff} and τ_{eff} were estimated from the current injection experiment, calculating the average response to subthreshold injections with more than 20 pulses. We computed the complex impedance

$$Z(f) = V(f)/I(f), \tag{4.4}$$

where $V(f)$ and $I(f)$ are respectively the Fourier transform of average voltage response and injected current. We assume a linear RC filter of the membrane (see sec-

tion 2.3) and we estimate R_{eff} and τ_{eff} by fitting the module of the impedance with

$$|Z(f)| = R_{\text{eff}} / \sqrt{1 + (2\pi f \tau_{\text{eff}})^2}. \tag{4.5}$$

As already discussed in 2.1.2 and 2.4, the interpretation of *in vivo* measurements of R_{eff} is difficult. In fact, while the measurement takes place in the soma of the neuron, synaptic inputs target mostly the dendritic tree. This means that the quantity measured might have little to do with the resistance at the synaptic sites. R_{eff} is commonly used in *in vivo* electrophysiology literature as a proxy for the synaptic activity of the neuron (Destexhe and Paré, 1999; Gentet et al., 2010; Haider et al., 2012). However, we must be weary on interpreting the results. Intuitively, a lower input resistance measured at the soma is an indication of a higher synaptic activity, but we drawing solid quantitative conclusions is certainly problematic.

4.2.11 *Modulation of V_m power in the δ-band during quiet wakefulness*

The waking period is characterised by a continuum of cortical states corresponding to varying levels of spontaneous fluctuations in neural population activity (Harris and Thiele, 2011). To investigate whether slow large amplitude membrane potential fluctuations (normally associated to quiet wakefulness) were persistent or transient, we integrated V_m STFT power in the δ-band ($1.5 - 4$ Hz) with 3 s sliding Hamming windows (Fig. 4.4 **a**). For each cell, we compute the probability distribution of δ power for movement and quiet wakefulness and defined as power threshold the 90^{th} percentile of the distribution during movement (Fig. 4.4 **b**). Thus, we calculated the portion of time that during quiet wakefulness the δ power is lower than the power threshold.

4.2.12 *Detection of compound synaptic events*

To understand how excitatory inputs change during movement in different functional sub-classes of L5B pyramidal neurons, we developed an event detection algorithm that measured the frequency of large compound synaptic events. We could faithfully detect compound synaptic events occurring in a time window (5 ms) shorter than the average membrane time constant (8.2 ± 2.3 ms) and with a detection threshold of 1 mV. Events that occurred within ± 10 ms of a spike were discarded (Fig. 4.5 **a**). To assess the reliability of our event detection algorithm we simulated noisy membrane potential traces (100 s in duration using Ornstein-Uhlenbeck processes) and manually

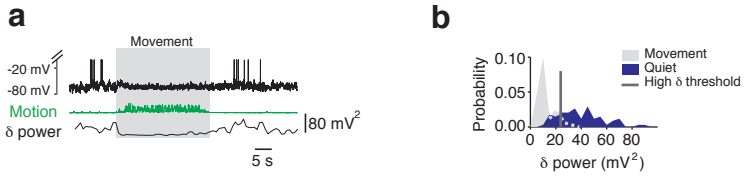

Figure 4.4: δ power distribution during quiet wakefulness and movement in a L2/3 pyramidal neuron in M1 (same analysis applies to L5B neurons). **a)** Representative voltage trace, motion index and V_m δ power for a L2/3 pyramidal neuron during quiet wakefulness and movement. During movement, δ power remains low while during quiet wakefulness there are periods of high and low δ power. **b)** δ power distribution in a L2/3 pyramidal neuron during quiet wakefulness (blue) and movement (grey). The bar represents the 95^{th} percentile of the movement distribution and is the threshold for classifying periods of high and low δ power during quiet wakefulness.

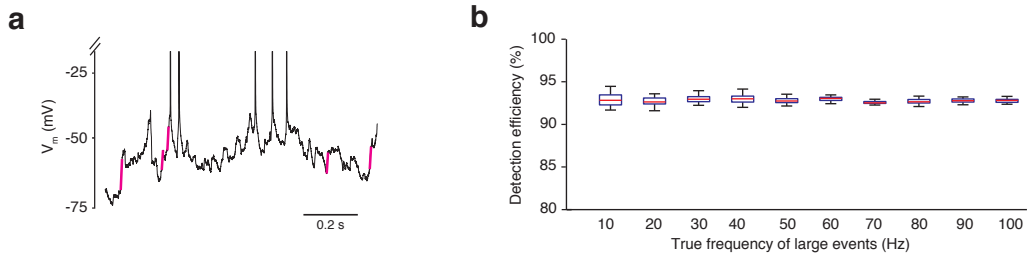

Figure 4.5: Event detection validation. **a)** Representative trace, where large events are highlighted with purple bars. **b)** Reliability of the event detection algorithm: fraction of recovered events for different input frequencies.

added events of known amplitude at frequencies ranging from $5 - 100$ Hz. For each frequency range 30 simulations were run and the mean detection efficiency computed (range $90 - 95\%$) across the entire frequency range (Fig. 4.5 **b**).

4.2.13 *Statistics*

Summary data are expressed as mean $\pm$ standard deviation unless otherwise stated. Statistical significance was determined using Wilcoxon signed-rank tests (paired data) and rank-sum tests (unpaired data) unless otherwise stated. Wilcoxon signed-rank tests on the areas underlying the rate density curves were used in Fig. 4.15 **b-c**. The relative distribution of functional phenotypes (supp, enh, n-r) were analysed using Pearson χ^2 test statistics (based on 10^6 permutations). For statistical tests, $p < 0.05$ was considered significant (*$p < 0.05$ and ** $p < 0.01$).

4.3 RESULTS

4.3.1 *Membrane potential dynamics of L5B pyramidal neurons during self-paced, voluntary movement*

To investigate the cellular mechanisms underpinning behavioral state-dependent modulation of M1 output, we obtained whole-cell patch-clamp recordings from the primary output layer of M1 (L5B, forelimb motor cortex, $620 - 880\,\mu$m from the pial surface, see section 4.2.3, $n = 45$) (Anderson et al., 2010; Sheets et al., 2011; Suter et al., 2013) during quiet wakefulness and self-paced, voluntary movements (e.g. walking, running or grooming on a single axis, cylindrical treadmill) (Fig. 4.6 **a**). Consistent with previous reports, transitions from quiet wakefulness to movement were characterised by the desynchronisation of cortical activity, reflected in the reduced variability of the local field potential (Fig. 4.6 **b**) (Crochet and Petersen, 2006; Poulet and Petersen, 2008). The observed desynchronisation is probably a consequence of the change in attentional state (Harris and Thiele, 2011), associated to movement preparation (Churchland et al., 2006b) and execution (Steriade et al., 1993b; Polack et al., 2013). During periods of quiet wakefulness, all L5B pyramidal neurons displayed large-amplitude V_m fluctuations (σ_{V_m} 3.9 ± 1.3 mV) and a relatively depolarised average resting V_m (μ_{V_m} -50.8 ± 5.4 mV). The interplay between mean V_m, distance from threshold and V_m variability resulted in moderate basal firing rates (5.9 ± 3.8 Hz, range $0.0 - 15.9$ Hz) (two representative traces in Fig. 4.6 **c-d**).

During changes in behavioral state from quiet wakefulness to movement the vast majority of L5B pyramidal neurons ($\sim$ 90%) displayed significant modulation of their basal firing rates. To functionally classify individual neurons we compared the variability in quiet wakefulness firing rate with the average firing rate during self-paced movement (Fig. 4.7 and section 4.2.5). If the average movement-related firing rate change was lower than the 1^{st} percentile of the distribution of firing rate changes during quiet wakefulness, neurons were classified as suppressed ($L5B_{supp}$, $n = 17$) (Figures 4.7 **a**, 4.6 **c-d** (top), Table 4.1). Neurons that displayed an average movement-related firing rate change above the 99^{th} percentile were classified as enhanced ($L5B_{enh}$, $n = 24$) (Figures 4.7 **c**, 4.6 **c-d** (bottom), Table 4.1). A small proportion of L5B neurons ($n = 4/45$) did not significantly change their firing rates during movement and were classified as non-responding neurons ($L5B_{n-r}$) (Fig. 4.7 **b** and 4.7 **g-i**). The proportion of L5 pyramidal neurons in which spike frequency decreased (37.8%), increased (53.3%) or did not change (9%) during movement was consistent with pre-

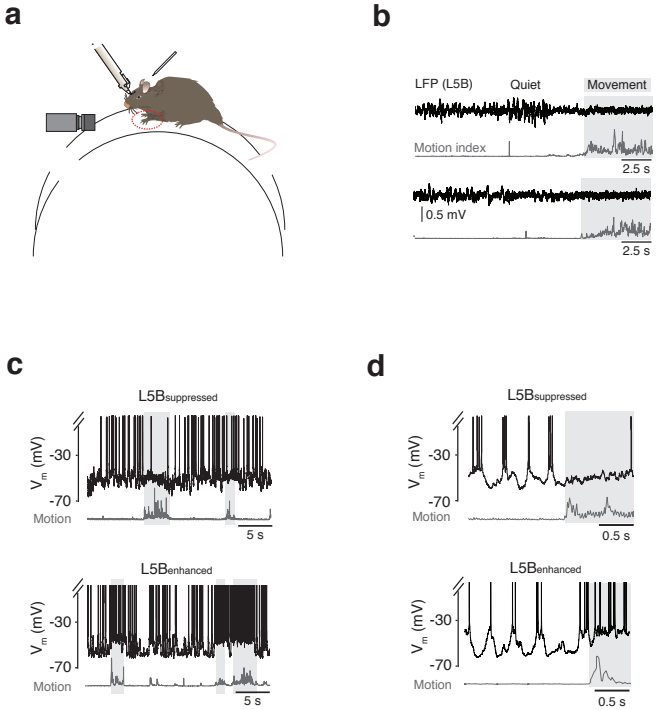

Figure 4.6: Whole-cell recordings of L5B pyramidal neurons in primary motor cortex during self-paced, voluntary movement. **a)** Patch-clamp recording configuration in head-fixed mice mounted on a single axis, cylindrical treadmill. Digital imaging (60 fps) was used to confirm changes in behavioral state – quiet wakefulness to movement – and to calculate motion index. **b)** Local field potential (LFP) recordings (black traces) of L5B activity and motion index (grey). **c-d)** Representative voltage traces (**c**) and higher time resolution examples (**d**) from a L5B suppressed (upper panels, firing rate suppressed during movement) and L5B enhanced (lower panels, firing rate enhanced during movement) pyramidal neuron during quiet wakefulness and movement (light grey shading). The motion index (dark grey) defines the magnitude and duration of each forelimb movement. In this figure and all subsequent figures action potentials have been truncated to highlight subthreshold V_m changes during movement.

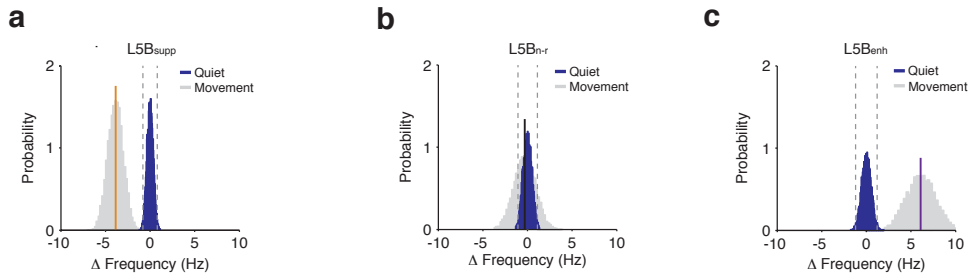

Figure 4.7: Functional classification of L5B pyramidal neurons. Representative Δ firing rate probability distributions during quiet wakefulness (blue) and movement (grey) in $L5B_{supp}$ (**a**), $L5B_{n-r}$ (**b**) and $L5B_{enh}$ (**c**) neurons. grey dotted lines represent the 1^{st} (left) and 99^{th} (right) percentiles. Solid colored lines represent the average firing rate change in a $L5B_{supp}$ (yellow), $L5B_{n-r}$ (black) and $L5B_{enh}$ (purple) neuron during movement.

vious reports (Beloozerova et al., 2003; Costa et al., 2004).

We next investigated the subthreshold mechanisms underpinning bidirectional modulation of M1 output during self-paced movement. During movement, $L5B_{supp}$ neurons displayed $\sim$ 1 mV hyperpolarization in mean V_m ($p = 2 \times 10^{-2}$) and reduced V_m variability (σ_{V_m} quiet 3.5 ± 0.8 mV, movement 2.5 ± 0.5 mV, $p = 3 \times 10^{-4}$), which lowered the probability of reaching threshold and reduced overall firing rates (quiet 6.4 ± 3.9 Hz, movement 2.8 ± 2.5 Hz, $p = 3 \times 10^{-4}$) (Fig. 4.8 **a-c, j,l**). In $L5B_{enh}$ neurons, movement also reduced V_m variability (σ_{V_m} quiet 4.1 ± 1.5 mV, movement 3.2 ± 0.8 mV, $p = 2 \times 10^{-3}$) but this was counteracted by a depolarization in average V_m (quiet -52.1 ± 5.3 mV, movement -47.9 ± 4.8 mV, $p = 2 \times 10^{-6}$), which significantly increased spike probability and firing rates (quiet 5.7 ± 3.8 Hz, movement 12.9 ± 7.4 Hz, $p = 2 \times 10^{-5}$) (Fig. 4.8 **d-f, k,l**). By contrast, the V_m dynamics and firing rates of $L5B_{n-r}$ neurons were not affected by the transition from quiet wakefulness to movement (Fig. 4.8 **g-i**).

Interestingly, the functional classification of L5B pyramidal neurons ($L5B_{supp}$ vs $L5B_{enh}$) was not dependent on the type of motor behavior being executed (e.g. locomotion vs grooming; Fig. 4.9), basic electrophysiological properties (Table 4.1), projection-class identity of individual neurons (pyramidal tract, PT-type vs intratelencephalic, IT-type neurons; Fig. 4.10 **a-b**), morphology (e.g. thin tufted vs. thick tufted neurons, Fig. 4.10 **c**), depth (Fig. 4.10 **d**) or location (Fig. 4.10 **e**).

Our results demonstrate that movement-related modulation of $L5B_{enh}$ firing rates is primarily mediated by a tonic depolarization in V_m. Reduced firing rates in $L5B_{supp}$

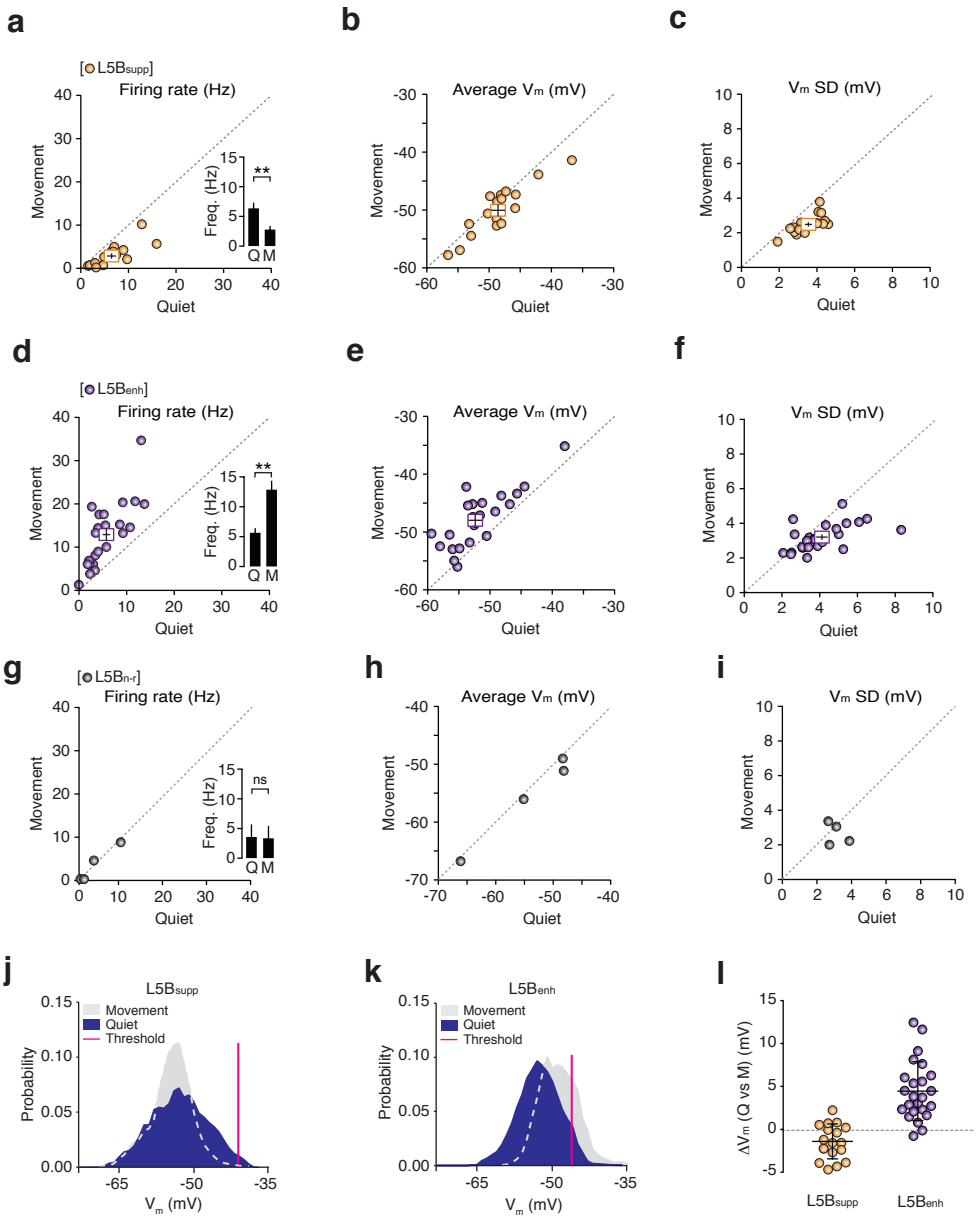

Figure 4.8: Firing rates and subthreshold features of L5B pyramidal neurons during quiet wakefulness and movement. **a-c)** Average firing rate (**a**), V_m (**b**) and σ_{V_m} (**c**) in $L5B_{supp}$ pyramidal neurons (yellow symbols, $n = 17$) during quiet wakefulness and movement. Filled circles represent data from individual neurons while square symbols represent mean $\pm$ standard error. Inset in (**a**) depicts the average $L5B_{supp}$ neuron firing rate during quiet wakefulness (Q) and movement (M). $^{**}p < 0.01$. **d-f)** Same as (**a-c**) for $L5B_{enh}$ neurons. Purple symbols ($n = 24$) represent individual neurons. **g-i)** Same as (**a-c**) for $L5B_{n-r}$ neurons. Black symbols ($n = 4$) represent individual neurons. **j-k**Representative V_m distributions for a $L5B_{supp}$ (**j**) and $L5B_{enh}$ (**k**) pyramidal neuron during quiet wakefulness and movement. Magenta bars denote the median spike threshold. **l)** Change in average V_m (ΔV_m) from quiet wakefulness to movement in $L5B_{supp}$ (yellow symbols) and $L5B_{enh}$ (purple symbols). Filled circles represent data from individual neurons and black bars represent mean $\pm$ standard deviation.

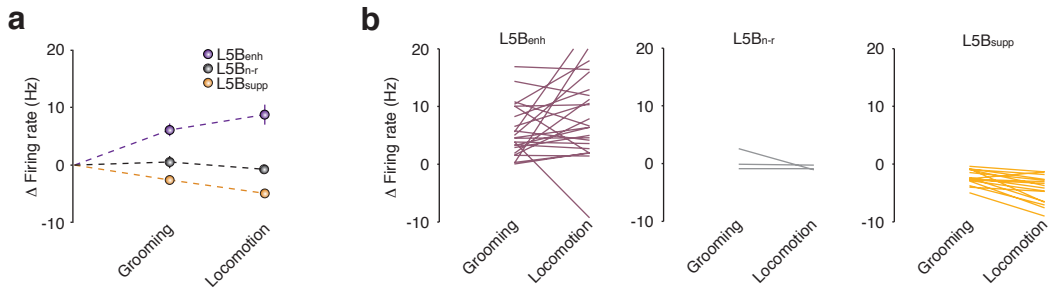

Figure 4.9: Functional classification of L5B pyramidal neurons is not dependent on the type of motor behavior. **a**) Average firing rate changes (relative to quiet wakefulness) in $L5B_{supp}$ (yellow, $n = 17$), $L5B_{n-r}$ (black, $n = 4$) and $L5B_{enh}$ (purple, $n = 24$) neurons during grooming or locomotion. **b**) Firing rate changes (relative to quiet wakefulness) for all the recorded neurons, split in the three classes: $L5B_{enh}$ (left), $L5B_{n\text{-}s}$ (centre), and $L5B_{supp}$ (right). With one exception only, neurons belong to the same class even during different motor behaviours.

Intrinsic properties of $L5B_{supp}$ and $L5B_{enh}$ neurons during quiet wakefulness

	$L5B_{supp}$	n	$L5B_{enh}$	n	p-value
Firing rate (Hz)	6.3 ± 3.9	17	5.7 ± 3.8	24	0.587
Mean Vm (mV)	-49.0 ± 4.7	17	-52.0 ± 5.3	24	0.061
Std. Vm (mV)	3.5 ± 0.8	17	4.1 ± 1.1	24	0.375
C (pF)	85 ± 17	5	76 ± 16	5	0.217
Input Resistance (MΩ)	85.3 ± 23.7	5	96.4 ± 17.5	5	0.487
Membrane time constant (ms)	8.6 ± 2.0	5	7.8 ± 1.1	5	0.625
Spike threshold (mV)	-39.1 ± 5.2	17	-40.6 ± 4.0	24	0.390
Spike FWHM (ms)	1.1 ± 0.4	17	1.0 ± 0.4	24	0.420
Spike dV/dt peak:trough	3.0 ± 0.8	17	3.0 ± 0.6	24	0.989
Accommodation	0.6 ± 0.3	4	0.8 ± 0.4	7	0.297
Sag (%)	3.8 ± 2.4	6	4.3 ± 4.4	15	0.974

Table 4.1: Intrinsic properties of M1 $L5B_{supp}$ and $L5B_{enh}$ pyramidal neurons recorded during quiet wakefulness.

neurons result from a moderate hyperpolarization and significant reduction in V_m variance.

4.3.2 *Bidirectional input sensitivity modulation during voluntary movement*

Behavioral state-dependent changes in V_m dynamics can profoundly affect the integrative mode and output firing patterns of neocortical neurons (Haider and McCormick, 2009; Rudolph-Lilith and Destexhe, 2003; Destexhe et al., 2003). What effects

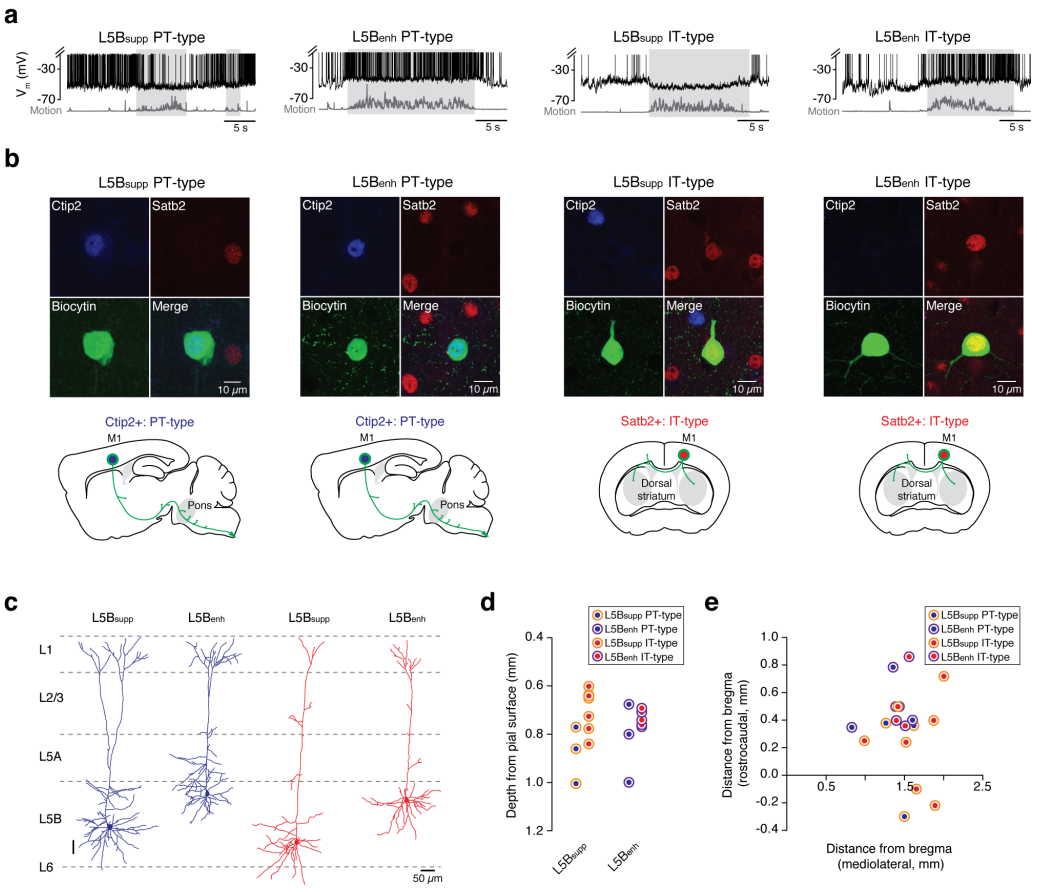

Figure 4.10: Projection class identity of individually recorded $L5B_{supp}$ and $L5B_{enh}$ neurons. **a)** Representative voltage traces from identified: $L5B_{supp}$ PT-type; $L5B_{enh}$ PT-type; $L5B_{supp}$ IT-type; and $L5B_{enh}$ IT-type during quiet wakefulness and movement (light grey shading and dark grey motion index). **b)** Upper panels: single cell biocytin labeling (green) and post-hoc immunohistochemical staining for Ctip2 (blue) and Satb2 (red) confirmed the projection class identity of individually recorded L5B pyramidal neurons. Lower panels: schematic brain sections showing $L5B_{supp}$ and $L5B_{enh}$ neurons contain a mixture of PT-type and IT-type projection neurons. **c)** Representative morphological reconstructions of $L5B_{supp}$ and $L5B_{enh}$ neurons color-coded by projection class identity (blue = PT-type, red = IT-type). **d)**Average depth of individually recorded $L5B_{supp}$ ($n = 10$) and $L5B_{enh}$ ($n = 8$) neurons color-coded by projection class identity. **e)** Neuroanatomical coordinates of individually recorded L5B pyramidal neurons plotted according to their position relative to bregma ($n = 10$ $L5B_{supp}$ neurons; $n = 8$ $L5B_{enh}$ neurons).
Figure prepared by Julia Schiemann, data collected by Julia Schiemann with the help of Paolo Puggioni and Joshua Dacre. Digital processing of the neural reconstructions by Ian Duguid.

do movement-related changes in V_m dynamics have on input-output transformations in L5B pyramidal neurons in M1? In principle, both changes in μ_{V_m}, σ_{V_m} and input resistance can profoundly influence the responsiveness and firing dynamics of a neuron (Cardin et al., 2008; Chance et al., 2002; Tiesinga et al., 2004; Hô and Destexhe, 2000).

Here, we performed current injection experiments in a small cohort of $L5B_{supp}$ and $L5B_{enh}$ neurons *in vivo* (Fig. 4.11 **a-b**, see methods 4.2.6) and measured spike probability during quiet wakefulness and voluntary movement. Although current injection at the soma disregards dendritic non-linearities, synaptic properties and locations, it provides a robust measure to assess the relationship between synaptic currents arriving at the soma and spike output probability during behavior – measured as a change in input sensitivity (Rossant et al., 2011).

During movement $L5B_{supp}$ neurons displayed a robust decrease in σ_{V_m} with no change in mean (Fig. 4.11 **c**), resulting in a 2-fold reduction in input sensitivity (Δ Sensitivity 0.6 ± 0.1, $n = 5$, Fig. 4.11 **e,g,i**).

By contrast, $L5B_{enh}$ neurons displayed both reduced $\sigma_{V_m}$and an increase in mean V_m (4.11 **d**), which together produced a 2-fold increase in input sensitivity (Δ Sensitivity 1.7 ± 0.4, $n = 6$, 4.11 **f,h,j**).

Although both L5B subpopulations displayed moderate changes in input resistance during movement they did not significantly differ from quiet wakefulness ($p = 0.32$) (Fig. 4.12). Thus, we can conclude that changes in input-sensitivity are due to the subthreshold dynamics and are not driven by variations in the conductance state.

Differential behavioral state-dependent changes in μ_{V_m} and σ_{V_m} ($L5B_{supp}$: predominately σ_{V_m} with moderate hyperpolarisation; $L5B_{enh}$: σ_{V_m} and μ_{V_m}) can switch L5B pyramidal neurons into two different integrative modes that bidirectionally modulate M1 output during self-paced movement.

4.3.3 *Behavioral state-dependent changes in network-driven Vm variance*

To investigate the mechanisms underpinning $L5B_{supp}$ and $L5B_{enh}$ neuron V_m dynamics we explored changes in V_m spectral components before and after movement onset. During quiet wakefulness, we observed slow ($1.5 - 4$ Hz, δ frequency band), large amplitude V_m fluctuations in all L5B pyramidal neurons (Fig. 4.13 **a-b**). The periods of high δ frequency power were intermittent, occurring only a fraction of the time

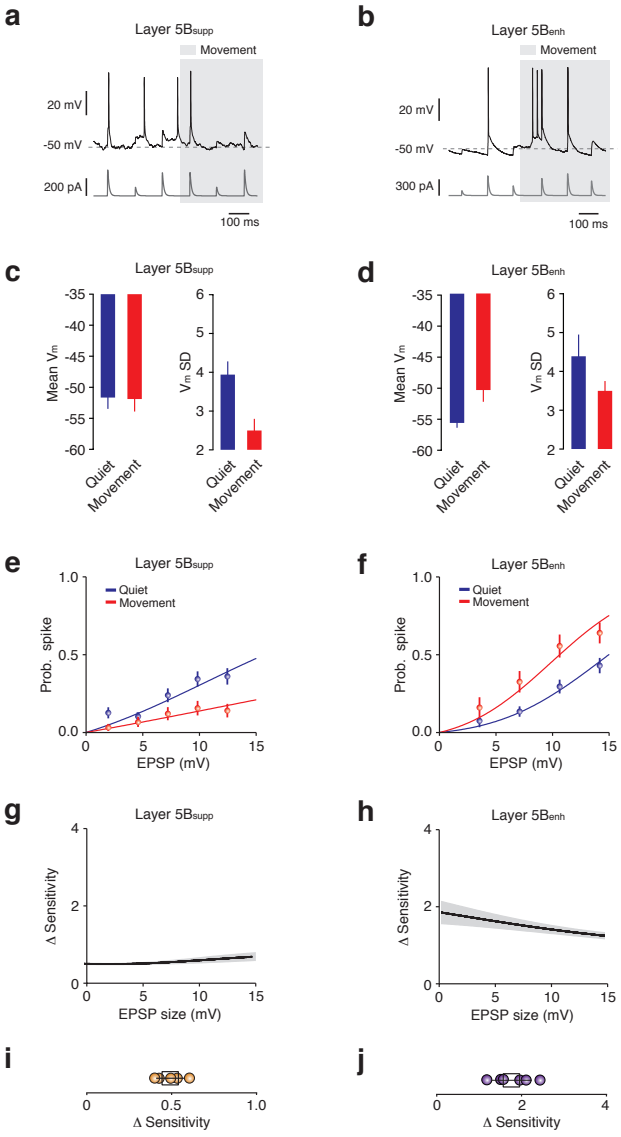

Figure 4.11: Bidirectional input sensitivity changes in L5Bsupp and L5Benh pyramidal neurons during movement. **a-b)** Representative voltage traces (black) during somatic EPSC current injections *in vivo* (grey) in a $L5B_{supp}$ (**a**) and $L5B_{enh}$ (**b**) pyramidal neuron during quiet wakefulness and movement (light grey shading). **c-d)** Average changes in μ_{V_m} and σ_{V_m} in $L5B_{supp}$ (**c**, $n = 5$) and $L5B_{enh}$ (**d**, $n = 6$) neurons during quiet wakefulness (blue) and movement (red). **e-f)** Input-output transformations in $L5B_{supp}$ (**e**) and $L5B_{enh}$ (**f**) neurons recorded *in vivo* during quiet wakefulness (blue) and movement (red). Symbols represent mean ± standard deviation; solid lines are fits to a truncated error-function (Eq. 4.1). **g-h)** Average change in spike probability as a function of increasing evoked EPSP amplitude for $L5B_{supp}$ (**g**, $n = 5$) and $L5B_{enh}$ (**h**, $n = 6$) neurons. Thick black lines represent population averages with standard deviations shown in grey. **i-j)** Mean change in input sensitivity for $L5B_{supp}$ (**i**, $n = 5$) and $L5B_{enh}$ (**j**, $n = 6$) neurons. Black symbols represents mean ± standard deviation; filled symbols represent data from individual neurons.

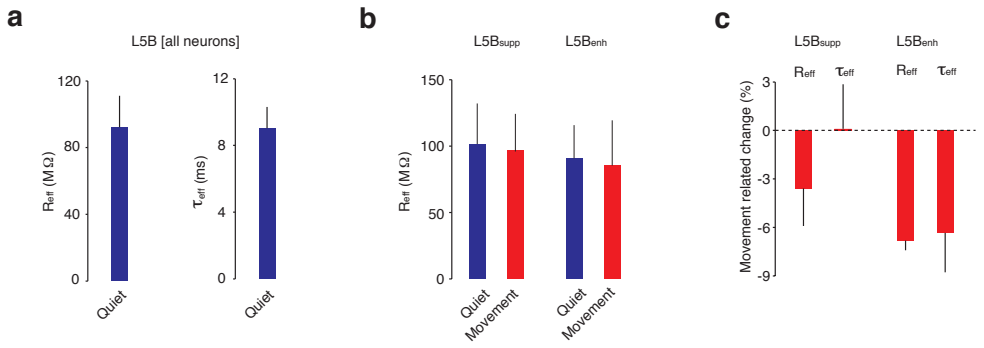

Figure 4.12: Movement-related changes in effective input resistance and membrane time constant in L5B pyramidal neurons. **a)** Input resistance (left) and membrane time constant (right) of L5B neurons ($n = 10$) during quiet wakefulness. **b)** Input resistance of $L5B_{supp}$ ($n = 5$, left) and $L5B_{enh}$ ($n = 5$, right) pyramidal neurons during quiet wakefulness (blue) and movement (red). **c)** Movement-related changes in effective input resistance (R_{eff}) and membrane time constant (τ_{eff}) for $L5B_{supp}$ ($n = 5$) and $L5B_{enh}$ ($n = 5$) pyramidal neurons. Bars represent median values $\pm$ median absolute deviation.

(Fig. 4.13 **c**), suggesting discontinuous levels of attention or arousal during quiet wakefulness (Harris and Thiele, 2011).

During movement, slow V_m fluctuations were suppressed in both subpopulations of L5B pyramidal neurons (δ power $L5B_{supp}$ quiet 7.8 ± 5.3 mV^2, movement 3.6 ± 2.1 mV^2, $n = 17$, $p = 2 \times 10^{-3}$; $L5B_{enh}$ quiet 16.4 ± 15.3 mV^2, movement 6.2 ± 5.8 mV^2, $n = 24$, $p = 10^{-4}$) (Fig. 4.13 **b, d**). The suppression of δ power led to reduced σ_{V_m}, which together with a moderate hyperpolarization (~ 1 mV) could account for the reduction in spike probability observed in $L5B_{supp}$ pyramidal neurons during movement (see Fig. 4.8).

In $L5B_{enh}$ neurons, slow V_m fluctuations were also abolished but power in the β frequency band ($12 - 30$ Hz) was increased (quiet 3.0 ± 2.1 mV^2, movement 7.4 ± 7.1 mV^2, $n = 24$, $p = 3 \times 10^{-5}$, Fig. 4.13 **d-e**). The increase in β-band power and net depolarization in V_m could account for elevated $L5B_{enh}$ firing rates during movement (see Fig. 4.8). Thus, reduced network-driven slow V_m fluctuations appear to decrease input sensitivity and neuronal excitability in $L5B_{supp}$ neurons during movement, while in $L5B_{enh}$ neurons this is counteracted by an increase in β-band power and mean V_m that elevates input sensitivity and drives neuronal output.

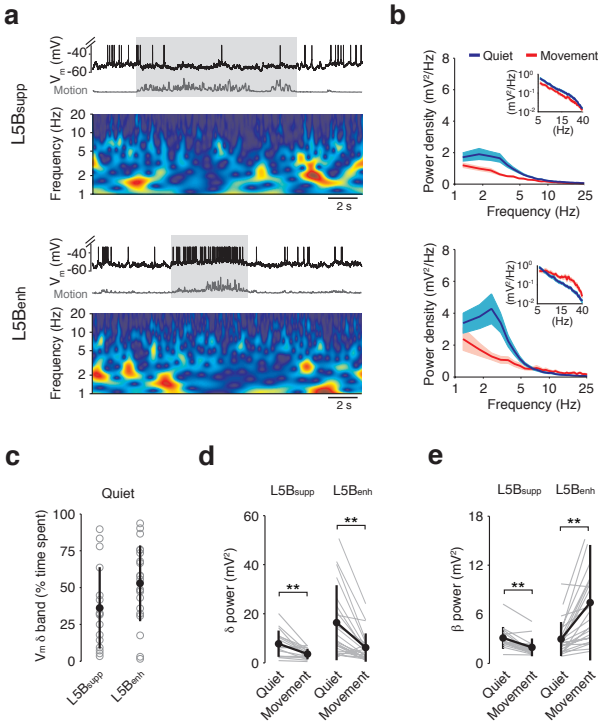

Figure 4.13: Movement-related changes in L5B membrane potential fluctuations. **a** Representative voltage traces and wavelet spectrograms for L5Bsupp (upper panels) and $L5B_{enh}$ (lower panels) pyramidal neurons during quiet wakefulness and movement (light grey shading). **b)** Average V_m power density for $L5B_{supp}$ (upper panels; $n = 17$) and $L5B_{enh}$ (lower panels; $n = 24$) pyramidal neurons during quiet wakefulness (blue) and movement (red). Data represent mean $\pm$ standard deviation. Insets show average V_m power density between 5 and 40 Hz. **c)** Fraction of time $L5B_{supp}$ and $L5B_{enh}$ pyramidal neurons spent with high power in the δ frequency band ($1.5 - 4$ Hz) during quiet wakefulness. grey circles represent data from individual neurons and black symbols represent mean $\pm$ standard deviation. **d-e)** Average V_m power in δ ($1.5 - 4$ Hz) (**d**) and β ($12 - 30$ Hz) (**e**) frequency band in $L5B_{supp}$ ($n = 17$) and $L5B_{enh}$ ($n = 24$) pyramidal neurons during quiet wakefulness and movement. grey lines represent data from individual neurons and black symbols represent mean $\pm$ standard deviation. $^{**}p = 0.01$.

4.3.4 *Increased excitatory input in $L5B_{enh}$ neurons during movement*

We next investigated the changes in input structure that could explain the V_m dynamics of L5B neurons during movement. Although voltage clamp recordings would be the ideal choice for measuring synaptic conductance changes during behavior, these methods produce incomplete voltage control of pyramidal neuron dendrites and errors in the measurement of excitatory and inhibitory conductances (Williams and Mitchell, 2008). Therefore, to address this issue we developed analytical and conductance-based computational models constrained by our experimental data (Fig. 4.12 and Table 4.1, see Chapter 2 for a full description). Our model (single compartment neuron) does not consider the spatiotemporal patterns of dendritic input or dendritic nonlinearities, but extract the effective conductances at the soma (Gerstner and Kistler, 2002). As already mentioned in section 4.2.10, we need to be careful when interpreting the results. Intuitively, a higher conductance at the soma is an indication of increased synaptic activity in the dendritic tree. However, it is hard to draw quantitative conclusions, because we only see the effect of the inputs at the somatic level.

4.3.4.1 *Estimation of the conductances*

We first used an analytical approach to estimate the movement-related changes in average excitatory and inhibitory conductance at the soma. Here we summarise the calculations - for a full description refer to Chapter 2, in particular section 2.2.

The total mean synaptic conductance is the sum of the average excitatory and inhibitory conductance ($\langle G_{syn} \rangle = \langle G_E \rangle + \langle G_I \rangle$). We calculated its value by subtracting the typical leak conductance ($G_L = 5.55$ nS) measured in vitro (Sheets et al., 2011) from the total conductance measured *in vivo* ($\langle G_{syn} \rangle = \langle G_{tot} \rangle - \langle G_L \rangle$), where $\langle G_{tot} \rangle$ is the reciprocal of the effective input resistance ($G_{tot} = 1/R_{eff}$, see Eq. 2.10 and Fig. 4.12). In a conductance-based single compartment model, the average V_m is determined by the total conductance and the ratio between excitatory and inhibitory conductances ($\gamma = \langle G_E \rangle / \langle G_i \rangle$). Thus, by just measuring the input resistance and average V_m we can estimate $\langle G_E \rangle$ and $\langle G_I \rangle$ (see Eq. 2.16 and 2.17).

During quiet wakefulness, we found G_E and G_I to be 2.5 and 2.7 nS respectively (Fig. 4.14 **a**), similar to values measured in the visual cortex of awake mice (Haider et al., 2012). The 95% confidence intervals in Fig. 4.14 **a-b** were calculated by finding pairs $(\langle G_E \rangle, \langle G_I \rangle)$ that lead to V_m and R_{eff} values within the 95% confidence interval of the data.

We then calculated the sub-population average movement-related changes: $L5B_{supp}$ cells displayed a slight hyperpolarisation ($\Delta V_m = -1.4 \pm 0.3$ mV) and a moderate

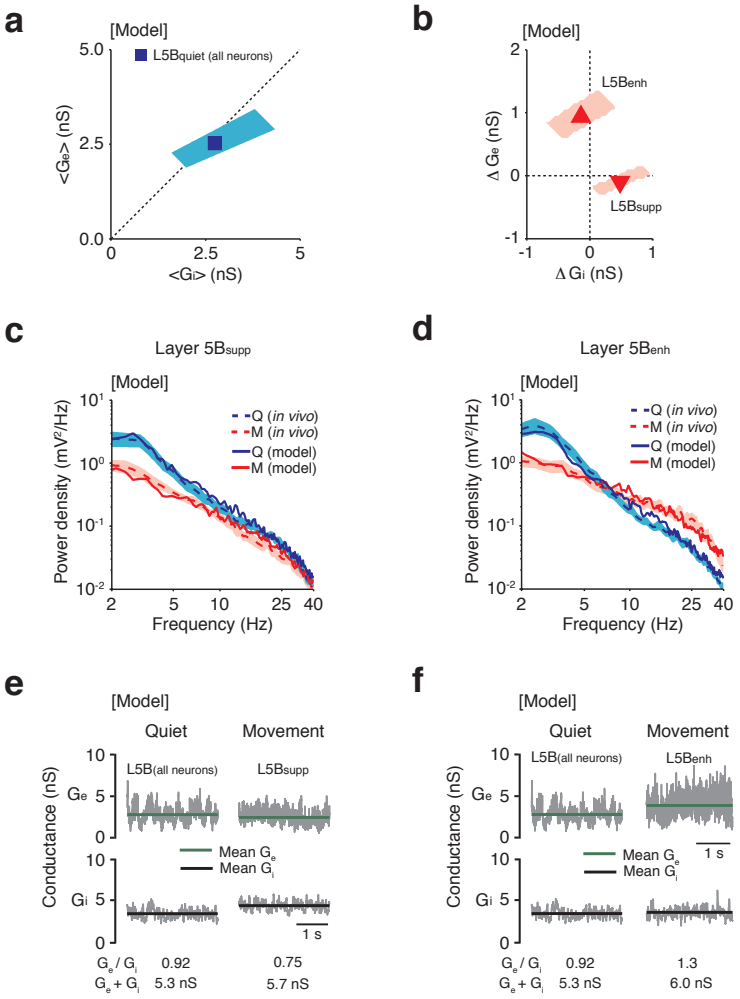

Figure 4.14: Increased excitatory drive in L5Benh neurons during movement. **a)** Estimate of the average excitatory ($\langle G_E \rangle$) and inhibitory ($\langle G_I \rangle$) conductance in L5B pyramidal neurons during quiet wakefulness ($n = 41$). Light blue shading represents the 95% confidence interval and the dashed line represents the unity line. **b)** Estimate of the average change in excitatory (ΔG_E) and inhibitory (ΔG_I) conductance in $L5B_{supp}$ (downward triangle, $n = 17$) and $L5B_{enh}$ (upward triangle, $n = 24$) pyramidal neurons during movement. Light red shading represents 95% confidence intervals. **c-d)** Simulated V_m power density plots for $L5B_{supp}$ (**c**) and $L5B_{enh}$ (**d**) pyramidal neurons during quiet wakefulness (solid blue line) and movement (solid red line). Dashed lines represent *in vivo* data from Fig. 4.13 plotted on a log scale for comparison. **e-f)** Representative model traces of the total excitatory (G_E, upper panels) and inhibitory (G_I, lower panels) conductance in $L5B_{supp}$ (**e**) and $L5B_{enh}$ (**f**) pyramidal neurons during quiet wakefulness and movement. Green and black bars represent average excitatory and inhibitory conductance values, respectively. *Panels c-d: implementation of the fitting procedure was performed by Miha Pelko.*

reduction in effective input resistance ($\Delta R_{\text{eff}} = -3.3 \pm 2.4\,\text{M}\Omega$). Thus, by applying Eq. 2.16 and 2.17, our calculations suggest that L5B_{supp} cells received a small increase in inhibition ($\Delta G_E = -0.1$ nS, $\Delta G_I = 0.5$ nS, Fig. 4.14 **b**).

In contrast, L5B_{enh} cells displayed a significant depolarisation ($\Delta V_m = 4.4 \pm 0.5$ mV) and a small decrease in input resistance ($\Delta R_{\text{eff}} = -6.3 \pm 2.6$ MΩ). Thus, by applying Eq. 2.16 and 2.17 our calculations suggest that L5B_{enh} cells receive a large increase in excitatory conductance ($\Delta G_E \simeq 0.9$ nS and $\Delta G_I \simeq -0.1$ nS, Fig. 4.14 **b**).

The results of our model depend on G_L, but, unfortunately, we cannot measure it *in vivo* due to the high level of synaptic activity. Thus, as explained earlier, we took G_L from the existing literature. To test how the inferred $\langle G_E \rangle$ and $\langle G_I \rangle$ depend on the uncertainty we have on G_L, we ran a simple error study.

The distribution of the input resistance $R_L = 1/G_L$ across different cells typically displays a standard deviation of ∼20 MΩ (Sheets et al., 2011). Since we recorded ∼20 cells per group, the error on the estimation of the mean R_L is $\sim 20/\sqrt{20} = 5$ MΩ. If we estimate G_E and G_I by varying R_L by ± 5 MΩ, the results will differ by $< 5\%$. Even in the extreme case where $R_L = 160$ MΩ (∼20 MΩ change), our estimation of G_E and G_I only varied by $\sim 10 - 15\%$. We are therefore confident that our method, although not exact, gives a good ballpark estimate of the average excitatory and inhibitory conductances at the soma.

In the next section, I try to link the conductances and the voltage statistics as seen at the soma to the statistics of synaptic inputs. Again, I want to highlight the fact that the conductance at the soma might have little to do with the conductance in proximity of the synaptic sites. Therefore, although the next section is an interesting mathematical exercise and might suggest qualitative mechanisms, we cannot really trust the numbers.

4.3.4.2 *Estimation of $L5B_{enh}$ input statistics*

To explore more detailed features of L5B input structure (i.e. input size and rate, slow fluctuations in synaptic input, excitatory pairwise correlations), we exploited the analytically derived average input conductances to constrain the parameters of the simple single compartment passive neural model described in Chapter 2.

In brief, we assume excitatory and inhibitory synaptic inputs to be uncorrelated and Poissonian with log-normally distributed synaptic weights a_k having standard deviation σ_{a_X} equal to 1.2 times their mean value μ_{a_X}, where $X \in [Exc, Inh]$ (Song et al., 2005b). We set the synaptic time constants $\tau_E = 2$ ms and $\tau_I = 10$ ms (Häusser and Roth, 1997), and the average size of the excitatory synaptic conductance to be the same for excitation and inhibition $\mu_{a_E} = \mu_{a_I}$ (Berger et al., 2009; Silberberg and

Markram, 2007).

In Section 2.3 we derived the equation of the V_m power spectral density (Eq. 2.33), which depends on the rates (ν_E and ν_I), mean amplitudes (μ_{a_E} and μ_{a_I}) and time constants (τ_E and τ_I) of excitatory and inhibitory synaptic inputs. Since (i) the time constants are taken from literature, (ii) average input amplitudes are assumed to be equal for excitatory and inhibitory inputs, and (iii) input rates and amplitudes need to satisfy Eq. 2.15, the power-spectrum depends on one effective parameter only.

In order to generate a rough estimate of the amplitude and frequency during quiet wakefulness, we fit the power spectral density in the range $5-40$ Hz, deliberately avoiding the δ-band fluctuations (Fig. 4.14 **c-d**). This yields an average excitatory and inhibitory input size $\mu_{a_X} = 98$ nS (corresponding to ~ 0.18 mV EPSPs and ~ 0.1 mV IPSPs with *in vivo* like background input) and rates $\nu_E = 4760$ Hz, $\nu_I = 1030$ Hz.

Importantly, our estimated input rates are consistent with previously published empirical observations, in that L5B pyramidal neurons have on the order of $15,000 \pm 5,000$ synapses (Larkman, 1991), where $\sim 4/5$ are excitatory and $\sim 1/5$ are inhibitory (Abeles, 1991). If each presynaptic axon forms $4-8$ synapses with its postsynaptic target - mean of 5.5 (Ramaswamy et al., 2011) - then L5B neurons receive input from an estimated 2,200 excitatory and 550 inhibitory neurons. By assuming a presynaptic firing rate of 1-5 Hz, excitatory and inhibitory input rates should be $\sim 6,600$ Hz and $\sim 1,650$ Hz, respectively.

Next, we described the slow component of the power spectrum. Despite the complicated mathematical formulation, the key concept is that we explain the peak in the δ range of the power-spectrum (4.13 **b**) as a result of a fluctuating input rate in that frequency range. In practice, we add an inhomogeneous component to the Poisson processes:

$$\begin{aligned} \nu_E(t) =& \nu_E[1 + m_{E1}\cos(2\pi f_r t + \phi(t)) + m_{E2}\xi_E(t)], \\ \nu_I(t) =& \nu_I[1 + m_{I2}\xi_I(t)], \end{aligned} \tag{4.6}$$

where $f_r = 2.5$ Hz is the peak frequency of the slow fluctuations, m_{E1} represents the amplitude of the slow oscillatory component, m_{E2} and m_{I2} the amplitude of the non-stationary component, while $\phi(t)$ and $\xi(t)$ are Ornstein-Uhlenbeck processes with time constant $\tau_\phi = 0.1$ s and $\tau_\xi = 0.2$ s. We highlight that although m_{E1}, m_{E2} and m_{I2} affect the temporal structure of the inputs, they do not change the mean. Using single compartment simulations based on our model, we find the parameters m_{E1}, m_{E2} and m_{I2} which best fit the power sperctrum (Fig. 4.14 **c-d**, blue lines). With a least square

fit, we estimated $m_{E1} = 0.65$, $m_{E2} = 0.35$ and $m_{I2} = 0$.

We next investigate changes in the input structure during movement for the two sub-population ($L5B_{supp}$ and $L5B_{enh}$). We assumed that the weight distribution did not change with respect to quiet wakefulness and thus we tried to explain changes in the power spectrum by frequency changes alone.

Using the same procedure outlined above, we calculated the new rates to be $\nu_E =$ 4550 Hz, $\nu_I =$ 1230 Hz, for periods of movement in $L5B_{supp}$ cells. Next, we found that the best fit of the slow component of the power spectrum was performed by suppressing V_m fluctuations ($m_{E1} = 0$) in the δ band. This reproduced the power spectrum of $L5B_{supp}$ cells during movement (Fig. 4.14 **c, e**).

Finally, for the $L5B_{enh}$ cells, we calculated $\nu_E = 6520$ Hz and $\nu_I = 980$ Hz. However, changes in input frequency alone were not able to explain the elevated β-band power and to improve the power-spectrum fit, we introduced short timescale pairwise correlations (pairwise correlation coefficient = 0.005) between excitatory inputs - method described in (Hô and Destexhe, 2000). Fine timescale correlations described well the enhanced V_m β-power observed *in vivo* (Fig. 4.14 **d, f**). This simple explanation is consistent with recent studies showing clustered neuronal activity in M1 during behavior (Dombeck et al., 2009; Komiyama et al., 2010; Peters et al., 2014).

We emphasize that, although fine timescale correlations well describe the experimental data, they are one of many the possible explanations. For example, dendritic nonlinearities and neuromodulation may influence input amplitudes and could potentially explain equally well the increase in β-band power. However, our simple model would not be able to distinguish between these different hypotheses and thus we decided to present here only the simplest explanation.

4.3.5 *Frequency of compound large synaptic inputs increases in $L5B_{enh}$ neurons during movement*

To test our model's prediction that $L5B_{enh}$ neurons preferentially receive a net increase in excitatory input and pairwise correlations during movement, we developed an event detection algorithm to estimate the change in rate of subthreshold excitatory synaptic inputs during periods of quiet wakefulness and voluntary movement.

Due to the high frequency of afferent input, we were unable to isolate single excitatory postsynaptic potentials (EPSPs) - see also 3.1.3. However, we could reliably detect compound synaptic inputs ($\geq$ 1 mV) occurring in a time window (5 ms) shorter than

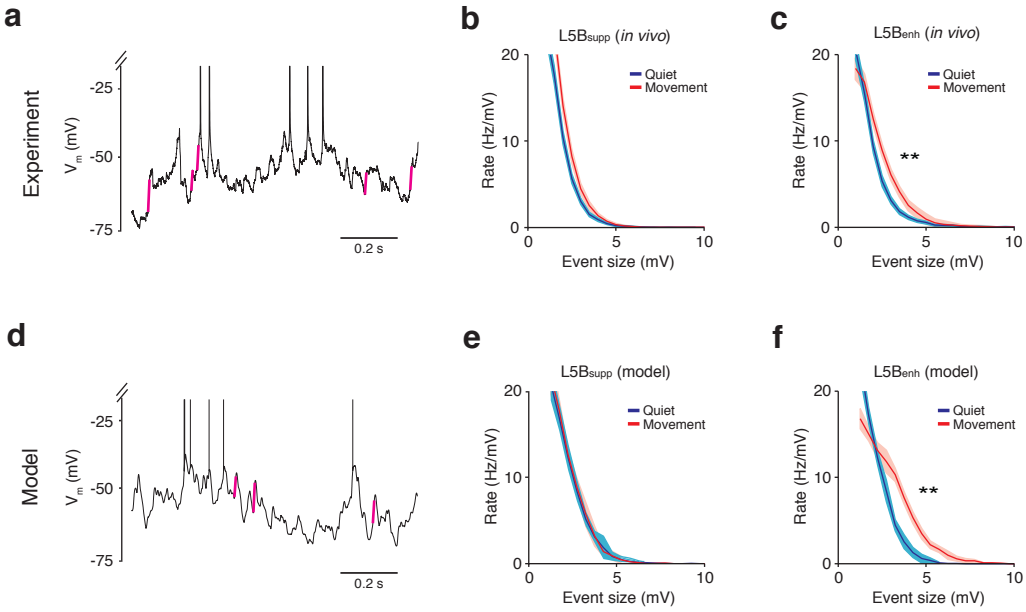

Figure 4.15: Increased excitatory drive in L5Benh neurons during movement. **a)** Representative voltage traces from an *in vivo* recording of a $L5B_{enh}$ pyramidal neuron. For display purposes only compound synaptic events with amplitudes > 4 mV and rise-times < 5ms are highlighted in magenta. **b-c)** Average rate density of compound synaptic events in $L5B_{supp}$ ($n = 17$) (**b**) and $L5B_{enh}$ ($n = 24$) (**c**) pyramidal neurons during quiet wakefulness (blue) and movement (red). **d-f** Same as **a-c**, but results from the model simulations. $^{**}p < 0.01$.

the average membrane time constant (8.2 ± 2.3 ms, $n = 10$) (Fig. 4.5 and 4.15 **a**). The detection threshold corresponded to twice the size of the average unitary synaptic response measured in L5 pyramidal neurons *in vitro* (Deuchars et al., 1994; Markram et al., 1997; Reyes and Sakmann, 1999). Events that occurred within ± 10 ms of a spike were discarded from the analysis.

Importantly, compound synaptic events may result from the combination of many individual EPSPs which arrive in the 5 ms time window. However, from the point of view of the neuron, these EPSPs are effectively coincident because the integration time is larger than the difference in their onset times.

During quiet wakefulness, we detected fast rising compound EPSPs (range $1 - 9.7$ mV) with similar rates in both $L5B_{supp}$ and $L5B_{enh}$ pyramidal neurons (Fig. 4.15 **b-c**), indicating both subpopulations of neurons receive a comparable level of excitatory drive and input correlations during quiet wakefulness. As predicted by model simulations and without further parameter tuning (Fig. 4.15 **d-f**), movement did not affect the rate of compound events in $L5B_{supp}$ neurons ($n = 17$) (Fig. 4.15 **b**). In contrast, $L5B_{enh}$ neurons displayed a significant increase in the rate of compound EPSPs

($n = 24$) (Fig. 4.15 **c**). Remarkably, we did not detect any compound events with amplitudes greater than 9.4 mV, even though neurons spent approximately 50% of the time > 10 mV from threshold.

Thus, $L5B_{enh}$ neurons appear to preferentially receive a net increase in excitatory drive during movement, which enhances the firing rate by depolarizing mean V_m and increasing input sensitivity.

4.4 DISCUSSION

The goal of the present study was to understand the mechanisms underpinning the movement-related changes in firing rate of L5B neurons in M1. We found that changing behavioral state – from quiet wakefulness to movement – bidirectionally modulated (i.e. enhanced or suppressed) M1 output via two opposing subthreshold mechanisms (Fig. 4.16): 1) a global decrease in network-driven, slow large-amplitude V_m fluctuations, which reduced V_m variability, input sensitivity and firing rates in $L5B_{supp}$ neurons; and 2) an increase in excitatory drive in a subpopulation of L5B neurons ($L5B_{enh}$), that increased input sensitivity and firing rates. Together, these findings illustrate the subthreshold mechanisms that regulate behavioral state-dependent modulation of M1 output.

4.4.1 *Functional classification of individual neurons*

We divided the neurons into three functional classes (enhanced, non-responding and suppressed), according to the changes in average firing rate between quiet wakefulness and movement. Only neurons that significantly change their firing rate ($p < 0.01$) belong to enhanced or suppressed groups, while 4 of them did not pass the significance test and were labelled as non-responding. Although the classes were defined using rigorous statistical tests (section 4.2.5), one might argue that actually the three classes are not *clusters*. For example, by inspecting figures 4.8 a,d and g, neurons do not appear to belong to three distinct clusters. In fact, attempts to find distinct clusters in the data failed, as shown in Figure 4.17.

Despite this result, in the context of this thesis, I decided to analyse the data using the statistically significant functional classification described in section 4.2.5. However, data might be analysed also in a totally different way, by considering the movement-related changes of firing rate as a continuum. We believe that a different data analysis would not affect the main conclusions of the study: global decrease of slow fluctuations vs. targeted increase of excitatory drive, which change the input-output transformation of the L5B neurons. Still, it would be an interesting exercise that might lead to different insights on the data.

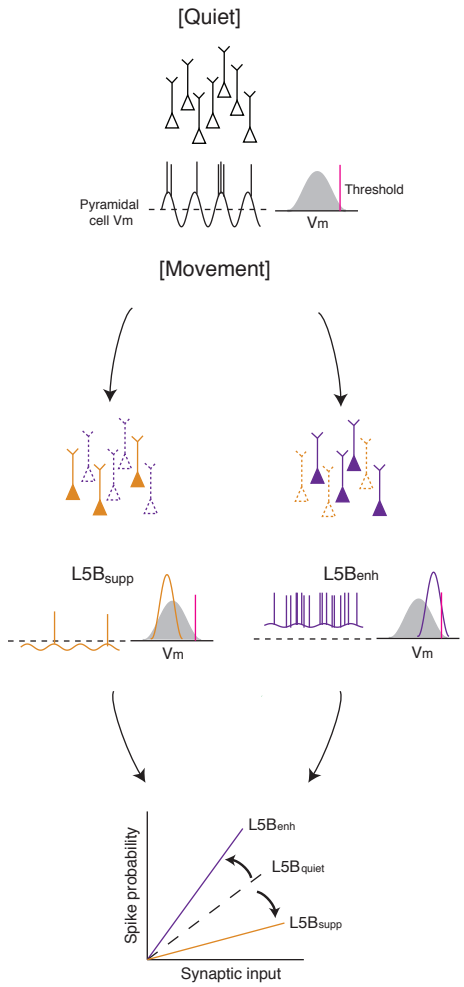

Figure 4.16: Summary of the cellular mechanisms underlying behavioral state-dependent modulation of motor cortex output. During periods of quiet wakefulness L5B pyramidal neurons display slow large amplitude V_m fluctuations, short distance to threshold and moderate ($\sim$ 5 Hz) firing rates. During movement, slow large-amplitude V_m fluctuations are suppressed in all L5B neurons, which reduced V_m variability, input sensitivity and overall firing rates. However, a subpopulation of L5B neurons concurrently experienced an increase in excitatory drive that depolarised mean V_m, increased input sensitivity and elevated firing rates.

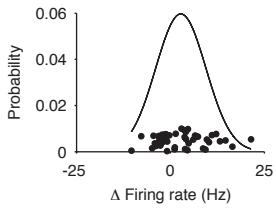

Figure 4.17: The functional subclasses defined in section 4.2.5 do not belong to separate clusters. Probability distribution of the difference of firing rate between quiet wakefulness (values of the individual neurons have been randomly scattered along the y-axis only to improve visualisation). We tried to find clusters using mixtures-of-Gaussians with increasing number of components. However, the best result according to the Bayesian Information Critrion (BIC, see section 1.2.4) was the one with one component, shown on the plot.

4.4.2 *Excitatory-inhibitory conductances in L5B pyramidal neurons*

Interpreting *in vivo* conductance measurements in large pyramidal neuron is problematic because, while the conductance is measured at the soma, synaptic inputs typically take place in the dendritic tree. Therefore, conductances in the soma might have little to do with the conductance experienced by the synaptic inputs (Williams and Mitchell, 2008). Neurons have been shown to have an axial resistance which act as a filter of the distal synaptic inputs and point-neuron models are in this respect an oversimplification. However, intuitively, if we measure a conductance increase in the soma, we can likely conclude that they are caused by a higher synaptic activity in the periphery of the neuron. Certainly, it wouldn't be a conclusive and unique interpretation. For example, it is possible that inputs that are closer to the soma have actually increased, while distal inputs have been dramatically reduced. While this scenario would indeed manifest as a net increase of the conductance measured in the soma, the actual number of inputs reaching the neuron might be indeed decreased. Other experiments (such as visualising the activity of all the synapses of the neuron) would be needed to validate this intuition. In the following discussion, I will assume that the conductance measured at the soma is a (qualitative) proxy of the synaptic inputs, but we must remember that there are also other possible interpretations.

Our conductance-based modeling suggests that $L5B_{supp}$ neurons received a moderate increase in local inhibitory input during movement – which in conjunction with decreased slow V_m fluctuations – reduced V_m variability, input sensitivity and firing rates. Although we did not directly investigate changes in inhibition, it is likely that fine scale modulation of local inhibitory input will be an important determinant of

L5B pyramidal neuron V_m during changes in behavioral state (Gentet et al., 2010; Haider et al., 2012).

At rest, excitatory and inhibitory conductances appeared to be balanced in mouse M1, with an estimated conductance ratio at the soma ($G_E/G_I = 0.9$) similar to that observed in visual cortex and parietal cortex of awake mice and cats, respectively (Haider et al., 2006, 2012; Rudolph-Lilith et al., 2007). However, while the conductances appear to be balanced, the currents (which in first approximations equal the conductance by the driving force of the synapses) are probably far from being balanced, due to the larger driving force for excitation.

Although the G_E/G_I ratio varies from neuron to neuron (Haider et al., 2006), on average it appears to be similar across species (Haider et al., 2006, 2012; Rudolph-Lilith et al., 2007). However, different species seem to have quite different levels of total synaptic conductance: rodents do not show the high conductance state typical of cat cortex (Haider et al., 2012). In mice, $G_E + G_I$ is about 2 times the leak conductance, as opposed to 5 times, which is the value typical for cats (Rudolph-Lilith et al., 2007). A lower conductance inevitably leads to longer integration time constants (see section 4.2.10) and less power to discriminate temporally close inputs (Destexhe et al., 2003). However, it is more energy efficient, because less synaptic inputs are required to maintain the background state. Moreover, in principle, it might bring more flexibility in terms of computation because the neuron will be more sensitive to transient changes in total conductance. In a situation of temporary high synaptic activity, the total conductance could reach high values for short periods time, which will alter the temporal integration mode of the neuron. Further investigation will be necessary to elucidate the functional and computational significance of the high or low conductance state across different species and brain regions.

4.4.3 *Estimation of synaptic inputs statistics in vivo*

To estimate the change in input statistics during movement we developed a simple single compartment passive neural model, which takes into account the first and second order statistics of the membrane potential.

First, we analytically derived $\langle G_E \rangle$ and $\langle G_I \rangle$ as seen at the soma by measuring the effective input resistance (R_{eff}) and the average membrane potential (μ_{V_m}). Previous reports have used similar approaches to measure the time-varying $G_E(t)$ and $G_I(t)$ by using either voltage-clamp recordings (Borg-Graham et al., 1996; Wehr and Zador, 2003) or current-clamp recordings with multiple baseline current injections

(Anderson et al., 2000). The method we developed here is more simple, as does not require voltage-clamp nor multiple current injections, but it captures only the average conductances and does not attempt time-varying inference.

As discussed in section 2.4, approximating a neuron as a single compartment is a crude simplification, as we know that dendritic processing is an important element for neuronal computation (London and Hausser, 2005). Thus, the conductances we obtain from the model refers to the net effect they have on the soma, after the dendritic processing.

As described in section 2.2, we rely on the estimation of R_{eff}, which we measure by (i) injecting current pulses, (ii) recording the voltage response and (iii) calculating the complex impedance as the ratio of the Fourier transforms of the voltage response and current pulse (Puil et al., 1986; Bao et al., 1992; Shin et al., 2008; Sheets et al., 2011). However, due to voltage-dependent properties of ion channels, impedance profiles are likely to be voltage-dependent. Although we did not investigate thoroughly this possibility, we showed that differences in R_{eff} between quiet wakefulness and movement, despite the V_m changes, are small (Fig. 4.12). Thus, we believe that our estimation of R_{eff} is robust and can be safely used to estimate average conductances at the soma, although we are aware of the fact that, due to the axial resistance, we cannot conclude anything on the magnitude of the conductances in the synaptic sites.

Secondly, we used a combination of analytical calculations and computational simulations to generate a rough estimate of the frequency and size of the excitatory and inhibitory synaptic inputs. Our method relies on fitting the power spectrum of the membrane potential, which captures the dynamics of the V_m fluctuations. Other computational studies have used second order statistics to describe synaptic inputs (Kuhn et al., 2004; Moreno-Bote et al., 2008), but we are not aware of other attempts to use the power-spectrum to estimate synaptic input statistics *in vivo*, where low-frequency fluctuations play a dominant role.

The method proposed here relies on a set of strong assumptions: (i) trains of synaptic inputs are not correlated, (ii) spiking activity does not perturb the subthreshold behaviour. We now discuss these assumptions.

Experimental and theoretical works show that correlations between excitatory neurons on a short time scale ($\sim 1-5$ms) are small *in vivo*, normally < 0.03 (Smith and Kohn, 2008; Helias et al., 2014; Grytskyy et al., 2013; Renart et al., 2010; Ecker et al., 2010). However, excitatory and inhibitory neurons are correlated in such a way that inhibition tracks (or follows) excitation (Okun and Lampl, 2008; Renart et al., 2010; Haider et al., 2012; Tetzlaff et al., 2012). Since our calculations do not take this into account, the contribution of the cross-correlation term in the power spectrum (Eq.

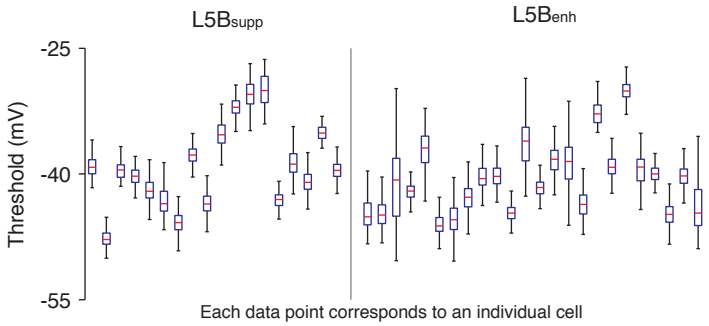

Figure 4.18: Wide range of threshold values within and across L5B pyramidal neurons. Each data point on the x axis represents a single neuron. The bars represent the full range of the threshold values, the boxes the 25^{th} and 75^{th} percentiles, while the red lines the median value.

2.30) was ignored. We argue that this will likely lead to a small underestimation of input frequencies.

In vivo, the spiking mechanism of a cell provides a natural limit to constrain the V_m: when a critical value is reached (spike threshold), sodium channels open triggering a spike. In our analysis, we removed spikes in order to get rid of the contamination due to active currents. However, this procedure biased our measurments towards lower μ_{V_m} and σ_{V_m}, because we truncated voltage trajectories which otherwise would have reached more depolarised values.

Moreover, the bias is not uniform across neurons, because neurons which sit closer to threshold (and have a higher firing rate) will be penalised more. We argue, that this effect in general leads to an underestimation of the excitatory conductance, in particular for $L5B_{enh}$ neurons during movement, which display the highest firing rates. Interestingly, the spike threshold is not a fixed value, and depends on the specific trajectory of the membrane potential during the approach to the critical value (Platkiewicz and Brette, 2010, 2011). Thus, *in vivo*, the threshold of a single neuron displays a wide range of values (Fig. 4.18). An extension to the current framework would be required to quantify the effect of spiking activity on our estimation. Crucially, the model will need to correctly describe the variable threshold and the after-spike currents which modulate the passive properties of the membrane potential (Mensi et al., 2011).

Although we believe that the results presented here represent a reasonable estimation of the input statistics, we feel that the analysis would benefit from rigorous formulation and validation in a probabilistic framework, similar to the one proposed in chapter 3. As discussed in section 3.1.5, a range of different probabilistic techniques

promise an estimation of $G_E(t)$ and $G_I(t)$ (Kobayashi et al., 2011; Paninski et al., 2012; Lankarany et al., 2013). In the future, it would be interesting to compare our simple method to these advanced (but computationally expensive) algorithms.

4.4.4 *Slow V_m fluctuations in M1 projection neurons*

The presence of rhythmic δ-band oscillations in the local field potential and subthreshold membrane potential of cortical neurons has long been associated with general anesthesia (Steriade et al., 1993b) and slow wave sleep (Steriade et al., 1993a, 2001). However, recent intracellular recordings from L2/3 neurons in mouse visual and somatosensory cortices have shown slow V_m fluctuations in excitatory and inhibitory neurons during quiet waking (Crochet and Petersen, 2006; Poulet and Petersen, 2008; Gentet et al., 2010; Haider et al., 2012; Okun et al., 2010). Similarly, our findings demonstrate that slow membrane potential fluctuations also occur in deep layers of M1 during periods of inactivity. Interestingly, periods of high V_m δ-band power during quiet wakefulness were intermittent suggesting discontinuous levels of arousal or awareness (Harris and Thiele, 2011). The function of cortical slow oscillations in rodents remains unclear. One hypothesis is that they represent an evolutionary conserved rhythmic mode that amplifies relevant inputs by enforcing oscillatory entrainment to different input streams (Schroeder and Lakatos, 2009; Knyazev, 2012). However, further investigations will be required to determine whether internal or external input streams can influence slow V_m fluctuations during quiet wakefulness and the importance of this for resting-state behavior in mice. In chapter 5 I will further discuss on this topic.

4.4.5 *Possible sources of increased excitatory inputs to $L5B_{enh}$ neurons during movement*

Our study shows that during movement a subpopulation of L5B neurons receives an increase excitation, which depolarises V_m and enhances input sensitivity and firing rate. To better understand the cellular and circuit mechanisms that regulate output during motor behaviour, it is important to locate the source of the increase excitation. L5B neurons in M1 receive input from a variety of brain areas (e.g. M1 L2/3 neurons, secondary motor cortex and motor thalamus, see Fig. 1.2, adapted from Hooks et al. (2013)): in principle, any combination of these inputs could be the source of the increased excitation we observed.

Previous studies have shown that L2/3 pyramidal neurons in M1, which provide a strong descending input to L5B (Kaneko et al., 1994; Weiler et al., 2008), display clustered activity during head-restrained locomotion in mice (Dombeck et al., 2009; Komiyama et al., 2010; Huber et al., 2012). However, preliminary data generated in the Duguid Lab suggest that L2/3 is unlikely the main source of excitation to L5B neurons during self-paced voluntary movement on a treadmill (Fig. 4.19 **a-c**), because movement-related firing rate changes appear to be rather small. The reasons for the discrepancy between these preliminary observations and previous studies are not clear and deserve further investigation. Possible explanations are (i) different experimental set-up, treadmill vs. rotating air-cushioned ball, and (ii) under-sampling problems of the patch-clamp recordings, where only 8 neurons were analysed.

Another possible source of excitation is from the motor thalamus, which directly targets L5B neurons (Castro-Alamancos, 2002b, 2004b; Constantinople and Bruno, 2013; Hooks et al., 2013) and shows increased activity during movement (Armstrong and Drew, 1984; Beloozerova et al., 2003; Poulet et al., 2012). Importantly, motor thalamic input to L5B is not projection class-specific (Hooks et al., 2013), which is in line with our observation that $L5B_{enh}$ neurons contained both PT- and IT-type neurons. Thalamic activation of supra- and infra-granular neurons in primary somatosensory cortex (S1) has been shown to promote cortical desynchronization and direct depolarization of pyramidal neurons (Constantinople and Bruno, 2013; Poulet et al., 2012), suggesting thalamus could mediate some of the V_m changes observed in L5B neurons in M1 during movement. Preliminary data generated in the Duguid Lab by pharmacologically blocking the motor thalamus, suggest that thalamic inputs are necessary in order to maintain V_m close to threshold, which results in a moderate basal firing rate (Fig. 4.19 **d**). However, despite thalamic inactivation, during movement the membrane potential still shows a net depolarisation, suggesting that thalamic inputs are not responsible for the enhanced excitation in $L5B_{enh}$ neurons during movement. If confirmed by further experiments, this finding would be in contrast with a recent report by Poulet et al. (2012), which shows that thalamic inactivation is responsible for a strong hyper-polarisation of V_m in L2/3 neurons in S1 during whisking. Possibly, thalamic inputs play a different role in regulating the dynamics of sensory vs. motor cortices.

Alternatively, neuromodulation has been shown to play an important role in cortical processing during behavior. In L2/3 pyramidal neurons in mouse primary visual cortex (V1), locomotion-dependent V_m depolarization appears to be regulated by the interplay between cholinergic disinhibition (Fu et al., 2014), enhanced glutamatergic input and noradrenergic neuromodulation (Polack et al., 2013). We did not directly

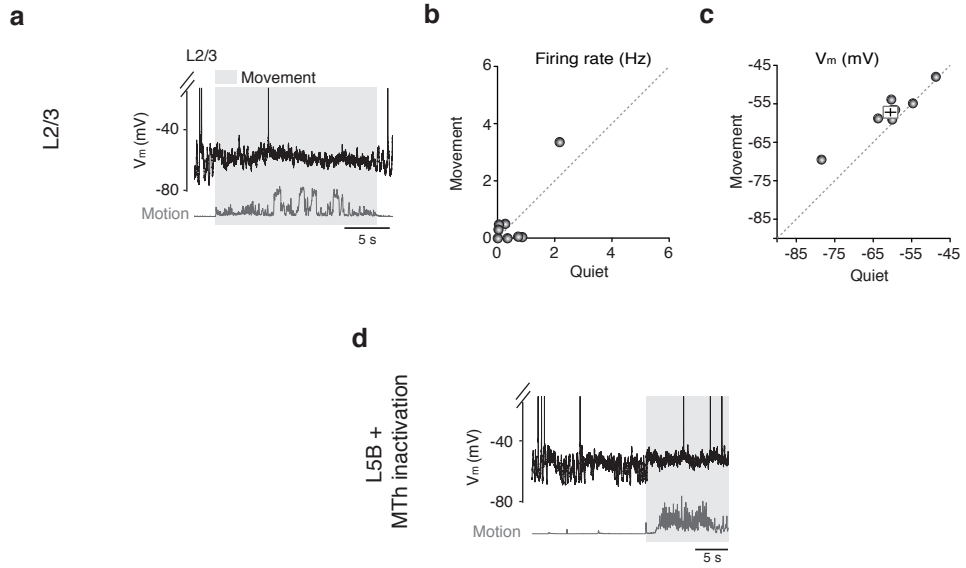

Figure 4.19: Possible sources of the increase in excitation to $L5B_{enh}$ neurons during movement. **a-c)** Activity of L2/3 neurons in M1, which is a local source of input to L5B: **(a)** representative voltage trace; **(b)** firing rate and **(c)** average V_m for individual L2/3 neurons recorded (grey circles, $n = 8$). **d)** Membrane potential of a L5B neuron following thalamic inactivation.
*Recording in panel **d** performed by Joshua Dacre.*

test the role of neuromodulation in this study[1], but the similarity in magnitude of V_m depolarization in M1 and V1 during locomotion suggests that one or more neuromodulators could play a role in sculpting M1 V_m dynamics. However, unlike V1, we only observed movement related V_m depolarization in a subset of L5B cells suggesting targeted, cell-selective effects which might not be easily accounted for by neuromodulation only. Thus, to explain why only a subset of neurons in L5B show increased excitation during movement, we may need to take into account also specific connectivity patterns in the network structure, which we next discuss.

1 In a follow up of this work, Julia Schiemann investigated the role of noradrenaline on L2/3 and L5B pyramidal neurons in M1. She found that in presence of noradrenergic blockers $L5B_{enh}$ neurons do not show the movement-related depolarisation we observed during control conditions. Thus, noradrenaline is required by $L5B_{enh}$ neurons to depolarise during movement. Her findings, together with the results presented in this chapter, are part of a manuscript which is currently under review in *Neuron*. However, I decided not to include her results in this thesis because I was not involved neither in the design nor in the execution of her experiments. I only analysed her data and I would not feel comfortable including these potentially high impact findings in the framework of my thesis.

4.4.6 *Could network activity underlie the movement-related bidirectional changes we measured?*

This study characterised the sub-threshold and spiking activity of different sub-populations of neurons in deep layers of M1. Although whole-cell recordings measure activity of single neurons, V_m fluctuations reflect the activity of the whole network (Long and Lee, 2012). With our extensive data analysis and modeling, we tried to capture the behaviour of the network from the V_m statistics in single neurons. Here we further speculate about possible network mechanisms underlying our experimental findings.

Many computational and theoretical studies show that, in a randomly connected recurrent neural network, spontaneous fluctuations in the activity of excitatory and inhibitory populations accurately track each other (Moreno-Bote et al., 2008; Renart et al., 2010). The negative feedback given by inhibitory microcircuits generates negative correlations in synaptic currents which cancel the effect of shared input (Tetzlaff et al., 2012). This leads to an asynchronous state, with very low correlations between neurons.

However, neurons are not randomly connected in the cortex: the presence of clustered sub-networks is supported by anatomical (Song et al., 2005b; Perin et al., 2011) and functional (Yassin et al., 2010) studies also in M1 (Anderson et al., 2010; Kiritani et al., 2012; Shepherd, 2013; Dombeck et al., 2009; Komiyama et al., 2010; Huber et al., 2012).

A recent report investigated the dynamics in a network of neurons with clustered connectivity (Litwin-Kumar and Doiron, 2012). The authors found that the activity within a cluster exhibited a complicated pattern of transitions between low and high activity states, which is also typical of our recordings (Fig. 4.6 **c-d**, 4.10 **a**, 4.13 **a**). In their model, inhibition is global, rather than local, therefore all clusters (active and non-active) experience the same amount of negative feedback. Interestingly, this leads to a higher degree of correlations among neurons belonging to the same cluster, due to the incomplete action of the inhibitory feedback. Correlations increase with firing rate (Rocha et al., 2007) and we suspect that they will increase even more in neurons within the same cluster. More correlations lead to a higher chance of having multiple synaptic inputs in a short time window, which is consistent with the increased frequency of compound synaptic inputs in $L5B_{enh}$ neurons during movement (Fig. 4.15).

Why would some of the neurons in M1 consistently decrease their firing rate during movement? Possibly, they belong to clusters which are more rarely activated by

long-range inputs and during movement receive a higher inhibition from neighbouring active clusters. However, we cannot exclude that this pool of neurons is needed for different behavioural tasks (e.g. goal directed movements) or for learning, in the same fashion as different clusters activate in L2/3 (Dombeck et al., 2009; Huber et al., 2012).

Another intriguing possibility is that actually $L5B_{supp}$ and $L5B_{enh}$ neurons are not fixed subpopulations, but dynamically switch over long periods of time. As shown by Litwin-Kumar and Doiron (2012), the transition time between active and inactive clusters of neurons depends on the specific network connectivity and can be very large. This hypothesis could be tested by monitoring the activity of multiple neurons for a long period of time.

4.4.7 *What did we learn?*

The results described in this chapter span about three years of work during my PhD (2010-2013) and started as a first-pass exploratory study of the intracellular activity of the neurons in the motor cortex. Four years ago, little was known about sub-threshold features of pyramidal neurons in an awake brain. The pioneering work by Crochet and Petersen (2006) and Poulet and Petersen (2008) were the first reports showing how brain-state changes affected the membrane potential dynamics in superficial layers of the sensory cortex. My idea, was to perform the same study in M1 and understand how changes in subthreshold dynamics could affect input-output transformations of motor-cortical neurons. Parallel to my study, the field witnessed a number of exceptional reports describing in detail mechanisms regulating V_m dynamics in different behavioural-states and brain areas. These reports focused on the superficial layers of visual (Polack et al., 2013; Haider et al., 2012) and somato-sensory (Avermann et al., 2012; Poulet et al., 2012) cortices and analysed the effects of (i) inhibition, (ii) thalamic inputs and (iii) neuromodulation on intracellular activity. However, no previous work investigated the mechanisms driving changes of activity in the deep layers of the motor cortex.

Our study shows that in the motor cortex during active behaviour the network activity displays a global desynchronisation which reflects in the spectral component of the power spectrum of V_m of individual neurons. This finding suggests that changes in brain state are global across the cortex and that, in this respect, the subthreshold features of neurons in M1 are not different from those in V1 and S1. More interestingly, we show for the first time that this global network effect produces in L5B neurons the same subthreshold changes monitored in L2/3 neurons (reduced power in the δ-frequency band). This observation suggests that all neurons in the whole cor-

tex (sensory and motor areas, deep and superficial layers) may experience the same underlying rhythm. Unfortunately, to fully prove this statement, we should perform simultaneous intracellular recordings from neurons in different cortical areas, which would be technically very challenging. In chapter 5 I will elaborate further on a possible explanation of the cortical-wide nature of the subthreshold rhythms.

For the first time, we quantified the effect of subthreshold dynamics on input-output transformation of neurons in an awake brain. Firstly, we showed that variations in total conductance between quiet wakefulness and movement are small and do not affect the integrative properties of the neurons. This is quite interesting, as conductance changes have been indicated by theoretical studies as possible candidates to regulate the response of the neurons (Hô and Destexhe, 2000; Chance et al., 2002; Cardin et al., 2008). Secondly, input-output curves theoretically have a sigmoidal shape and respond to changes in membrane mean and variance with shifts and slope changes respectively. However, we showed that, due to the limited range of input size observed *in vivo*, changes in mean and variance have qualitatively similar effect on the input-output curves we measured. Since the membrane potential of L5B neurons sits relatively close to threshold, subtle changes in input statistics (both mean and variance) have dramatic effects on spike probability.

We also observed that a sub-population of neurons ($L5B_{enh}$) increase the sensitivity to small inputs during movement. One could ask whether this increased sensitivity is a consequence or a cause of the increased firing rate. An increased firing rate will enhance the excitation in the recurrent network, which in turns will depolarise the neurons and increase their sensitivity to small inputs. This would be a circular argument with no easy solution. This type of problem is peculiar when trying to interpret observations in a complex system displaying recurrent positive feedback (Arthur, 2013). I think that it will be highly beneficial to set up network simulations (which naturally incorporate feedback loops) replicating the experimental findings described here. For example, it would be interesting to study which (i) connectivity profiles, (ii) external input patterns and (iii) neuromodulatory effects are compatible with the measured movement-related changes in sub-threshold and supra-threshold activity.

We also highlight that our findings refer to voluntary self-paced movements. It will be of great interest to investigate what happens when the animal is engaged in specific motor tasks. Possibly, goal-oriented motor behaviours will display different features, due to the effect of specific neuromodulatory mechanisms (Marder et al., 2014).

We have described how our work relates to similar studies in other cortical areas and the possible impact it has on understanding cortical processing. However, one could ask whether this work helps our knowledge on how motor cortex is involved in movement control. At the moment, the answer is likely to be negative. While intracellular recordings elucidate cellular mechanisms, to understand the role of M1 as a whole, recordings from large populations of neurons would be the preferred choice. We mentioned in chapter 1 that M1 maps the highly dimensional motor space into a smaller number of dimensions by exploiting muscle synergies, which are muscle coactivation patterns (Overduin et al., 2012). Single cell recordings cannot possibly offer any insight on that. However, the global and cellular mechanisms we described could be used to constrain simulations of biologically plausible neural network which reproduce population-level features. At the moment, we can only speculate that changes in spike output and input sensitivity we observed generate motor commands, which, integrated with ongoing rhythmic spinal cord signals, adjust and maintain locomotor function (Armstrong and Drew, 1984; Beloozerova et al., 2003; Ueno and Yamashita, 2011). The path to link low-level features to high-level computational functions is long and steep, but I hope this work goes in the right direction.

5

CONCLUSION

In this thesis, by using whole-cell recordings and probabilistic models, I have studied input-output transformations in single neurons of awake mice. Here I summarise the main contributions in each chapter.

In Chapter 2 I presented a set of calculations which link synaptic input to the membrane potential statistics of a simple passive point-neuron model. This work extends previous reports by including an analytical description of the power spectrum of the membrane potential, which was a crucial element in the models developed in the other chapters.

In Chapter 3 I introduced a probabilistic model developed to infer input frequency and synaptic weight distribution using *in vivo* voltage clamp data. In principle this method can be applied to any good quality *in vivo* voltage-clamp recording, but here, due to the difficulty to acquire good quality data of large cortical pyramidal neurons, I applied it on molecular layer cerebellar interneurons of awake mice. I showed that this model outperforms current methods commonly used in experimental laboratories, which are time consuming and provide incorrect results. I found that effective synaptic weight distributions have long tails, which means that most of the synapses are small, while a few of them are particularly strong. This finding is consistent with the idea that networks have preferential information pathways (few strong synapses) sitting on the top of a background activity (supported by many weak synapses). In contrast to the findings obtained using traditional analysis methods, our model shows that during movement, the excitatory inputs to cerebellar interneurons increase in frequency without affecting the weight distribution.

Finally, in Chapter 4 I investigated the mechanisms responsible for changes in firing rate and input-output transformations of pyramidal neurons in the deep layers of the primary motor cortex. In this study, we acquired whole-cell recordings in the motor cortex of awake behaving mice and implemented a simple model which describes some of the features observed in the experimental data. We found that two subpopulation of neurons differentially change their firing rate and input sensitivity during movement, due to two concurrent effects: a global desynchronisation of the network (a brain-state switch), and a targeted increase in excitatory inputs to a subset of the neurons. Interestingly, output neurons in motor cortex display the

same network-driven movement-related reduction in membrane potential slow fluctuations previously found in superficial layers of sensory cortices. This is compatible with the idea that the entire cortex experiences the same underlying rhythm during behaviour (below I will further discuss this concept). In contrast to L2/3 neurons, which seem to display a rather uniform behaviour in M1, a subset of L5B neurons presents a sustained depolarisation on the top of the reduction in slow fluctuations.

The topics and results I presented in this thesis represent just a small contribution in understanding brain function, but hopefully my work will generate a few ideas that will lead to a more comprehensive understanding. Here I discuss two of the (many) outstanding questions that the thesis has raised.

5.1 BIDIRECTIONAL CHANGES IN M1: DRIVING OR DRIVEN BY MOVEMENT?

One outstanding question is whether the observed changes we see in the motor cortex are a consequence or a cause of the movements. Unfortunately, due to the complex nature of the brain[1] and the limitations of our approach, this question does not have a simple answer. I discuss separately the two main findings of chapter 4, namely (i) the desynchronisation of the network activity and (ii) the bidirectional changes in firing rate and input sensitivity.

The desyncronisation of the network activity is probably due to a transition from a *passive* to an *active* brain state (Harris and Thiele, 2011). As we have shown in Fig. 4.13 **c**, desynchronisation can also take place also during quiet wakefulness, and we interpreted this as transient attentional shifts. However, during movement, the brain state should always be active, leading to desynchronised cortical activity. This means that desynchronisation, if associated with a change towards an active brain state, is likely to take place before the movement and is not a mere consequence of locomotion (Churchland et al., 2006b, 2010).

However, it is more difficult to know the causal relationship between movement and the bidirectional changes in firing rate and input sensitivity. While it is established that M1 activation can trigger and shape movements (Fig. 4.2), it is also recognised that movements provide the brain with sensory and proprioceptive feedback, which in turn are reported back to M1 (Evarts and Fromm, 1977; Pavlides et al., 1993; Bhanpuri et al., 2013; Hooks et al., 2013). As discussed in section 1.1.2, the primary

1 Complexity science is a movement that studies how interacting elements in a system create overall patterns and how these patterns in turn cause the interacting elements to change or adapt (Arthur, 2013). According to this definition, the brain is certainly a complex system.

motor cortex is not the only brain area projecting directly to the spinal cord (Lemon, 2008). Moreover, spontaneous locomotor activity is generated by central pattern generators in the spinal cord (Forssberg and Grillner, 1973; Goulding, 2009). Thus, it is not surprising that lesions in M1 do not suppress locomotion (Ueno and Yamashita, 2011), but alter the fine movement of the paws.

In our experimental set-up we cannot determine whether the features we observed in M1 during movement are the source of or are a consequence of the movement itself. Nevertheless, we can state that these features (i) characterise movement periods and (ii) provide inputs to the spinal cord which regulate specific features of locomotion (Armstrong and Drew, 1984; Beloozerova et al., 2003; Ueno and Yamashita, 2011). As we said, the brain is a complex system, where the interactions of individual elements (neurons) create overall patterns (e.g. brain state changes, movement) which in turn imply adaptations of the interacting elements. In this view, it is perhaps naive to raise the question *what causes what?*, because in a complex system, due to cyclic feedback loops, it is hard to isolate cause and consequence.

To solve this chicken-egg problem, we need to carefully plan the experiment in order to obtain millisecond precision when comparing the onset of the movement and the activity of pyramidal neurons in M1. In fact, while high frequency cameras can capture movements, they cannot detect early muscle contractions. Thus, it will be necessary to use more invasive monitoring techniques, like subcutaneous electromyographic recordings (EMG), which will significantly increase the already high technical hurdle of the experiment[2].

Another possibility would be to perform experiments with a specific behavioural task, where the mouse has to execute repetitive well defined movements (e.g. button press or lever push/pull). By averaging across a number of repetitions, it might be possible to correlate the timing of movement with the neural activity and disentangle sensory feedback from motor commands.

5.2 ORIGIN OF THE SLOW FLUCTUATIONS

We briefly discussed in section 1.1.4 the mechanisms responsible for the switching of the cortical state from a synchronised state, rich in slow frequency fluctuations of

2 The onset detection in EMG signals is a tricky problem, which could be a subject of a thesis by itself. EMGs show non-stationary noise in overlapping frequency bands with the signal, which make the onset of a change very difficult to detect (Staude et al., 2001). In my view, lots can be learned from seismology, which has a long research tradition in detecting the exact onset time of earthquakes (Küperkoch et al., 2010; Kitagawa et al., 2001). The problem it faces is mathematically very similar to detecting movement onsets in EMG signals. A range of techniques have been employed: wavelet packet decomposition (Dai-Zhi et al., 2005), fractal-dimension methods (Sabbione and Velis, 2010), information-theory based analysis (Akram and Eaton, 2012).

population activity, to a desynchronised state. However, the functional reason why the cortex dynamically switches between these two states during wakefulness is not known. In particular, while the advantages of a desynchronised state are clear - reduced internal variability leading to improved signal-to-noise ratio (Arieli et al., 1996; Churchland et al., 2006b, 2010)-, only few hypotheses try to explain the benefit of a state rich in slow-fluctuations. One possibility is that it represents a default cortical state with low energy demands (Harris and Thiele, 2011), the other is that slow fluctuations, if entrained to external sensory stimuli, might improve signal detection in sensory perception (Lakatos et al., 2008, 2009; Schroeder and Lakatos, 2009). The latter hypothesis being true, we need to understand what sensory stimulation, if any, could entrain the cortex to slow rhythms.

The studies of Lakatos and colleagues in primate sensory cortices (auditory and visual) show that if attended, cross-modal sensory inputs can coordinate the timing of slow oscillations in primary sensory cortex (Lakatos et al., 2008, 2009; Calderone et al., 2014). In fact, they introduced the concept of a *leading* sensory modality, which can be chosen by shifting the attention. If stimuli occur with a rhythmic and predictable structure in an attended, master modality, ongoing slow oscillations in the entire cortex will entrain to this rhythm. Because periods of cortical excitability will be aligned with the occurrence of events in the master modality, processing secondary modalities will be efficiently lead by the master.

A recent report shows that LFP oscillations in the barrel cortex of awake mice are entrained to the respiratory rhythm (Ito et al., 2014). Moreover, we noticed that mice breathing frequency (~ 3 Hz) is in the range of the δ oscillations observed in M1 during quiet wakefulness. Since mice are likely to attend to olfactory input during quiet wakefulness (Shusterman et al., 2011; Kleinfeld et al., 2014), we hypothesise that slow intracellular oscillations in the primary motor cortex of awake, behaving mice are entrained to olfactory input during quiet wakefulness. If this hypothesis is correct, it would mean that when mice select olfaction as their leading sense, M1 would be ready to react to inputs coming from pre-motor areas (and possibly generate movement) right on the onset of a potentially interesting olfactory stimulus. To test this hypothesis, it would be really interesting to study the relationship between the phase of the breathing cycle and the cortical fluctuations we recorded in M1.

Preliminary data, based on a prototype experiment we performed ($n = 1$ recording), do indeed fit with our above hypothesis[3]. Using the same set-up described in chapter 4 (head-restrined awake mouse free to walk on a treadmill), we acquired a

3 Experiment performed by P. Puggioni, electronic board and thermistors to monitor the breathing rate designed and build by D.M. Ross, data analysis designed by P. Puggioni and implemented by D.M. Ross.

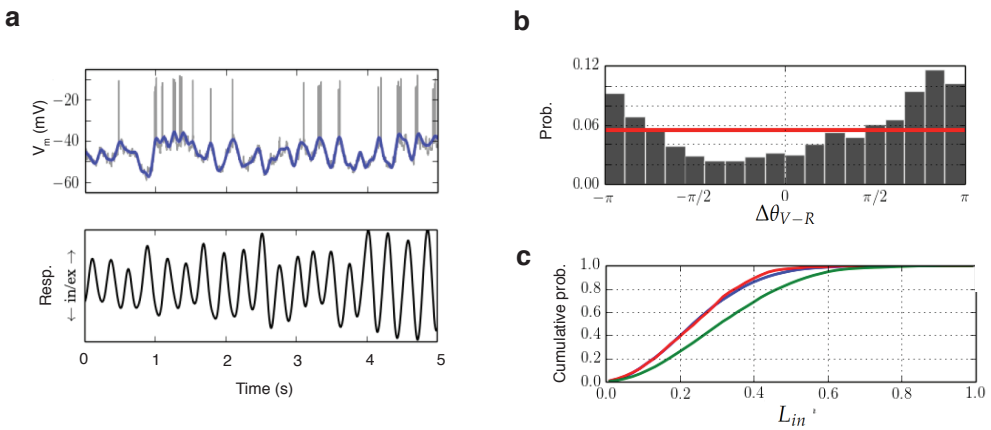

Figure 5.1: Slow subthreshold oscillations in M1 are entrained to respiratory rhythm during quiet wakefulness but not during movement. **a)** (Top) Voltage trace of a pyramidal neuron in M1 (gray line) with extracted δ band membrane potential oscillations and (bottom) associated respiratory recording (in: inhalation, ex: exhalation). **b)** Probability distribution for the instantaneous phase difference between the respiratory and whole-cell patch clamp recordings (dark grey; red line shows uniform distribution). **c)** Cumulative probability distributions of the phase-lock index L_{in} for quiet wakefulness (green), movement (red) and control (blue). KS test, p<0.01 for quite wakefulness vs. control.
Figure adapted from 'Respiratory entrainment of delta-theta (< 8 Hz) oscillations in the primary motor cortex of awake, behaving mice', BSc thesis by D.M. Ross. (University of Edinburgh, 2014)

whole-cell M1 L5B pyramidal neuron recording while simultaneously monitoring the breathing rate using a fast thermistor (Ito et al., 2014) (Fig. 5.1 **a**). In brief, the instantaneous phase of the V_m and breathing were obtained by applying wavelet transforms (Torrence and Compo, 1998) and extracting the phases relative to the frequency displaying the highest power in the respiratory signal. The probability distribution of the phase difference $\Delta\theta_{V-R}$ between V_m and the respiratory trace differs from a uniform distribution (Fig. 5.1 **b**). The phase lock index

$$L_{in} = 1/N\sqrt{(\Sigma_{i=1}^{N}\cos\Delta\theta_{V-R}^{i})^2 + (\Sigma_{i=1}^{N}\sin\Delta\theta_{V-R}^{i})^2}, \tag{5.1}$$

calculated using 4 second sliding windows, measures how tightly locked the two signals are (0: unlocked, 1: perfectly locked) (Ashida and Wagner, 2010). During quite wakefulness, the probability distribution of L_{in} is significantly different from control[4] (Fig. 5.1 **c**, green and blue lines respectively). Interestingly, during movement (red line) the phase-locking was indistinguishable from control.

4 For the control, we calculated the L_{in} of breathing signal and V_m belonging to different recordings

These exciting preliminary results suggest that in quiescent mice, there is a hierarchy of sensory modelities. The master modality may default to olfaction, while during movement, their attention likely switches to other sensory-motor inputs which do not show a characteristic rhythm - the continuous-mode described by Schroeder and Lakatos (2009).

An alternative explanation is that fluctuations in M1 are involved in driving the rhythmic thoracic movements required for inhalation/exhalation. However, we believe that this simple explanation is unlikely to be true for three reasons: (i) the respiratory cycle is believed to be under the control of brainstem nuclei (Feldman and Negro, 2006; Garcia et al., 2011; Smith et al., 2013); (ii) we recorded from the forelimb region of M1, an area that is unlikely linked to driving respiratory movements; (iii) this explanation does not account for the suppression of slow fluctuations in M1 during movement, which arguably is the period during which respiratory regulation becomes more important.

It will be valuable to perform other sets of experiments to better understand to what extent this hierarchical organisation ultimately affects behavioral (motor) responses. In particular, it will be interesting to suddenly present bright visual stimuli at random time intervals. If our conjecture is correct, a sudden visual stimulation should shift the attention of the mouse from olfaction to vision and disrupt the ongoing oscillation in M1 even in absence of movement. In addition, it will be interesting to measure the reaction time of the mouse in response to stimuli (for example a loud noise) which are in phase or not with the respiration. We expect that movements generated by external stimuli will have shorter latency when they are synchronous to the peak of the membrane potential during slow fluctuations, thus showing that intracellular fluctuations in M1 have a behavioural significance. Studies performed in monkeys showed that the neural variability which characterises the quiet state is quenched before the onset of the movement (Churchland et al., 2006a,b, 2010). The authors conclude that the suppression of fluctuations of neural activity is fundamental to reduce neural variability and enhance the signal to noise of motor command transmission. However, if experiments will confirm our hypothesis, they would be in contrast with this interpretation. Fluctuations of neural activity before movement onset would not just be *noise*. They would reflect the attentional state of the individual and, in some circumstances, they would be beneficial to prompt quick motor responses.

5.3 CONCLUSION

The experimental work presented in this thesis has been a pioneering exploratory analysis and has produced a ground truth data-set of intracellular recordings in the primary motor cortex of awake mice. It was complemented by a novel probabilistic inference technique which will help in extracting all possible information from the data. Due to its exploratory nature, in the framework of the thesis I focused on the descriptive level, elucidating the intracellular features which underlie changes of firing activity related to behaviour.

Following the discussion of exciting preliminary data in section 5.2, the next step will be to build on our descriptive findings and get to better understand M1 and cortical function. Clearly, further investigation is needed to confirm and extend the results of this preliminary study. The set of future experiments I described offer a unique opportunity to find a thread linking attention to intracellular mechanisms and behaviour. This would represent a significant step towards demonstrating that the brain does not operate with static *always on* brain modules. In contrast, it can *decide* which area is in command and the activity of other areas becomes enslaved to the master. It is without doubt that an attentional shift can rapidly change hierarchies and redefine the flow of information.

Maybe, after all, this orchestra has a conductor (Singer, 2008).

BIBLIOGRAPHY

Abeles, M. (1991). *Corticonics: Neural Circuits of the Cerebral Cortex*. (Cited on page 86.)

Akram, J. and Eaton, D. (2012). Adaptive microseismic event detection and automatic time picking. *AAPG Datapages/Search and Discovery*, pages 1–5. (Cited on page 105.)

Alonso-Nanclares, L., Gonzalez-Soriano, J., Rodriguez, J. R., and DeFelipe, J. (2008). Gender differences in human cortical synaptic density. *Proc Natl Acad Sci USA*, 105(38):14615–9. (Cited on page 1.)

Anderson, C. T., Sheets. . . , P. L., Kiritani, T., and Shepherd, G. M. G. (2010). Sublayer-specific microcircuits of corticospinal and corticostriatal neurons in motor cortex. *Nat Neurosci*, 13(6):739–44. (Cited on pages 4, 73, and 99.)

Anderson, J. S., Carandini, M., and Ferster, D. (2000). Orientation tuning of input conductance, excitation, and inhibition in cat primary visual cortex. *J Neurophysiol*, 84(2):909–26. (Cited on pages 20, 34, and 94.)

Arieli, A., Sterkin, A., Grinvald, A., and Aertsen, A. (1996). Dynamics of ongoing activity: explanation of the large variability in evoked cortical responses. *science*, 273(5283):1868–71. (Cited on pages 1, 9, and 106.)

Arlotta, P., Molyneaux, B. J., Chen, J., Inoue, J., Kominami, R., and Macklis, J. D. (2005). Neuronal subtype-specific genes that control corticospinal motor neuron development in vivo. *Neuron*, 45(2):207–21. (Cited on page 68.)

Armstrong, D. M. and Drew, T. (1984). Discharges of pyramidal tract and other motor cortical neurones during locomotion in the cat. *J Physiol (Lond)*, 346:471–95. (Cited on pages 59, 60, 97, 102, and 105.)

Arthur, W. (2013). Complexity economics: a different framework for economic thought. *Complexity Economics, Oxford University Press (forthcoming)*. (Cited on pages 101 and 104.)

Ashida, G. and Wagner, H. (2010). Processing of phase-locked spikes and periodic signals. *Analysis of parallel spike trains*. (Cited on page 107.)

Avermann, M., Tomm, C., Mateo, C., Gerstner, W., and Petersen, C. C. H. (2012). Microcircuits of excitatory and inhibitory neurons in layer 2/3 of mouse barrel cortex. *J Neurophysiol*. (Cited on page 100.)

Ayaz, A. and Chance, F. S. (2009). Gain modulation of neuronal responses by subtractive and divisive mechanisms of inhibition. *J Neurophysiol*, 101(2):958–68. (Cited on pages 1 and 10.)

Azevedo, F. A. C., Carvalho, L. R. B., Grinberg, L. T., Farfel, J. M., Ferretti, R. E. L., Leite, R. E. P., Filho, W. J., Lent, R., and Herculano-Houzel, S. (2009). Equal numbers of neuronal and nonneuronal cells make the human brain an isometrically scaled-up primate brain. *J. Comp. Neurol.*, 513(5):532–41. (Cited on page 1.)

Bao, J. Z., Davis, C. C., and Schmukler, R. E. (1992). Frequency domain impedance measurements of erythrocytes. constant phase angle impedance characteristics and

a phase transition. *Biophysical Journal*, 61(5):1427–34. (Cited on page 94.)

Barber, D. (2012). *Bayesian reasoning and machine learning*. (Cited on pages 12 and 14.)

Barbour, B., Brunel, N., Hakim, V., and Nadal, J.-P. (2007). What can we learn from synaptic weight distributions? *Trends Neurosci*, 30(12):622–9. (Cited on pages 35 and 56.)

Beloozerova, I. N., Sirota, M. G., and Swadlow, H. A. (2003). Activity of different classes of neurons of the motor cortex during locomotion. *J Neurosci*, 23(3):1087–97. (Cited on pages 59, 60, 75, 97, 102, and 105.)

Bendat, J. and Piersol, A. (1966). *Measurement and analysis of random data*. (Cited on page 36.)

Bennett, C., Arroyo, S., and Hestrin, S. (2013). Subthreshold mechanisms underlying state-dependent modulation of visual responses. *Neuron*, 80(2):350–7. (Cited on pages 1 and 62.)

Berger, T. K., Perin, R., Silberberg, G., and Markram, H. (2009). Frequency-dependent disynaptic inhibition in the pyramidal network: a ubiquitous pathway in the developing rat neocortex. *J Physiol (Lond)*, 587(Pt 22):5411–25. (Cited on page 85.)

Beugen, B. J. V., Gao, Z., Boele, H.-J., Hoebeek, F., and Zeeuw, C. I. D. (2013). High frequency burst firing of granule cells ensures transmission at the parallel fiber to purkinje cell synapse at the cost of temporal coding. *Front. Neural Circuits*, 7:95. (Cited on page 57.)

Bhanpuri, N. H., Okamura, A. M., and Bastian, A. J. (2013). Predictive modeling by the cerebellum improves proprioception. *J Neurosci*, 33(36):14301–6. (Cited on page 104.)

Bialek, W., Rieke, F., van Steveninck, R., and Warland, D. (1999). Spikes: Exploring the neural code (computational neuroscience). *The MIT Press*. (Cited on page 17.)

Bishop, C. (2007). Pattern recognition and machine learning (information science and statistics). *Springer*. (Cited on pages 12, 14, and 15.)

Borg-Graham, L. J., Monier, C., and Frégnac, Y. (1996). Voltage-clamp measurement of visually-evoked conductances with whole-cell patch recordings in primary visual cortex. *J Physiol Paris*, 90(3-4):185–8. (Cited on pages 34 and 93.)

Brazier, M. (1963). The history of the electrical activity of the brain as a method for localizing sensory function. *Med Hist*, 7:199–211. (Cited on page 6.)

Brette, R. and Destexhe, A. (2012). Intracellular recording. *Handbook of Neural Activity Measurement*. (Cited on page 27.)

Brozović, M., Abbott, L. F., and Andersen, R. A. (2008). Mechanism of gain modulation at single neuron and network levels. *J Comput Neurosci*, 25(1):158–68. (Cited on page 61.)

Buchanan, K. A., Blackman, A. V., Moreau, A. W., Elgar, D., Costa, R. P., Lalanne, T., Jones, A. A. T., Oyrer, J., and Sjöström, P. J. (2012). Target-specific expression of presynaptic nmda receptors in neocortical microcircuits. *Neuron*, 75(3):451–66. (Cited on page 67.)

Buzsáki, G., Bickford, R. G., Ponomareff, G., Thal, L. J., Mandel, R., and Gage, F. H. (1988). Nucleus basalis and thalamic control of neocortical activity in the freely moving rat. *J Neurosci*, 8(11):4007–26. (Cited on page 8.)

Buzsáki, G. and Mizuseki, K. (2014). The log-dynamic brain: how skewed distributions affect network operations. *Nat Rev Neurosci*, 15(4):264–78. (Cited on pages 35 and 56.)

Cajal, S. (1899). *Comparative study of the sensory areas of the human cortex*. (Cited on page 3.)

Calderone, D., Lakatos, P., Butler, P., and Castellanos, F. (2014). Entrainment of neural oscillations as a modifiable substrate of attention. *Trends in Cognitive Sciences*, 18(6):300–309. (Cited on page 106.)

Carandini, M., Heeger, D. J., and Movshon, J. A. (1997). Linearity and normalization in simple cells of the macaque primary visual cortex. *J Neurosci*, 17(21):8621–44. (Cited on page 1.)

Cardin, J. A., Palmer, L. A., and Contreras, D. (2008). Cellular mechanisms underlying stimulus-dependent gain modulation in primary visual cortex neurons in vivo. *Neuron*, 59(1):150–60. (Cited on pages 61, 79, and 101.)

Casella, G. (1985). An introduction to empirical bayes data analysis. *The American Statistician*, 39(2):83–87. (Cited on page 41.)

Castro-Alamancos, M. A. (2002a). Different temporal processing of sensory inputs in the rat thalamus during quiescent and information processing states in vivo. *J Physiol (Lond)*, 539(Pt 2):567–78. (Cited on page 1.)

Castro-Alamancos, M. A. (2002b). Different temporal processing of sensory inputs in the rat thalamus during quiescent and information processing states in vivo. *The Journal of Physiology*, 539(Pt 2):567–78. (Cited on page 97.)

Castro-Alamancos, M. A. (2004a). Absence of rapid sensory adaptation in neocortex during information processing states. *Neuron*, 41(3):455–64. (Cited on page 60.)

Castro-Alamancos, M. A. (2004b). Dynamics of sensory thalamocortical synaptic networks during information processing states. *Prog Neurobiol*, 74(4):213–247. (Cited on page 97.)

Chalk, M., Herrero, J. L., Gieselmann, M. A., Delicato, L. S., Gotthardt, S., and Thiele, A. (2010). Attention reduces stimulus-driven gamma frequency oscillations and spike field coherence in v1. *Neuron*, 66(1):114–25. (Cited on page 8.)

Chance, F. S., Abbott, L. F., and Reyes, A. D. (2002). Gain modulation from background synaptic input. *Neuron*, 35(4):773–82. (Cited on pages 1, 10, 61, 62, 79, and 101.)

Chorev, E., Epsztein, J., Houweling, A. R., Lee, A. K., and Brecht, M. (2009). Electrophysiological recordings from behaving animals–going beyond spikes. *Curr Opin Neurobiol*, 19(5):513–9. (Cited on pages 6, 7, and 26.)

Churchland, M. M., Afshar, A., and Shenoy, K. V. (2006a). A central source of movement variability. *Neuron*, 52(6):1085–96. (Cited on page 108.)

Churchland, M. M., Yu, B. M., Cunningham, J. P., Sugrue, L. P., Cohen, M. R., Corrado, G. S., Newsome, W. T., Clark, A. M., Hosseini, P., Scott, B. B., Bradley, D. C., Smith, M. A., Kohn, A., Movshon, J. A., Armstrong, K. M., Moore, T., Chang, S. W., Snyder, L. H., Lisberger, S. G., Priebe, N. J., Finn, I. M., Ferster, D., Ryu, S. I., Santhanam, G., Sahani, M., and Shenoy, K. V. (2010). Stimulus onset quenches neural variability: a widespread cortical phenomenon. *Nat Neurosci*, 13(3):369–78. (Cited on pages 9, 104, 106, and 108.)

Churchland, M. M., Yu, B. M., Ryu, S. I., Santhanam, G., and Shenoy, K. V. (2006b). Neural variability in premotor cortex provides a signature of motor preparation. *J Neurosci*, 26(14):3697–712. (Cited on pages 8, 9, 73, 104, 106, and 108.)

Cohen, M. R. and Kohn, A. (2011). Measuring and interpreting neuronal correlations. *Nat Neurosci*, 14(7):811–9. (Cited on page 57.)

Constantinople, C. M. and Bruno, R. M. (2011). Effects and mechanisms of wakefulness on local cortical networks. *Neuron*, 69(6):1061–8. (Cited on pages 9, 10, and 60.)

Constantinople, C. M. and Bruno, R. M. (2013). Deep cortical layers are activated directly by thalamus. *science*, 340(6140):1591–4. (Cited on pages 3 and 97.)

Costa, R. M., Cohen, D., and Nicolelis, M. A. L. (2004). Differential corticostriatal plasticity during fast and slow motor skill learning in mice. *Curr Biol*, 14(13):1124–34. (Cited on pages 60 and 75.)

Cowan, R. and Wilson, C. (1994). Spontaneous firing patterns and axonal projections of single corticostriatal neurons in the rat medial agranular cortex. *Journal of Neurophysiology*, 71(1):17–32. (Cited on page 60.)

Crochet, S. and Petersen, C. C. H. (2006). Correlating whisker behavior with membrane potential in barrel cortex of awake mice. *Nat Neurosci*, 9(5):608–10. (Cited on pages 8, 60, 64, 73, 96, and 100.)

Dai-Zhi, L., Ren-Ming, W., Xi-Hai, L., and Zhi-Gang, L. (2005). Onset point identification of single-channel seismic signal based on wavelet packet decomposition and ar model. *CHINESE JOURNAL OF GEOPHYSICS*, 48(5):1170–1175. (Cited on page 105.)

Davidson-Pilon, C. (2014). Probabilistic programming and bayesian methods for hackers. *https://github.com/CamDavidsonPilon/Probabilistic-Programming-and-Bayesian-Methods-for-Hackers*. (Cited on page 16.)

Dean, P., Porrill, J., Ekerot, C.-F., and Jörntell, H. (2010). The cerebellar microcircuit as an adaptive filter: experimental and computational evidence. *Nat Rev Neurosci*, 11(1):30–43. (Cited on page 57.)

Destexhe, A. and Contreras, D. (2006). Neuronal computations with stochastic network states. *Science*, 314(5796):85–90. (Cited on page 60.)

Destexhe, A. and Paré, D. (1999). Impact of network activity on the integrative properties of neocortical pyramidal neurons in vivo. *J Neurophysiol*, 81(4):1531–47. (Cited on page 71.)

Destexhe, A., Rudolph-Lilith, M., and Paré, D. (2003). The high-conductance state of neocortical neurons in vivo. *Nat Rev Neurosci*, 4(9):739–51. (Cited on pages 11, 19, 60, 70, 77, and 93.)

Deuchars, J., West, D. C., and Thomson, A. M. (1994). Relationships between morphology and physiology of pyramid-pyramid single axon connections in rat neocortex in vitro. *J Physiol (Lond)*, 478 Pt 3:423–35. (Cited on page 88.)

Dombeck, D. A., Graziano, M. S. A., and Tank, D. W. (2009). Functional clustering of neurons in motor cortex determined by cellular resolution imaging in awake behaving mice. *J Neurosci*, 29(44):13751–60. (Cited on pages 5, 63, 65, 87, 97, 99, and 100.)

Douglas, R. J. and Martin, K. A. C. (2004). Neuronal circuits of the neocortex. *Annu. Rev. Neurosci.*, 27:419–51. (Cited on page 3.)

Drew, T., Jiang, W., and Widajewicz, W. (2002). Contributions of the motor cortex to the control of the hindlimbs during locomotion in the cat. *Brain Research Reviews*, 40(1–3):178–191. (Cited on page 59.)

Drew, T., Prentice, S., and Schepens, B. (2004). Cortical and brainstem control of locomotion. *Progress in Brain Research*, Volume 143:251–261. (Cited on page 59.)

Dumoulin, V. and Thouin, F. (2014). A ballistic monte carlo approximation of pi. *arXiv*, physics.pop-ph. (Cited on page 14.)

Ecker, A. S., Berens, P., Keliris, G. A., Bethge, M., Logothetis, N. K., and Tolias, A. S. (2010). Decorrelated neuronal firing in cortical microcircuits. *Science*, 327(5965):584–7. (Cited on pages 57 and 94.)

Evarts, E. and Fromm, C. (1977). Sensory responses in motor cortex neurons during precise motor control. *Neuroscience Letters*, 5(5):267–272. (Cited on page 104.)

Feldman, J. L. and Negro, C. A. D. (2006). Looking for inspiration: new perspectives on respiratory rhythm. *Nat Rev Neurosci*, 7(3):232–42. (Cited on page 108.)

Forssberg, H. and Grillner, S. (1973). The locomotion of the acute spinal cat injected with clonidine i.v. *Brain Research*, 50(1):184–186. (Cited on pages 59 and 105.)

Fries, P., Reynolds, J. H., Rorie, A. E., and Desimone, R. (2001). Modulation of oscillatory neuronal synchronization by selective visual attention. *science*, 291(5508):1560–3. (Cited on page 8.)

Fu, Y., Tucciarone, J. M., Espinosa, J. S., Sheng, N., Darcy, D. P., Nicoll, R. A., Huang, Z. J., and Stryker, M. P. (2014). A cortical circuit for gain control by behavioral state. *Cell*, 156(6):1139–1152. doi: 10.1016/j.cell.2014.01.050. (Cited on pages 62 and 97.)

Garcia, A. J., Zanella, S., Koch, H., Doi, A., and Ramirez, J.-M. (2011). Chapter 3– networks within networks: the neuronal control of breathing. *Prog Brain Res*, 188:31–50. (Cited on page 108.)

Gentet, L. J., Avermann, M., Matyas, F., Staiger, J. F., and Petersen, C. C. H. (2010). Membrane potential dynamics of gabaergic neurons in the barrel cortex of behaving mice. *Neuron*, 65(3):422–35. (Cited on pages 6, 66, 71, 93, and 96.)

Gerstner, W. and Kistler, W. (2002). *Spiking neuron models: Single neurons, populations, plasticity*. (Cited on pages 17, 21, and 83.)

Gerstner, W. and Naud, R. (2009). How good are neuron models? *science*, 326(5951):379–380. (Cited on page 17.)

Gordon, G. R. J. and Bains, J. S. (2005). Noradrenaline triggers multivesicular release at glutamatergic synapses in the hypothalamus. *J Neurosci*, 25(49):11385–95. (Cited on page 30.)

Goulding, M. (2009). Circuits controlling vertebrate locomotion: moving in a new direction. *Nat Rev Neurosci*, 10(7):507–518. 10.1038/nrn2608. (Cited on pages 59 and 105.)

Graziano, M. S. A. and Aflalo, T. N. (2007a). Mapping behavioral repertoire onto the cortex. *Neuron*, 56(2):239–51. (Cited on page 59.)

Graziano, M. S. A. and Aflalo, T. N. (2007b). Rethinking cortical organization: moving away from discrete areas arranged in hierarchies. *Neuroscientist*, 13(2):138–47.

(Cited on page 59.)

Graziano, M. S. A., Taylor, C. S. R., Moore, T., and Cooke, D. F. (2002). The cortical control of movement revisited. *Neuron*, 36(3):349–62. (Cited on pages 1 and 3.)

Grytskyy, D., Tetzlaff, T., Diesmann, M., and Helias, M. (2013). A unified view on weakly correlated recurrent networks. *Front. Comput. Neurosci.*, 7:131. (Cited on pages 57 and 94.)

Haider, B., Duque, A., Hasenstaub, A. R., and McCormick, D. A. (2006). Neocortical network activity in vivo is generated through a dynamic balance of excitation and inhibition. *Journal of Neuroscience*, 26(17):4535–45. (Cited on pages 28 and 93.)

Haider, B., Hausser, M., and Carandini, M. (2012). Inhibition dominates sensory responses in the awake cortex. *Nature*. (Cited on pages 19, 28, 60, 71, 83, 93, 94, 96, and 100.)

Haider, B. and McCormick, D. A. (2009). Rapid neocortical dynamics: cellular and network mechanisms. *Neuron*, 62(2):171–89. (Cited on pages 60, 61, and 77.)

Harris, K. D. and Thiele, A. (2011). Cortical state and attention. *Nat Rev Neurosci*. (Cited on pages 1, 8, 9, 71, 73, 81, 96, 104, and 106.)

Häusser, M. and Roth, A. (1997). Estimating the time course of the excitatory synaptic conductance in neocortical pyramidal cells using a novel voltage jump method. *J Neurosci*, 17(20):7606–25. (Cited on page 85.)

Häusser, M., Spruston, N., and Stuart, G. J. (2000). Diversity and dynamics of dendritic signaling. *science*, 290(5492):739–44. (Cited on page 24.)

Helias, M., Tetzlaff, T., and Diesmann, M. (2014). The correlation structure of local neuronal networks intrinsically results from recurrent dynamics. *PLoS Comput Biol*, 10(1):e1003428. (Cited on pages 57 and 94.)

Helmchen, F., Svoboda, K., Denk, W., and Tank, D. W. (1999). In vivo dendritic calcium dynamics in deep-layer cortical pyramidal neurons. *Nature Neuroscience*, 2(11):989–96. (Cited on page 24.)

Henze, D. A. and Buzsáki, G. (2001). Action potential threshold of hippocampal pyramidal cells in vivo is increased by recent spiking activity. *Neuroscience*, 105(1):121–30. (Cited on page 66.)

Hines, M. L. and Carnevale, N. T. (1997). The neuron simulation environment. *Neural Comput*, 9(6):1179–209. (Cited on page 24.)

Hô, N. and Destexhe, A. (2000). Synaptic background activity enhances the responsiveness of neocortical pyramidal neurons. *J Neurophysiol*, 84(3):1488–96. (Cited on pages 11, 61, 62, 79, 87, and 101.)

Hooks, B. M., Mao, T., Gutnisky, D. A., Yamawaki, N., Svoboda, K., and Shepherd, G. M. G. (2013). Organization of cortical and thalamic input to pyramidal neurons in mouse motor cortex. *J Neurosci*, 33(2):748–60. (Cited on pages 4, 5, 67, 96, 97, and 104.)

Horrace, W. (2013). Moments of the truncated normal distribution. *J Prod Anal*, pages 1–6. (Cited on page 37.)

hua Liu, B., Li, P., Sun, Y. J., tang Li, Y., Zhang, L. I., and Tao, H. W. (2010a). Intervening inhibition underlies simple-cell receptive field structure in visual cortex. *Nat Neurosci*, 13(1):89–96. (Cited on page 28.)

hua Liu, B., Li, P., Sun, Y. J., tang Li, Y., Zhang, L. I., and Tao, H. W. (2010b). Intervening inhibition underlies simple-cell receptive field structure in visual cortex. *Nat Neurosci*, 13(1):89–96. (Cited on page 28.)

Huber, D., Gutnisky, D. A., Peron, S., O'Connor, D. H., Wiegert, J. S., Tian, L., Oertner, T. G., Looger, L. L., and Svoboda, K. (2012). Multiple dynamic representations in the motor cortex during sensorimotor learning. *Nature*, 484(7395):473–8. (Cited on pages 5, 97, 99, and 100.)

Hyland, B. (1998). Neural activity related to reaching and grasping in rostral and caudal regions of rat motor cortex. *Behav Brain Res*, 94(2):255–69. (Cited on page 5.)

Ikegaya, Y., Sasaki, T., Ishikawa, D., Honma, N., Tao, K., Takahashi, N., Minamisawa, G., Ujita, S., and Matsuki, N. (2013). Interpyramid spike transmission stabilizes the sparseness of recurrent network activity. *Cerebral Cortex*, 23(2):293–304. (Cited on page 56.)

Isomura, Y., Harukuni, R., Takekawa, T., Aizawa, H., and Fukai, T. (2009). Microcircuitry coordination of cortical motor information in self-initiation of voluntary movements. *Nature Neuroscience*, 12(12):1586–93. (Cited on pages 4, 5, and 59.)

Ito, J., Roy, S., Liu, Y., Cao, Y., Fletcher, M., Lu, L., Boughter, J., Grün, S., and Heck, D. (2014). Whisker barrel cortex delta oscillations and gamma power in the awake mouse are linked to respiration. *Nature Communications*, 5. (Cited on pages 106 and 107.)

Jelitai, M. (2014). Private communucation. (Cited on page 30.)

Joseph, R. (1996). *Neuropsychiatry, Neuropsychology, and Clinical Neuroscience: Emotion, Evolution, Cognition, Language, Memory, Brain Damage, and Abnormal Behavior*. (Cited on page 3.)

Kandel, E., Schwartz, J., and Jessell, T. (2000). Principles of neural science. 4. (Cited on pages 2, 3, and 4.)

Kaneko, T., Caria, M., and Asanuma, H. (1994). Information processing within the motor cortex. ii. intracortical connections between neurons receiving somatosensory cortical input and motor output neurons of the cortex. *J. Comp. Neurol.*, 345(2):172–184. (Cited on page 97.)

Keller, G. B., Bonhoeffer, T., and Hübener, M. (2012). Sensorimotor mismatch signals in primary visual cortex of the behaving mouse. *Neuron*, 74(5):809–815. (Cited on page 62.)

Kiritani, T., Wickersham, I. R., Seung, H. S., and Shepherd, G. M. G. (2012). Hierarchical connectivity and connection-specific dynamics in the corticospinal-corticostriatal microcircuit in mouse motor cortex. *Journal of Neuroscience*, 32(14):4992–5001. (Cited on pages 2 and 99.)

Kitagawa, G., Takanami, T., and Matsumoto, N. (2001). Signal extraction problems in seismology*. *International statistical review*, 69(1):129–152. (Cited on page 105.)

Kleinfeld, D., Deschênes, M., Wang, F., and Moore, J. D. (2014). More than a rhythm of life: breathing as a binder of orofacial sensation. *Nat Neurosci*, 17(5):647–51. (Cited on page 106.)

Knyazev, G. (2012). Eeg delta oscillations as a correlate of basic homeostatic and motivational processes. *Neuroscience & Biobehavioral Reviews*, 36(1):677–695. (Cited on page 96.)

Kobayashi, R., Shinomoto, S., and Lansky, P. (2011). Estimation of time-dependent input from neuronal membrane potential. *Neural Comput*, 23(12):3070–93. (Cited on pages 34, 40, 58, and 96.)

Koch, C. (1999). Biophysics of computation. *Oxford University Press*. (Cited on pages 1, 17, and 21.)

Koch, C. (2004). Biophysics of computation: information processing in single neurons. (Cited on page 2.)

Komiyama, T., Sato, T. R., O'Connor, D. H., Zhang, Y.-X., Huber, D., Hooks, B. M., Gabitto, M., and Svoboda, K. (2010). Learning-related fine-scale specificity imaged in motor cortex circuits of behaving mice. *Nature*, 464(7292):1182–6. (Cited on pages 5, 87, 97, and 99.)

Koulakov, A. A., Hromádka, T., and Zador, A. M. (2009). Correlated connectivity and the distribution of firing rates in the neocortex. *J Neurosci*, 29(12):3685–94. (Cited on page 56.)

Kuhn, A., Aertsen, A., and Rotter, S. (2004). Neuronal integration of synaptic input in the fluctuation-driven regime. *Journal of Neuroscience*, 24(10):2345–56. (Cited on page 94.)

Küperkoch, L., Meier, T., and Diehl, T. (2010). Automated event and phase identification. *Lithospheric Deformation Turning Observations Into Models*, page 89. (Cited on page 105.)

Lakatos, P., Karmos, G., Mehta, A. D., Ulbert, I., and Schroeder, C. E. (2008). Entrainment of neuronal oscillations as a mechanism of attentional selection. *Science*, 320(5872):110–3. (Cited on pages 9 and 106.)

Lakatos, P., O'Connell, M. N., Barczak, A., Mills, A., Javitt, D. C., and Schroeder, C. E. (2009). The leading sense: supramodal control of neurophysiological context by attention. *Neuron*, 64(3):419–30. (Cited on pages 1, 9, and 106.)

Lankarany, M., Zhu, W.-P., Swamy, M. N. S., and Toyoizumi, T. (2013). Inferring trial-to-trial excitatory and inhibitory synaptic inputs from membrane potential using gaussian mixture kalman filtering. *Front. Comput. Neurosci.*, 7:109. (Cited on pages 34, 40, 58, and 96.)

Larkman, A. U. (1991). Dendritic morphology of pyramidal neurones of the visual cortex of the rat: Iii. spine distributions. *J. Comp. Neurol.*, 306(2):332–43. (Cited on page 86.)

Laubach, M., Wessberg, J., and Nicolelis, M. A. (2000). Cortical ensemble activity increasingly predicts behaviour outcomes during learning of a motor task. *Nature*, 405(6786):567–71. (Cited on page 5.)

Lee, A. K., Manns, I. D., Sakmann, B., and Brecht, M. (2006). Whole-cell recordings in freely moving rats. *Neuron*, 51(4):399–407. (Cited on page 7.)

Lee, D., Lin, B.-J., and Lee, A. K. (2012). Hippocampal place fields emerge upon single-cell manipulation of excitability during behavior. *Science*, 337(6096):849–53. (Cited on page 7.)

Lefort, S., Tomm, C., Sarria, J.-C. F., and Petersen, C. C. H. (2009). The excitatory neuronal network of the c2 barrel column in mouse primary somatosensory cortex. *Neuron*, 61(2):301–16. (Cited on pages 2, 6, and 7.)

Lemon, R. N. (2008). Descending pathways in motor control. *Annu Rev Neurosci*, 31:195–218. (Cited on pages 5, 59, and 105.)

Lemon, R. N. (2010). What drives corticospinal output? *F1000 Biol Rep*, 2:51. (Cited on pages 1, 3, and 59.)

Lemon, R. N. and Griffiths, J. (2005). Comparing the function of the corticospinal system in different species: organizational differences for motor specialization? *Muscle Nerve*, 32(3):261–79. (Cited on page 5.)

Lickiss, T., Cheung, A. F. P., Hutchinson, C. E., Taylor, J. S. H., and Molnár, Z. (2012). Examining the relationship between early axon growth and transcription factor expression in the developing cerebral cortex. *Journal of Anatomy*, 220(3):201–211. (Cited on page 68.)

Lindner, B. (2006). Superposition of many independent spike trains is generally not a poisson process. *Physical Review E*, 73(2):022901. (Cited on pages 21 and 32.)

Litwin-Kumar, A. and Doiron, B. (2012). Slow dynamics and high variability in balanced cortical networks with clustered connections. *Nat Neurosci*, 15(11):1498–505. (Cited on pages 99 and 100.)

London, M. and Hausser, M. (2005). Dendritic computation. *Annu. Rev. Neurosci.*, 28:503–32. (Cited on pages 24 and 94.)

Long, M. A. and Lee, A. K. (2012). Intracellular recording in behaving animals. *Curr Opin Neurobiol*, 22(1):34–44. (Cited on pages 6, 26, and 99.)

Manabe, T., Renner, P., and Nicoll, R. (1992). Postsynaptic contribution to long-term potentiation revealed by the analysis of miniature synaptic currents. *Nature*, 355(6355):50–55. 10.1038/355050a0. (Cited on page 56.)

Mao, T., Kusefoglu, D., Hooks, B. M., Huber, D., Petreanu, L., and Svoboda, K. (2011). Long-range neuronal circuits underlying the interaction between sensory and motor cortex. *Neuron*, 72(1):111–23. (Cited on page 4.)

Marder, E., O'Leary, T., and Shruti, S. (2014). Neuromodulation of circuits with variable parameters: Single neurons and small circuits reveal principles of state-dependent and robust neuromodulation. *Annu. Rev. Neurosci.*, 37(1):329–346. doi: 10.1146/annurev-neuro-071013-013958. (Cited on page 101.)

Margrie, T. W., Brecht, M., and Sakmann, B. (2002). In vivo, low-resistance, whole-cell recordings from neurons in the anaesthetized and awake mammalian brain. *Pflugers Arch*, 444(4):491–8. (Cited on page 6.)

Markram, H., Lübke, J., Frotscher, M., and Sakmann, B. (1997). Regulation of synaptic efficacy by coincidence of postsynaptic aps and epsps. *science*, 275(5297):213–5. (Cited on page 88.)

Marmont, G. (1949). Studies on the axon membrane; a new method. *J Cell Physiol*, 34(3):351–82. (Cited on page 26.)

McCormick, D. A. (1989). Cholinergic and noradrenergic modulation of thalamocortical processing. *Trends Neurosci*, 12(6):215–21. (Cited on page 10.)

McCormick, D. A. and Bal, T. (1997). Sleep and arousal: thalamocortical mechanisms. *Annu. Rev. Neurosci.*, 20:185–215. (Cited on page 9.)

McCormick, D. A., Wang, Z., and Huguenard, J. (1993). Neurotransmitter control of neocortical neuronal activity and excitability. *Cereb Cortex*, 3(5):387–98. (Cited on

page 1.)

Mensi, S., Naud, R., Pozzorini, C., Avermann, M., Petersen, C. C. H., and Gerstner, W. (2011). Parameter extraction and classification of three cortical neuron types reveals two distinct adaptation mechanisms. *J Neurophysiol*. (Cited on page 95.)

Mitchell, J. F., Sundberg, K. A., and Reynolds, J. H. (2009). Spatial attention decorrelates intrinsic activity fluctuations in macaque area v4. *Neuron*, 63(6):879–88. (Cited on page 8.)

Molyneaux, B. J., Arlotta, P., Menezes, J. R. L., and Macklis, J. D. (2007). Neuronal subtype specification in the cerebral cortex. *Nat Rev Neurosci*, 8(6):427–37. (Cited on page 68.)

Moreno-Bote, R., Renart, A., and Parga, N. (2008). Theory of input spike auto- and cross-correlations and their effect on the response of spiking neurons. *Neural Comput*, 20(7):1651–705. (Cited on pages 57, 94, and 99.)

Neher, E. and Sakmann, B. (1976). Single-channel currents recorded from membrane of denervated frog muscle fibres. *Nature*, 260(5554):799–802. 10.1038/260799a0. (Cited on page 26.)

Niell, C. M. and Stryker, M. P. (2010). Modulation of visual responses by behavioral state in mouse visual cortex. *Neuron*, 65(4):472–9. (Cited on page 62.)

Okun, M. and Lampl, I. (2008). Instantaneous correlation of excitation and inhibition during ongoing and sensory-evoked activities. *Nat Neurosci*, 11(5):535–7. (Cited on pages 6, 60, and 94.)

Okun, M., Naim, A., and Lampl, I. (2010). The subthreshold relation between cortical local field potential and neuronal firing unveiled by intracellular recordings in awake rats. *J Neurosci*, 30(12):4440–8. (Cited on page 96.)

Overduin, S. A., d'Avella, A., Carmena, J. M., and Bizzi, E. (2012). Microstimulation activates a handful of muscle synergies. *Neuron*, 76(6):1071–7. (Cited on pages 5 and 102.)

Paninski, L., Vidne, M., Depasquale, B., and Ferreira, D. G. (2012). Inferring synaptic inputs given a noisy voltage trace via sequential monte carlo methods. *J Comput Neurosci*, 33(1):1–19. (Cited on pages 34, 40, 58, and 96.)

Patil, A., Huard, D., and Fonnesbeck, C. (2010). Pymc: Bayesian stochastic modelling in python. *Journal of statistical software*, 35(4):1. (Cited on pages 16 and 45.)

Pavlides, C., Miyashita, E., and Asanuma, H. (1993). Projection from the sensory to the motor cortex is important in learning motor skills in the monkey. *Journal of Neurophysiology*, 70(2):733–741. (Cited on page 104.)

Paxinos, G. and Franklin, K. (2004). *The Mouse Brain in Stereotaxic Coordinates*. (Cited on page 67.)

Perin, R., Berger, T. K., and Markram, H. (2011). A synaptic organizing principle for cortical neuronal groups. *Proc Natl Acad Sci USA*, 108(13):5419–24. (Cited on page 99.)

Perin, R., Telefont, M., and Markram, H. (2013). Computing the size and number of neuronal clusters in local circuits. *Frontiers in neuroanatomy*, 7:1. (Cited on page 2.)

Peters, A., Chen, S., and Komiyama, T. (2014). Emergence of reproducible spatiotemporal activity during motor learning. *Nature*, 510(7504):263–267. (Cited on page 87.)

Petersen, C. C. H., Hahn, T. T. G., Mehta, M., Grinvald, A., and Sakmann, B. (2003). Interaction of sensory responses with spontaneous depolarization in layer 2/3 barrel cortex. *Proc Natl Acad Sci USA*, 100(23):13638–43. (Cited on page 60.)

Pettersen, K. H., Lindén, H., Tetzlaff, T., and Einevoll, G. T. (2014). Power laws from linear neuronal cable theory: power spectral densities of the soma potential, soma membrane current and single-neuron contribution to the eeg. *PLoS computational biology*, 10(11):e1003928. (Cited on page 25.)

Phillips, C. and Porter, R. (1977). Corticospinal neurones. their role in movement. *Monographs of the Physiological Society*, (34):v. (Cited on page 59.)

Platkiewicz, J. and Brette, R. (2010). A threshold equation for action potential initiation. *PLoS Comput Biol*, 6(7):e1000850. (Cited on page 95.)

Platkiewicz, J. and Brette, R. (2011). Impact of fast sodium channel inactivation on spike threshold dynamics and synaptic integration. *PLoS Comput Biol*, 7(5):e1001129. (Cited on page 95.)

Poirazi, P., Brannon, T., and Mel, B. W. (2003). Arithmetic of subthreshold synaptic summation in a model ca1 pyramidal cell. *Neuron*, 37(6):977–87. (Cited on page 24.)

Polack, P.-O., Friedman, J., and Golshani, P. (2013). Cellular mechanisms of brain state-dependent gain modulation in visual cortex. *Nature Neuroscience*, 16(9):1331–9. (Cited on pages 1, 8, 9, 10, 62, 73, 97, and 100.)

Polsky, A., Mel, B. W., and Schiller, J. (2004). Computational subunits in thin dendrites of pyramidal cells. *Nature Neuroscience*, 7(6):621–7. (Cited on page 24.)

Poo, C. and Isaacson, J. S. (2009). Odor representations in olfactory cortex: "sparse" coding, global inhibition, and oscillations. *Neuron*, 62(6):850–61. (Cited on page 28.)

Poulet, J. F. A., Fernandez, L. M. J., Crochet, S., and Petersen, C. C. H. (2012). Thalamic control of cortical states. *Nat Neurosci*, 15(3):370–2. (Cited on pages 1, 9, 97, and 100.)

Poulet, J. F. A. and Petersen, C. C. H. (2008). Internal brain state regulates membrane potential synchrony in barrel cortex of behaving mice. *Nature*, 454(7206):881–5. (Cited on pages 1, 6, 8, 10, 60, 64, 73, 96, and 100.)

Puil, E., Gimbarzevsky, B., and Miura, R. M. (1986). Quantification of membrane properties of trigeminal root ganglion neurons in guinea pigs. *J Neurophysiol*, 55(5):995–1016. (Cited on page 94.)

Rall, W. (1959). Branching dendritic trees and motoneuron membrane resistivity. *Experimental Neurology*, 1(5):491–527. (Cited on page 25.)

Ramaswamy, K. S., Palmer, M. L., van der Meulen, J. H., Renoux, A., Kostrominova, T. Y., Michele, D. E., and Faulkner, J. A. (2011). Lateral transmission of force is impaired in skeletal muscles of dystrophic mice and very old rats. *The Journal of Physiology*, 589(Pt 5):1195–208. (Cited on page 86.)

Reiner, A., Jiao, Y., Mar, N. D., Laverghetta, A. V., and Lei, W. L. (2003). Differential morphology of pyramidal tract-type and intratelencephalically projecting-type corticostriatal neurons and their intrastriatal terminals in rats. *J. Comp. Neurol.*, 457(4):420–440. (Cited on page 67.)

Renart, A., Rocha, J. D. L., Bartho, P., Hollender, L., Parga, N., Reyes, A., and Harris, K. D. (2010). The asynchronous state in cortical circuits. *Science*, 327(5965):587–90. (Cited on pages 57, 94, and 99.)

Reyes, A. and Sakmann, B. (1999). Developmental switch in the short-term modification of unitary epsps evoked in layer 2/3 and layer 5 pyramidal neurons of rat neocortex. *J Neurosci*, 19(10):3827–35. (Cited on page 88.)

Rice, S. (1954). Mathematical analysis of random noise. *Selected papers on noise and stochastic processes*, 23-24. (Cited on page 36.)

Rocha, J. D. L., Doiron, B., Shea-Brown, E., Josić, K., and Reyes, A. (2007). Correlation between neural spike trains increases with firing rate. *Nature*, 448(7155):802–6. (Cited on page 99.)

Rossant, C., Leijon, S., Magnusson, A. K., and Brette, R. (2011). Sensitivity of noisy neurons to coincident inputs. *Journal of Neuroscience*, 31(47):17193–206. (Cited on pages 11, 66, and 79.)

Rothman, J. S., Cathala, L., Steuber, V., and Silver, R. A. (2009). Synaptic depression enables neuronal gain control. *Nature*, 457(7232):1015–8. (Cited on page 10.)

Roxin, A., Brunel, N., Hansel, D., Mongillo, G., and Vreeswijk, C. V. (2011). On the distribution of firing rates in networks of cortical neurons. *J Neurosci*, 31(45):16217–26. (Cited on page 56.)

Rudolph-Lilith, M. and Destexhe, A. (2003). Characterization of subthreshold voltage fluctuations in neuronal membranes. *Neural Comput*, 15(11):2577–618. (Cited on page 77.)

Rudolph-Lilith, M., Pospischil, M., Timofeev, I., and Destexhe, A. (2007). Inhibition determines membrane potential dynamics and controls action potential generation in awake and sleeping cat cortex. *Journal of Neuroscience*, 27(20):5280–90. (Cited on page 93.)

Sabbione, J. and Velis, D. (2010). Automatic first-breaks picking: New strategies and algorithms. *Geophysics*, 75(4):V67–V76. (Cited on page 105.)

Saleem, A. B., Ayaz, A., Jeffery, K. J., Harris, K. D., and Carandini, M. (2013). Integration of visual motion and locomotion in mouse visual cortex. *Nature Neuroscience*, 16(12):1864–9. (Cited on page 1.)

Sasaki, K., Gemba, H., and Hashimoto, S. (1981). Premovement slow cortical potentials on self-paced hand movements and thalamocortical and corticocortical responses in the monkey. *Exp Neurol*, 72(1):41–50. (Cited on page 5.)

Sayer, R. J., Friedlander, M. J., and Redman, S. J. (1990). The time course and amplitude of epsps evoked at synapses between pairs of ca3/ca1 neurons in the hippocampal slice. *J Neurosci*, 10(3):826–36. (Cited on page 56.)

Schroeder, C. E. and Lakatos, P. (2009). Low-frequency neuronal oscillations as instruments of sensory selection. *Trends Neurosci*, 32(1):9–18. (Cited on pages 9, 96, 106, and 108.)

Schutter, E. (2009). *Computational modeling methods for neuroscientists*. (Cited on page 18.)

Sheets, P. L., Suter, B. A., Kiritani, T., Chan, C. S., Surmeier, D. J., and Shepherd, G. M. G. (2011). Corticospinal-specific hcn expression in mouse motor cortex: I(h)-dependent synaptic integration as a candidate microcircuit mechanism involved in motor control. *J Neurophysiol*, 106(5):2216–31. (Cited on pages 73, 83, 85, and 94.)

Shepherd, G. M. G. (2013). Corticostriatal connectivity and its role in disease. *Nat Rev Neurosci*, 14(4):278–91. (Cited on pages 60 and 99.)

Shin, M., Brager, D., Jaramillo, T. C., Johnston, D., and Chetkovich, D. M. (2008). Mislocalization of h channel subunits underlies h channelopathy in temporal lobe epilepsy. *Neurobiology of Disease*, 32(1):26–36. (Cited on page 94.)

Shu, Y., Hasenstaub, A., and McCormick, D. A. (2003). Turning on and off recurrent balanced cortical activity. *Nature*, 423(6937):288–93. (Cited on pages 60 and 61.)

Shusterman, R., Smear, M., Koulakov, A., and Rinberg, D. (2011). Precise olfactory responses tile the sniff cycle. *Nature Neuroscience*, 14(8):1039–1044. (Cited on page 106.)

Silberberg, G. and Markram, H. (2007). Disynaptic inhibition between neocortical pyramidal cells mediated by martinotti cells. *Neuron*, 53(5):735–46. (Cited on page 85.)

Silver, R. A. (2010). Neuronal arithmetic. *Nat Rev Neurosci*, 11(7):474–89. (Cited on pages 1, 11, 61, and 62.)

Singer, W. (2008). The brain, an orchestra without conductor. *CERN (European Centre for Nuclear Physics) colloquium, 31st January*. (Cited on pages 1 and 109.)

Smith, J., Abdala, A., Borgmann, A., Rybak, I., and Paton, J. (2013). Brainstem respiratory networks: building blocks and microcircuits. *Trends in Neurosciences*, 36(3):152–162. (Cited on page 108.)

Smith, M. A. and Kohn, A. (2008). Spatial and temporal scales of neuronal correlation in primary visual cortex. *Journal of Neuroscience*, 28(48):12591–603. (Cited on pages 57 and 94.)

Song, S., Sjöström, P. J., Reigl, M., Nelson, S., and Chklovskii, D. B. (2005a). Highly nonrandom features of synaptic connectivity in local cortical circuits. *Plos Biol*, 3(3):e68. (Cited on pages 35, 54, and 56.)

Song, S., Sjöström, P. J., Reigl, M., Nelson, S., and Chklovskii, D. B. (2005b). Highly nonrandom features of synaptic connectivity in local cortical circuits. *Plos Biol*, 3(3):e68. (Cited on pages 85 and 99.)

Spiegelhalter, D., Best, N., Carlin, B., and Linde, A. V. D. (2002). Bayesian measures of model complexity and fit. *Journal of the Royal Statistical Society: Series B (Statistical Methodology)*, 64(4):583–639. (Cited on page 15.)

Staude, G., Flachenecker, C., Daumer, M., and Wolf, W. (2001). Onset detection in surface electromyographic signals: a systematic comparison of methods. *EURASIP Journal on Applied Signal Processing*, 2001(1):67–81. (Cited on page 105.)

Steriade, M., Dossi, R. C., and Nuñez, A. (1991). Network modulation of a slow intrinsic oscillation of cat thalamocortical neurons implicated in sleep delta waves: cortically induced synchronization and brainstem cholinergic suppression. *J Neurosci*, 11(10):3200–17. (Cited on page 9.)

Steriade, M. and McCarley, R. W. (2005). Brainstem control of wakefulness and sleep. *Plenum Press, New York*. (Cited on page 7.)

Steriade, M., McCormick, D. A., and Sejnowski, T. J. (1993a). Thalamocortical oscillations in the sleeping and aroused brain. *science*, 262(5134):679–85. (Cited on pages 9 and 96.)

Steriade, M., McCormick, D. A., and Sejnowski, T. J. (1993b). Thalamocortical oscillations in the sleeping and aroused brain. *science*, 262(5134):679–85. (Cited on pages 60, 73, and 96.)

Steriade, M., Timofeev, I., and Grenier, F. (2001). Natural waking and sleep states: a view from inside neocortical neurons. *J Neurophysiol*, 85(5):1969–85. (Cited on pages 60 and 96.)

Suter, B. A., Migliore, M., and Shepherd, G. M. G. (2013). Intrinsic electrophysiology of mouse corticospinal neurons: a class-specific triad of spike-related properties. *Cerebral Cortex*, 23(8):1965–77. (Cited on pages 67 and 73.)

Szapiro, G. and Barbour, B. (2007). Multiple climbing fibers signal to molecular layer interneurons exclusively via glutamate spillover. *Nat Neurosci*, 10(6):735–42. (Cited on pages 31 and 53.)

Tan, A. Y. Y., Chen, Y., Scholl, B., Seidemann, E., and Priebe, N. J. (2014). Sensory stimulation shifts visual cortex from synchronous to asynchronous states. *Nature*, 509(7499):226–9. (Cited on page 1.)

Tanji, J. and Evarts, E. V. (1976). Anticipatory activity of motor cortex neurons in relation to direction of an intended movement. *J Neurophysiol*, 39(5):1062–8. (Cited on page 5.)

Tennant, K. A., Adkins, D. L., Donlan, N. A., Asay, A. L., Thomas, N., Kleim, J. A., and Jones, T. A. (2011). The organization of the forelimb representation of the c57bl/6 mouse motor cortex as defined by intracortical microstimulation and cytoarchitecture. *Cerebral Cortex*, 21(4):865–76. Ggghbhy. (Cited on pages 63 and 64.)

Teramae, J.-N. and Fukai, T. (2014). Computational implications of lognormally distributed synaptic weights. *Proceedings of the IEEE*, 102(4):500. (Cited on page 56.)

Teramae, J.-N., Tsubo, Y., and Fukai, T. (2012). Optimal spike-based communication in excitable networks with strong-sparse and weak-dense links. *Sci. Rep.*, 2:485. (Cited on page 56.)

Tetzlaff, T., Helias, M., Einevoll, G. T., and Diesmann, M. (2012). Decorrelation of neural-network activity by inhibitory feedback. *PLoS computational biology*, 8(8):e1002596. (Cited on pages 94 and 99.)

Tiesinga, P., Fellous, J.-M., Salinas, E., José, J., and Sejnowski, T. (2004). Inhibitory synchrony as a mechanism for attentional gain modulation. *J Physiol Paris*, 98(4–6):296–314. (Cited on pages 61 and 79.)

Torrence, C. and Compo, G. (1998). A practical guide to wavelet analysis. *Bulletin of the American Meteorological Society*, 79(1):61–78. (Cited on pages 70 and 107.)

Ueno, M. and Yamashita, T. (2011). Kinematic analyses reveal impaired locomotion following injury of the motor cortex in mice. *Experimental Neurology*, 230(2):280–90. (Cited on pages 60, 102, and 105.)

Wang, L., Conner, J. M., Rickert, J., and Tuszynski, M. H. (2011). Structural plasticity within highly specific neuronal populations identifies a unique parcellation of motor learning in the adult brain. *Proc Natl Acad Sci USA*. (Cited on page 63.)

Wehr, M. and Zador, A. M. (2003). Balanced inhibition underlies tuning and sharpens spike timing in auditory cortex. *Nature*, 426(6965):442–6. (Cited on pages 28, 34, and 93.)

Weiler, N., Wood, L., Yu, J., Solla, S. A., and Shepherd, G. M. G. (2008). Top-down laminar organization of the excitatory network in motor cortex. *Nat Neurosci*, 11(3):360–6. (Cited on pages 4 and 97.)

Williams, S. R. and Mitchell, S. J. (2008). Direct measurement of somatic voltage clamp errors in central neurons. *Nat Neurosci*, 11(7):790–8. (Cited on pages 28, 52, 83, and 92.)

Wilson, C. J. and Kawaguchi, Y. (1996). The origins of two-state spontaneous membrane potential fluctuations of neostriatal spiny neurons. *J Neurosci*, 16(7):2397–410. (Cited on page 1.)

Yassin, L., Benedetti, B. L., Jouhanneau, J.-S., Wen, J. A., Poulet, J. F. A., and Barth, A. L. (2010). An embedded subnetwork of highly active neurons in the neocortex. *Neuron*, 68(6):1043–50. (Cited on page 99.)

Yasvoina, M. V., Genç, B., Jara, J. H., Sheets, P. L., Quinlan, K. A., Milosevic, A., Shepherd, G. M. G., Heckman, C. J., and Özdinler, P. H. (2013). egfp expression under uchl1 promoter genetically labels corticospinal motor neurons and a subpopulation of degeneration-resistant spinal motor neurons in an als mouse model. *J Neurosci*, 33(18):7890–904. (Cited on page 68.)

Zagha, E., Casale, A. E., Sachdev, R. N. S., McGinley, M. J., and McCormick, D. A. (2013). Motor cortex feedback influences sensory processing by modulating network state. *Neuron*, 79(3):567–78. (Cited on page 9.)